Spark Sintering of Fe-B System Alloys and Their Application for Cutting Tools

Fe-B 系合金の放電焼結と切削工具への適用

Dissertation for the Degree of

Doctor of Philosophy

Department of Mechanical System Engineering
Graduate School of Engineering
Hiroshima University, Japan

Prof. Matsugi Kazuhiro, Advisor

Shaoming Kang

July 2018

Abstract

The cemented carbides consisting of WC grains bound with Co phase have been used for cutting tools, rock drill tip and other wear resistant part during the last several decades. However, W and Co are specified as rare metals due to the uneven distribution of W and Co in the world, limiting their further application in the industry. Therefore, FeB with the same hardness and thermal conductivity to the WC is expected to be the substitute material. Consideration for the low sinterability of FeB, Ni or Fe belongs to the same transition group of Co is introduced to prepare the fully dense compact. In this thesis, the sintering behaviors and mechanical properties of FeB-Fe and FeB-Ni system alloys are investigated to evaluate the potential application in cutting field.

This thesis consists of the following chapters.

Chapter 1 generally describes the motivation and detailed background of this work, which contains the evaluation of cutting performance, the research status of the tool materials, the development of the WC-Co alloys and the recent advances of the FeB alloys.

Chapter 2 defines a 3-dimensional local number, LN3D, and 2-dimensional local number, LN2D, o Fe is first selected as the binder phase and mixes with FeB powders by the elemental blending methods. The effect of Fe content and sintering temperature on the sintering behavior and mechanical properties of FeB-Fe system alloys were investigated to evaluate whether Fe was suitable as a binder phase for FeB.

Chapter 3 gives details the Ni binder phase is also investigated by the electroless Ni plating and spark sintering methods. The electroless Ni plating parameters such as the treating amount of the FeB powder, bath temperature and plating time are optimized so that the Ni is coated evenly on the surface of FeB particles. After that, the sintering behaviors and mechanical properties of fully dense FeB with the different Ni content compacts are investigated. The effect of the sintering parameters such as sintering

temperature and holding time on the FeB-Ni compacts are also investigated to prepare the FeB-Ni compacts with high relative density and homogeneous distribution of Ni.

Chapter 4 presents rthe practical application measurement including the wear and friction tests and the interrupted cutting tests are carried out using the fully dense FeB-Ni compact. The cutting tests of FeB-Ni compacts are studied under the cutting speed of 1.7-10 m/min compared with WC-7.8Co cutting tools as well as the wear and friction tests. The effect of the speed on the wear and cutting mechanism and properties are investigated.

Chapter 5 summarizes all the previous chapters and proposes the conclusions of the research work.

CONTENTS

Chapter 1
Background and Objective

1.1 Introduction

Metal cutting process is one of the most widely used technologies in the modern manufacturing field[1-3]. Up to 15% of all the mechanical components manufactured worldwide are derived from the metal cutting technology[2]. For the metal cutting, the cutting tool plays a decisive role in the development of the cutting technology. The tool materials, tool structure and the geometry of the tool determine the cutting performance, especially the tool materials. The machining accuracy, the quality of machined surface, cutting efficiency, tool life, consumption of the tool and processing costs depend on the performance of the tool materials. In the metal cutting process, the cutting edge of the tool must withstand extreme process conditions such as high contact cutting pressure, high cutting temperature and severe friction and wear against the workpiece surface by fast moving chip. Furthermore, the tool is subjected to great impact and vibration in the interrupted cutting.

1.1.1 Study on the cutting performance

In machining, tool life is the most important practical consideration when choosing cutting tools and cutting conditions. Cutting tools with long service lives can reduce production costs and more consistent dimensional and surface finish capability due to the slowly wear or otherwise fail. For these reasons, tool life is the most commonly used standard for evaluating cutting tool performance and the machinability of materials.

1.1.1.1 Type of tool wear

An understanding of the tool life requires an understanding of the ways of tool failure. Tool wear and failure mechanisms have great practical significances, because they will affect the processing cost and quality. Generally, tool failure may cause by tool wear,

plastic deformation or fracture. Tool wear may be classified by the region of the tool affected or by the physical mechanisms that produce it. The principle types of tool wear, classified according to the regions of the tool they affect, are shown in Fig.1.1[4].

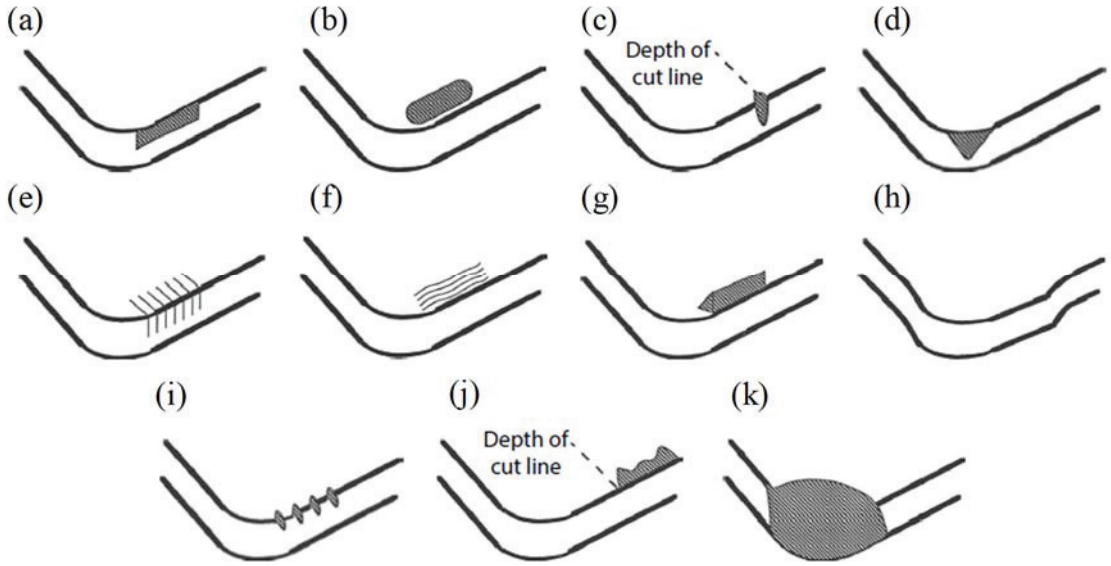

Figure 1.1 Types of wear on cutting tools: (a) flank wear; (b) crater wear; (c) notch wear; (d) nose radius wear; (e) comb (thermal) cracks; (f) parallel (mechanical) cracks; (g) built-up edge; (h) gross plastic deformation; (i) edge chipping or frittering; (j) chip hammering; (k) gross fracture[4].

Flank wear is the wear observed on the flank or clearance face and results in the formation of a wear land as shown in Fig.1.1a and 1.2a. The extent of flank wear is characterized by an average or maximum wear width VB. The flank wear between the wear land and machined surface damages the surface and produces frictional heating and flank force, thereby increasing deflections and reducing dimensional accuracy. Generally, tool life is assumed to be over when the average width of the flank wear land VB reaches 0.3 mm[5]. Flank wear most commonly results from abrasion by the hard constituents of the workpiece material. This is a common failure mode in the machining of steel and cast iron, in which the abrasive particles are predominantly Fe_3C cementite and non-metallic inclusions. By increasing the wear resistance of tool materials and using hard coatings on cutting tools, the flank wear can be reduced.

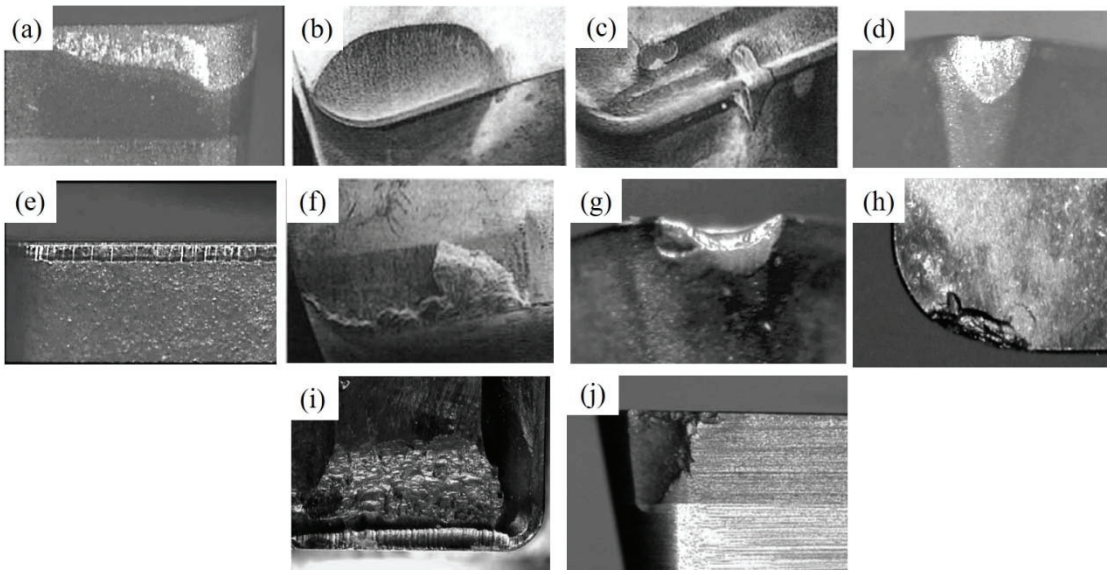

Figure 1.2 (a) Severe flank and nose radius wear on a carbide insert used to machine 390 Al. (b) Rake face wear on a cemented carbide tool produced during the machining of plain carbon steel. (c) Notch wear on a carbide tool produced during the machining of a nickel-base super alloy. (d) Nose radius wear on a coated carbide insert used to machine a nickel alloy.(e) Thermal cracks in coated carbide inserts used to mill compacted graphite iron under dry machining.(f) Built-up edge produced during low speed machining of a nickel-base alloy.(g) Plastic deformation of a carbide tool edge used to machine a nickel alloy.(h) Edge chipping on a polycrystalline cubic boron nitride insert used to machine hard steel.(i) Built-up edge produced during low speed machining of a nickel-base alloy. (j) Fractured edge on a polycrystalline cubic boron nitride insert used to machine hard steel[4,5].

Rake face or crater wear produces a wear crater on the rake face of the cutting tools as shown in Fig.1.1b and 1.2b. The extent of rake wear characterized by an average or maximum wear width KT. It is mainly due to the chemical interaction between the rake face of the cutting tool and the hot chips. Moderate rake face wear usually does not restrict the tool life. In fact, the formation of the crater increases the effective rake angle of the tool which can reduce the cutting forces. However, excessive rake face wear weakens the cutting edge, leads to deformation or fracture of the tool and should be avoided because it shortens the tool life and makes resharpening the tool difficult. By increasing the chemical stability of the tool material or by reducing the chemical solubility of the tool

in the chip, the rake face wear can be reduced; this can be achieved by applying coatings. In addition, decreasing the cutting speed is also an effective way to control the rake face wear.

Notch wear (depth-of-cut notching) often appears on the tools used in rough turning, especially at the contact point between the tool and the unmachined surface or the free edge of the tool, as shown in Fig.1.1c and 1.2c. Notch wear is usually caused by abration[6]. It is particularly common when cutting parts with a hard surface layer or scale, or the work hardening material which produces abrasive chips (such as stainless steel and nickel-base alloy). Notch wear is also attribute to the oxidation if a coolant is used, or the chemical reaction or corrosion at the interface between the tool and the atmosphere. Notch wear can lead to tool fracture and can be minimized by applying tools with high hot hardness and plastic deformation resistance, by increasing the lead angle which increases the area of contact between the tool and part surface or using chamfered edges, rounded inserts and avoiding small depths of cut.

Nose radius wear or tool-tip blunting, shown in Fig.1.1d and 1.2d, appears on the nose radius of the tool, on the trailing edge near the end of the flank face. It is similar to the combination of flank and notch wear, and mainly caused by the abrasion and corrosion or oxidation.

Thermal and mechanical cracking, shown in Fig.1.1e, f and 1.2e, usually results from cyclic thermal and mechanical loading of the tool associated with interrupted cutting. Two types of cracks may occur: cracks perpendicular to the cutting edge, which usually causes by cyclic thermal loads, especially when a coolant is used; cracks parallel to the cutting edge, which usually causes by cyclic mechanical loads. Thermal and mechanical cracking may lead to rapid tool fracture or fragment.

Built-up edge (BUE), shown in Fig.1.1g and 1.2f, is referred to when metal adheres strongly to the cutting edge, building up and projecting forward from it. It typically occurs when cutting soft and ductile metals such as Al, Ni, Co and Ti alloys at low cutting speeds and light feed rates. BUE formation is undesirable because it changes the effective depth of cut. In addition, BUE is often unstable, resulting in poor surface finish and tool chipping. BUE formation can be reduced by using more positive rake angle, with smooth

surface finish (<0.5 μm Ra) and higher cutting speeds.

Plastic deformation of the cutting edge, shown in Fig.1.1h and 1.1g, occurs when the cutting tool cannot support the cutting pressure between the tool and the chip. Cutting edge deformation usually occurs at high feed rates, which results in higher cutting-edge loads, or at higher cutting speeds because the hardness of the tool decreases with increment of the cutting temperature.

Edge chipping or frittering, shown in Fig.1.1i and 1.1h, occurs when cutting with brittle tool materials, or when cutting work materials including hard or abrasive particles. Edge chipping leads to poor surface finish and increased flank wear, and may cause tool failure.

Chip hammering, shown in Fig.1.1j and 1.1i, occurs when cutting materials form a tough or abrasive chip. It occurs when the chip curls back and strikes the tool face away from the cutting edge. Chip hammering is caused by improper chip control and can be eliminated by changing the lead angle, cutting depth, feed rate or tool nose radius.

Tool fracture or breakage, shown in Fig.1.1k and 1.1j, leads to the catastrophic loss of the cutting edge and a large part of the tool. Tool breakage occurs when cutting tools fail to support the cutting force on the tool-chip contact area. The general strategy to eliminate the fracture including reducing the cutting force, using of stronger or more rigid tooling sets and using tools with improved fracture toughness.

1.1.1.2 Tool wear mechanism

The physical mechanisms that produce the various types of wear described above depend on various cutting conditions, especially the cutting speed. At lower cutting speed, the most significant types of wear are related to the abrasion and adhesive. Adhesive wear occurs when small particles of the tool adhere or weld to the chip and are removed from the tool surface due to friction. It occurs mainly on the rake face of the tool, leading to the formation of crater wear. This type of wear is not normally practically significant due to the low adhesive wear rate. However, significant adhesive wear may promote the formation of BUE which can result in the edge chipping. Abrasive wear occurs when hard particles slide against and remove material from the cutting tool. The hard particles come from either the work material's microstructure or broken away from the cutting edge by

brittle fracture. Abrasive wear occurs mainly on the flank face of the tool. As a result, abrasive wear is usually the main cause of flank wear, notch wear and nose radius wear. Thus, it is usually the form of wear that controls the life of the cutting tool, especially at low to medium cutting speeds.

As the cutting speed is increased, adhesive and abrasive wear rates increase due to the increased distance slid in a given time and the increased cutting temperatures. Generally, the hardness of the tool materials reduces with the increment of the temperature, which known as thermal softening. The thermal softening effect may cause the plastic deformation of the cutting edge.

As the cutting speed is increased further, temperature-activated wear mechanisms including diffusion, oxidation, and chemical wear become predominant. In diffusion wear, constituents of the tool material diffuse into or form solid solutions with the chip material. This weakens the tool surface and causes the crater wear or even breakage. Oxidation occurs when constituents of the tool material (especially the binder) react with atmospheric oxygen. Oxidation may cause severe depth-of-cut notch wear, or formation of hard oxide particles which increasing the abrasive wear. Chemical wear caused by chemical reactions between constituents of the tool and the workpiece or cutting fluid, results in flank and crater wear. Reducing the cutting speed can effectively reduce many types of wear, but since this can reduce the metal removal rate.

1.1.1.3 Tool life

Tool life affects the choice of tool, selection of the process variables, economy of operations and possibility of the process's adaptive control. It is well known that tool life depends on several factors that characterize the performance of machine, tools and work system. Thus, it is impossible to derive a universal tool-life criterion for these all quantitative and qualitative variables. In other word, tool life is not an absolute concept but depends on the choice of the tool life criterion. Among standardized tool life tests, the flank wear criterion (VB=0.3mm) is used because flank wear is normally the most desirable type of wear. The flank wear rate is relatively low and repeatable, so the tool life is relatively long and consistent. Tool wear curves illustrate the relationship between the flank wear width and the cutting time (t) or the overall length of the cutting path (L),

as shown in Fig.1.3[4]. There are three characteristic parts that can be observed on these curves. The first region (I in Fig.1.3(b)) is the region of initial wear. Relatively high rate of wear (an increase of tool wear per unit time or length) occurs in this region. It is caused by accelerated wear of the tool layers damaged during its manufacturing or resharpening. The second region (II in Fig.1.3(b)) is the region of steady wear. This is the normal operating region for cutting tools. The third region (III in Fig. 1.3(b)) is known as the accelerated wear region. In this region, flank wear accelerates and becomes severe, which often leads to catastrophic failure. Tools should not be used within this region.

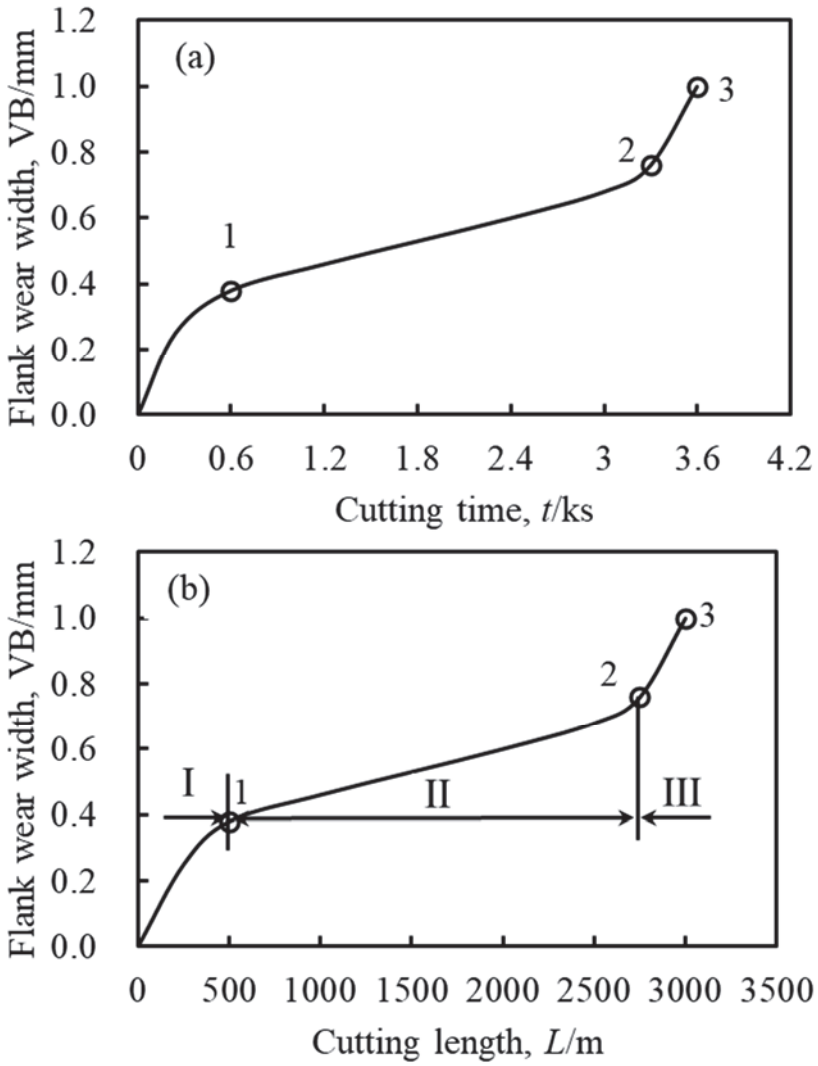

Figure 1.3 Typical tool wear curves for flank wear: (a) as a function of time and (b) as a function of cutting length[4].

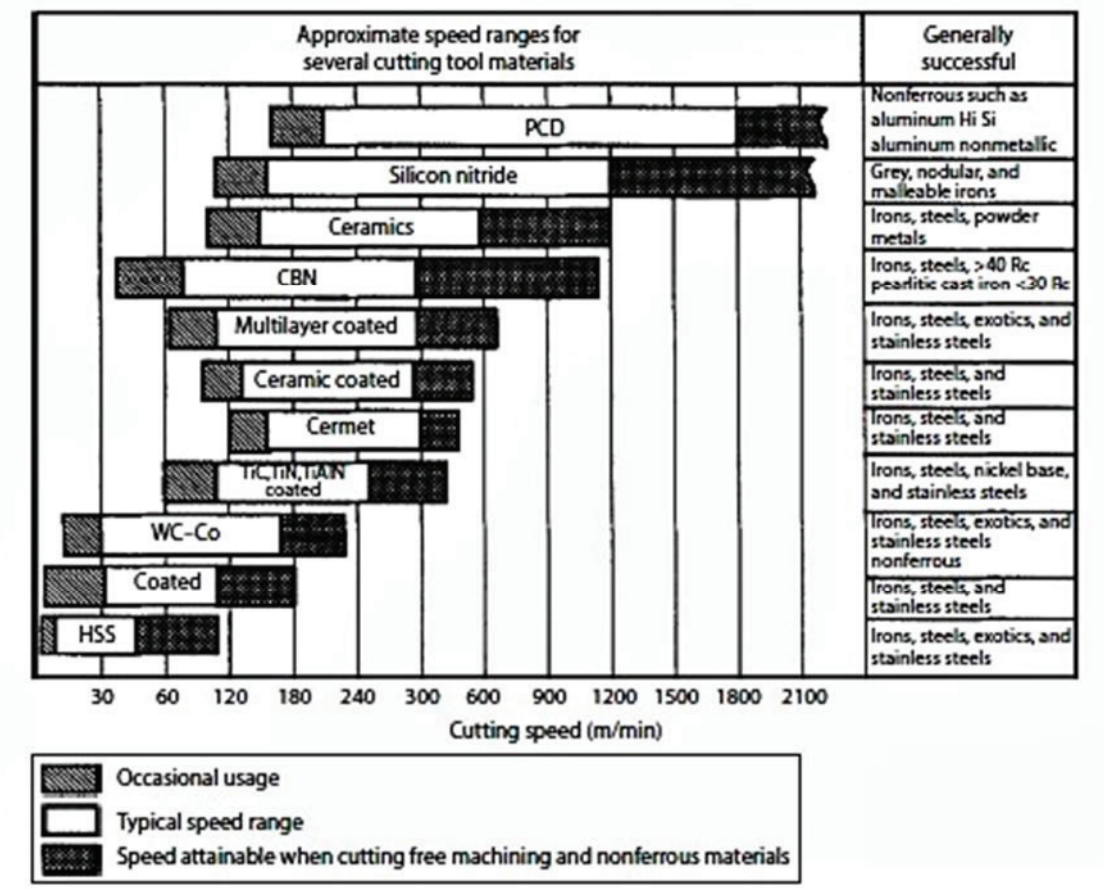

Figure 1.4 Procedure for tool selection and optimization of cutting conditions[7].

1.1.2 Development of the cutting tools

Generally, the tool material should have certain properties, namely[4]:

1. High hardness at elevated temperatures to resist abrasive wear.

2. High deformation resistance to prevent the cutting edge from plastic deformation under high stresses and high temperatures generated during chip formation.

3. High fracture toughness to resist edge micro-chipping and breakage especially in the interrupted cutting.

4. Chemical inertness (low chemical affinity or high chemical stability) with respect to workpiece material to protect against heat-affected wear types, i.e. chemical, oxidation and diffusion oxidation wear.

5. High thermal conductivity to reduce temperatures near the cutting edge (the cool edge of the tool).

6. High fatigue resistance for tools withstanding peaked mechanical loads.

7. High thermal shock resistance which naturally follows the mechanical shock.

8. High stiffness to maintain accuracy.

9. Adequate lubricity (low friction) with respect to the workpiece material to increase welding resistance and to prevent built-up edge, especially when cutting soft, ductile materials.

The first three properties are required to prevent sudden, catastrophic failure of the tool. Properties 1, 4 and 5 are required to resist the high temperatures generated during chip formation. Elevated tool temperatures will aggravate thermal softening, diffusion or chemical wear of the tool, which resulting in rapid tool wear[7-10]. Properties 3, 6 and 7 are required to prevent chipping and breakage of the tool, especially in interrupted cutting. It should be noted that no single too material exhibits all the above mentioned desirable properties for a tool material in practice. The choice of the tool materials depending on the types of machining operations, workpiece materials being machined, the required accuracy, overall thermochemical process conditions and economic considerations, as reference in Fig. 1.4.

The common tool materials currently in use include high speed steel(HSS) and cobalt rich high-speed steel(HSS-Co), cemented carbides(WC), cermet(TiC), ceramics (alumina and silicon carbides), super-/ ultra-hard materials such as polycrystalline cubic boron nitride (PCBN) and polycrystalline diamond (PCD) [4].

When compared with competing tool materials, HSS possesses moderate wear resistance, high transverse rupture strength and low cost. However, the limited wear resistance, chemical stability and greater tendency to form a built-up edge than other materials make HSS tools suitable for use only at limited cutting speeds. Cemented carbides belong to a class of refractory materials in which the hard carbides of Group IVB-VIB metals are bound together or cemented by a ductile metal binder, usually Fe, Ni or Co[11,12]. Owing to the high hardness and wear resistance of the hard phases, cemented carbides have been used for cutting and wear resistance tools. Generally, the WC-based composites are usually referred as “cemented carbides”, while others like TiC-based ones are referred as “cermets”[13]. Cermets are TiC-, TiN-, or TiCN-based

hardmetals which often described as ceramic or carbide composites. Cermets have excellent deformation resistance and high chemical stability, but relatively poor strength and toughness. Ceramic tools are characterized by high hardness, high wear resistance and chemically stability. Whereas, the relatively low strength, low fracture toughness and poor resistance to thermal and mechanical shock usually make them more susceptible to excessive chipping or cracks, leading to a short tool life[14]. PCBN has a high thermal conductivity, high hot hardness, and excellent thermal stability. It is one of the hardest materials known after diamond and widely used in ferrous metal cutting[15]. PCD is a kind of extremely wear resistance material referred to as super-hard materials. However, PCD is not suitable for machining steel materials due to the strong affinity of the diamond and iron. Both materials are manufactured using a high temperature, high pressure process in which individual diamond or CBN particles are consolidated in the presence of Fe, Ni and/or Co catalysts that promote grain consolidation into a solid mass (solid polycrystalline) or on a WC substrate (backed polycrystalline). However, the extremely high fabrication cost of PCBN and PCD limit their application in industries.

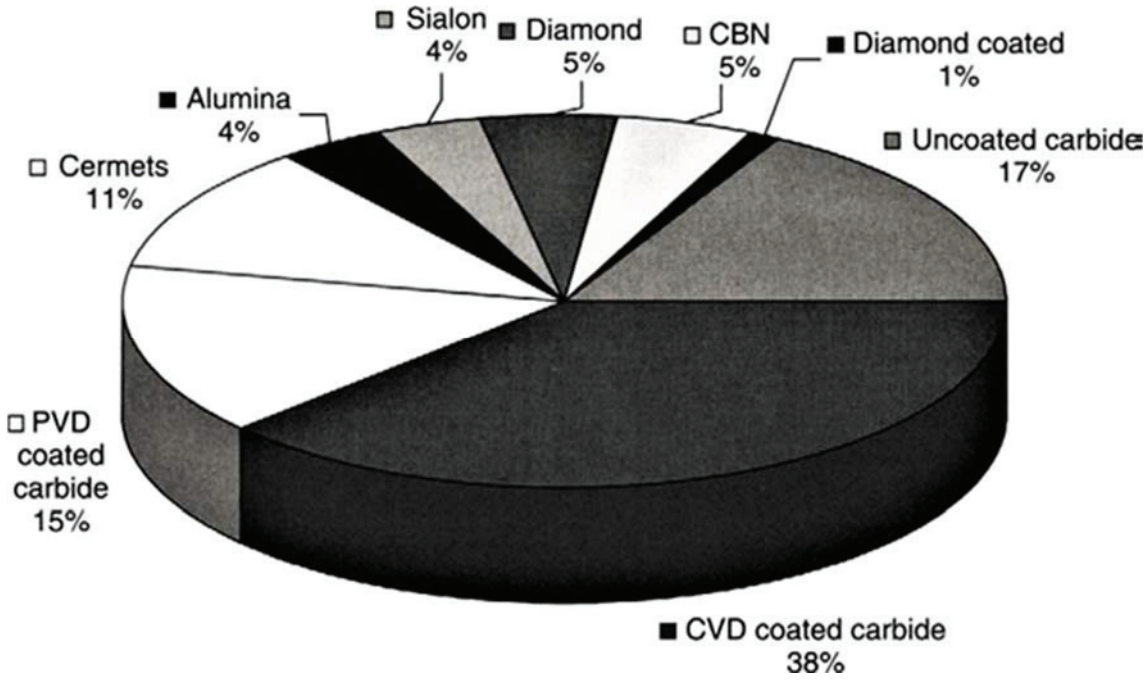

Figure 1.5 Estimated global use of the main cutting tool materials in year 2005[17].

1.2 Research on the cemented carbides hard materials

In recent years, with the development and application of advanced manufacturing technology and all kinds of new and difficult to machine materials, the higher requirement of the performance of the tool materials is put forward. Cemented carbide tool materials become more and more widely used because of their excellent comprehensive properties. As shown in Fig.1.5, it can be seen in this pie diagram that carbide tools are mostly used in the manufacturing sector (about 70% of the total usage including the coated carbides). The composite formed by the combination of WC and Co is the most traditionally used system in cemented carbides[18]. Although it has been developed more than 70 years old, the WC-Co hard metals continue to gain importance for cutting, mining and chipless forming tools, as well as for high performance construction and wear parts. For the modern hard metals, a broad range of WC grades are used together with carbides such as (Ta,Nb)C, TiC, (W,Ti,Ta)C and special grades of Co powder. These continuously improved or newly developed powder intermediates have been essential to the improved performance of modern hardmetal tools and wear parts.

Future developments in the field of hard materials are mainly related to: (i) the WC with low or free Co hard materials, owing to the raw materials supply and its scarcity resulting in high prices; (ii) WC-Co with superfine and nanocrystalline hard materials. The superiority of superfine and nanocrystalline hard materials is mainly because very high hardness can be combined with high strength[18]; (iii) WC–Co ultra-coarse grades. The hardmetal grades are characterized by the combination of higher hardness and transverse rupture strength as result of the binder hardening and reinforcement[19]; (iv) coated WC-Co hard materials. Coated WC-Co cutting tools offer proven performance advantages such as the high mechanical and thermal shock resistance[20].

The occurrence of W and Co ore is rich in the world. However, as shown in Fig. 1.6, the location of the ore, refining efficiency and the concentration that economic to mining have a significant impact on the ready availability[21]. Consequently, W and Co are considered as strategic materials. Major producing countries have strengthened the management of strategic resources for W and Co, which result in the supply and price instability. Another important consideration for the WC-Co comes from the health

perspective. In Europe the REACH program[22], so far has classified Co as very toxic to the human health. In addition, Co as the binder has several detrimental properties related to its hcp lattice structure[23,24]. This, together with the raw material prices has increased the research activities to find alternatives to both WC and Co.

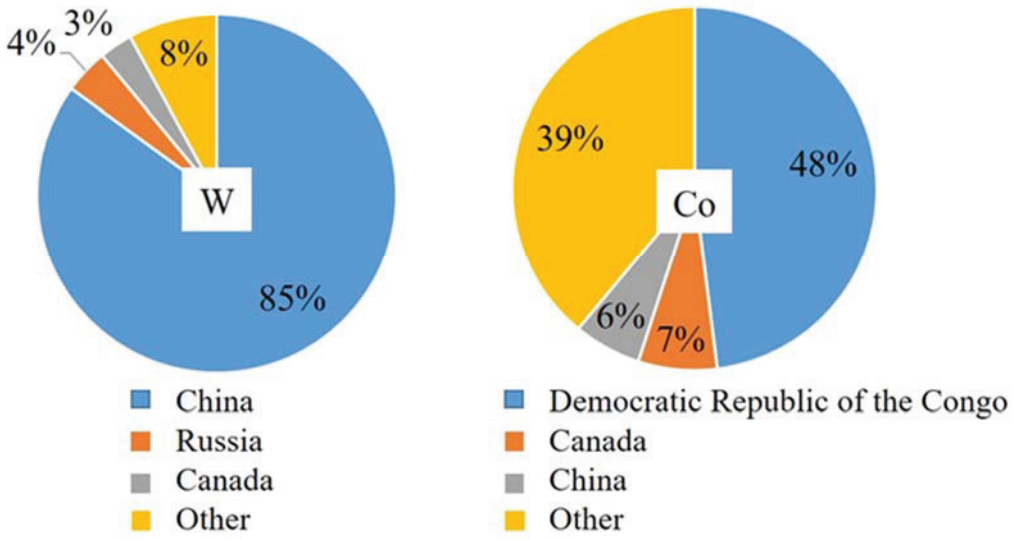

Figure 1.6 Major producing country for W and Co[25,26].

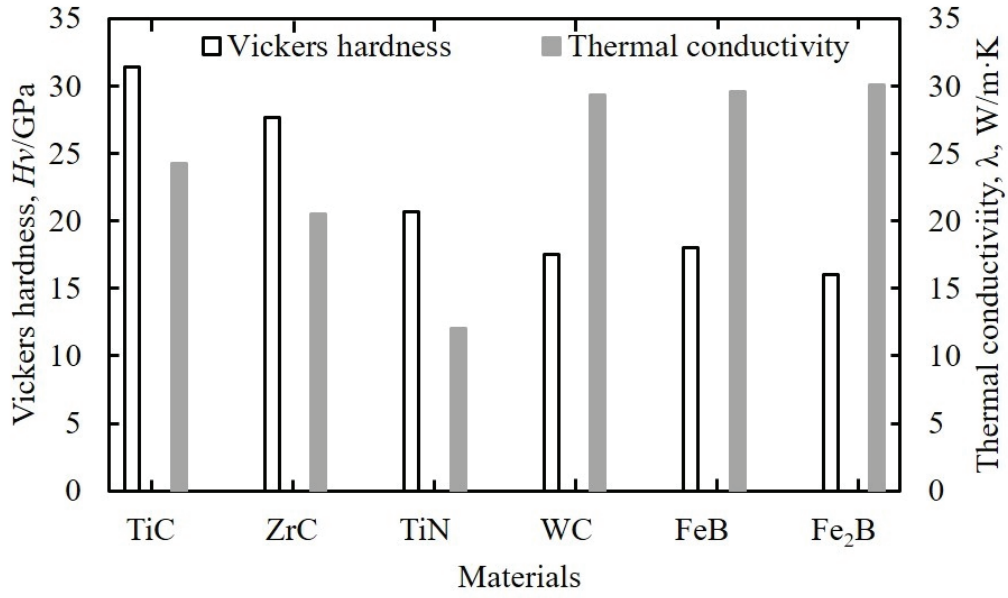

Figure 1.7 Vickers hardness and thermal conductivity of some metallic carbides, nitrides and borides[27].

1.3 Overview of iron borides hard materials

By the reasons mentioned above, one of the main topics of the actual research in the field of cemented carbides concerns the development of new composites having comparable or superior properties with partial or total substitution of the WC and Co by other more economic and less toxic materials. Both hard and binder phases are modified by refractory carbides, nitrides, borides and other iron group transition metals to substitute the WC-Co[12]. Borides have a unique combination of thermal, mechanical, electrical and chemical properties. As shown in Fig.1.7, iron borides (FeB/Fe_2B) show the same level thermal conductivity and hardness with WC. Iron borides can be prepared through the direct combination of the ubiquitous elements Fe and B. It is expected that iron borides (FeB/Fe_2B) can substitute WC in the application of cutting tools.

1.3.1 The structure of the iron borides

The structure of the iron borides is related to the position of B and Fe in the crystal structure. The B atoms have a general tendency to form chains, nets or three-dimensional frameworks which may be alternatively be classified into two groups based on the crystallo-chemical consideration: boride structures of lower boron content or boron-rich compositions. The structures of iron borides (FeB/Fe_2B) are determined by their metallic lattices which belong to the boride structures of lower boron content. The mass concentration of B in FeB and Fe_2B is 8.83% and 16.23%, respectively. The B atoms forming zig-zag chains in FeB and Fe_2B with isolated B atoms as shown in figure 1.8 and 1.9, respectively. FeB crystallizes have an orthorhombic structure and Fe_2B has a body-centered tetragonal (bct) structure. The structural information for the two Fe-B crystals including the lattice constants and the nearest-neighbor (NN) distances is summarized in Table I[28]. For the structure of the FeB, the metal lattices may be regarded as consisting of trigonal prisms connected in different ways. Channels appear through which boron chains are extended through the lattices. The type of Fe_2B belongs to a great number of borides of the $CuAl_2$-type (C16), which consists of sheets of tetrahedra of metal atoms with B atoms in the holes between these sheets. The structure can be regarded as composed of alternate layers of Fe and B atoms.

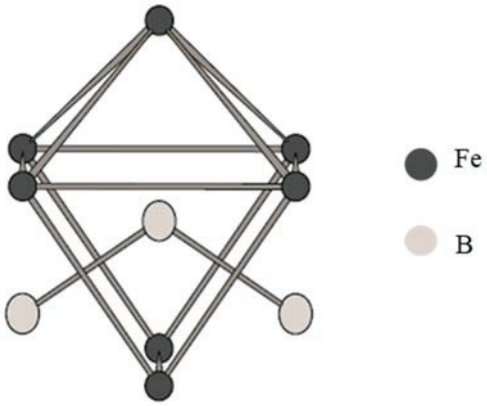

Figure 1.8 Part of the crystal structure of FeB, view approximately along the a axis[28].

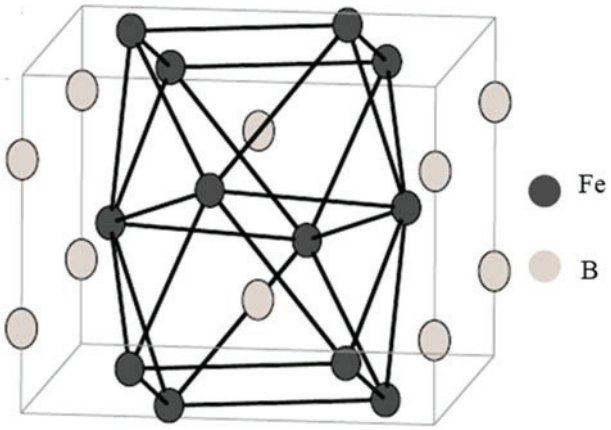

Figure 1.9 The structure of Fe_2B[28].

Table 1.1 Crystal structure information of FeB and Fe_2B. The numbers in parentheses represent the number of bonds[28].

	FeB	Fe_2B
Crystal structure	Orthorhombic	bct
Lattice constant (Å)	a=5.5076	a=5.110
	b=2.9528	
	c=4.0625	c=4.249
Z (moll/cell)	4	3
Space group	*P*nma	*I*4/mcm
NN Dist. (Å)	2.1455(2)	2.1799(8)
	2.1710(2)	

1.3.2 The properties of the iron borides

Iron borides are interstitial compounds, the B atoms occupying interstitial positions in the distorted Fe lattice. Interstitial compounds consisting of relatively large transition-metal atoms and smaller metalloids have many useful properties, such as hardness, high melting point, wear resistance, corrosion resistance, good electric and thermal conductivity, catalytic properties and ferromagnetism. These properties are attributed to the stable electronic configuration. Iron borides are extremely hard and brittle as well as high Young's modulus. Iron borides are characterized by chemical inertness in dilute and even in concentrated acids and bases except for the oxidizing acids[29]. Furthermore, iron borides display reasonably good resistance to oxidation in air. Generally, the borides should have low oxidation resistance because the free energy of formation for most borides is low (80-150 kJ/mole). It is surmised that a protective layer of mixed oxides formed at the surface which is responsible for the slow oxidation rate[30]. An interesting property of iron borides is their high resistance against the molten metals (for instance Fe and Al), non-basic slags and salts. In addition, iron borides show ferromagnetic with well electrical conductivity.

1.3.3 The development of the iron borides

The iron borides have vast practical application as well as providing interest for fundamental study. L.G. Yu et al[31] investigate the FeB/Fe_2B phase transformation during SPS pack-boriding. FeB and Fe_2B phases have been applied in the surface of boride-doped steels through boriding. In the boriding process, the formation of FeB and Fe_2B phases occurs through the diffusion of B atoms into the steel enhance the hardness and wear resistance of the base metal. Iron borides are also used as deoxidizing agents, and alloying components of coatings applied to weld-facing electrodes. Greenwood et al[32] overview the chemical properties of the iron borides including the solubility of iron borides in aqueous acids, halogens, the oxidation resistance and the resistance of the molten salts. In addition, Ying Bai et al[33] investigate the FeB alloy prepared by an electric arc method and used as the anode material for alkaline secondary batteries due to the excellent electrochemical performances. Early expectations that the borides would be

able to successfully compete with the refractory carbides as constituents in hard materials[34]. Steinitz finds that Mo_2B with Ni as binder phase are claimed to be promising cutting tool materials. Simultaneously, Merz finds that the material composed of the CrB with Mo as binder phase is the potential tool material. It is difficult to find a useful combination of a refractory boride and a binder alloy with appropriate wetting properties. Recently, Matsugi et al fabricate ubiquitous hard materials compacts which are 0, 10 and 50 vol.% Fe added in the FeB powders by spark plasma sintering technique. The sintering behaviors using FeB powders with Fe as binder phase is investigated. In addition, the hardness, wear resistance and cutting performance of the FeB with Fe compact are characterized [35,36]. It is found that FeB is satisfied for its standard value of VB (0.3 mm) as the cutting tool. Further investigation on FeB with suitable binder phase to be the cutting tool material is needed.

1.3.4 Selection of the binder phase

The achievement of full density is diffcult for iron borides because of the poor deformability. It requires high temperatures, high pressures and long holding times to achieve acceptable dense compacts which lead to microstructures consisting of large grains and high energy consumption. However, the sintering ability of iron borides will be enhanced dramatically by introducing binder phase such as Fe, Ni or Co, which all have good deformability. In this way the plastic deformaion of iron borides is not needed. Prakash[37] reports that hard materials with Fe-rich binders have improved mechanical properties such as higher hardness, abrasive wear resistance and toughness compared to Co bonded cemented carbides. Fe is considered as the suitable binder phase for the rich reservese and low price compared with other transition metals. The conventional method of adding binder metal (e.g. Co powders to WC powders) is usually carried out by mechanical mixing. Normally, FeB and Fe powders are evenly mixed in the same way as WC and Co.

On the other hand, Ni as a suitable candidate binder phase is also investiaged. Ni unlike Co or Fe, has no phase transition and retains its face centered cubic(fcc) structure at all temperatures below the solidus. Additions of Ni on the one hand can stabilize the face centered cubic structure to give an austentic ductile binder. Ni binder phase is

introduced by the electroless plating method. Electroless plating is an electrochemical process without external electric field. Electroless plating describes the methods of depositing metal ions by means of autocatalytic oxidation reduction reactions. The metal ions in the solution are selectively reduced to substrate with catalytically active surface by using the appropriate reducing agent. Electroless plating is widely used to fabricate metallic coatings on various materials regardles of the shape due to its simple operation and low cost. Electroless plating Ni on the powders could avoid the direct contact and agglomeration of the hard particls, improving the hemogeneous of the chemical composition and enhancing interfcial bonding strength. Futhermore, electroless Ni plating is widely used because of the hemogeneous distribution of the coating and high adehisieve.

1.4 Preparation of hard materials

Powder metallurgy (PM) is suitable for making unique materials impossible to get from melting or forming in other ways. PM is a processing technique used to produce bulk materials and components from metal or ceramic powders. Generally, PM is a process whereby powders are compressed as a green body and sintered to a net shape at elevated temperatures about 0.6–0.8 Tm[38]. Sintering is a technique of consolidating powder compacts by thermal energy[39]. Sintering is one of the most critical processes affecting the microstructure and properties of hard materials. The optimized sintering process is very important for the preparation of excellent hard materials. There are challenging demands from the PM industry for new and improved sintering process with finer microstructures and enhanced physical and mechanical properties. After years of production practice and research, many different types of sintering technology have been developed including vacuum sintering, hot isostatic pressing sintering and spark plasma sintering, et al.

Vacuum sintering is a sintering process under the vacuum condition. Under the vacuum condition, the wettability between the hard phase and the binder phase, the process of densification is promoted, the relative density and mechanical properties of the hard materials are improved. The impurities in the sintered body are easily eliminated and

the residual pores are reduced. Thereby the impurity segregation between hard phase and binder phase as well as the interfacial between hard phase is decrease. The disadvantage of vacuum sintering is that the sintered compact still has a small number of pores and defects. It is difficult to achieve full densification.

Hot isostatic pressing (HIP) is a densification method applying the isostatic pressure to prepare compacts. In the HIP process, both high temperature (about 70% of the melting point) and high pressure (generally 100-200 MPa) are applied simultaneously to obtain fully dense compacts[40]. The defects of the heterogeneous microstructure and properties of the compacts are improved under the uniform external pressure[41]. In addition, HIP can be employed for manufacturing complex parts due to the ability of near net-shape parts (reducing costly machining)[42]. It thus offers unique benefits for metal, ceramic and refractory applications. However, hot isostatic pressing is relatively expensive and it is difficult to sinter parts at temperature so high above 1600°C[43]. Moreover, the application of hot isostatic pressing sintering equipment is limited because of its high requirement for equipment, low production cost and low efficiency.

Low pressure sintering is a sintering technique that makes the compacts achieve full densification under high temperature and isostatic pressure. Compared with HIP process, low pressure sintering is low pressure and low-cost method with simple equipment for fabricating complex shaped compacts. Low pressure sintering is widely used in industrial because it can significantly reduce the porosity and eliminate internal defects[44]. However, to obtain full dense compact via low pressure sintering require high temperature. High temperature sintering causes exaggerated grain growth which results in a deterioration of the resultant mechanical properties, such as the strength.

Microwave heating is a process in which the materials couple with microwaves, absorb the electromagnetic energy volumetrically and transform into heat[45]. Through the interaction between microwave and materials, microwave sintering increases the kinetic energy of the molecules or ions inside of the sintered materials, decreases the sintering activation energy and raises the diffusion coefficient which can be carried out at low temperature sintering and inhibits the grain growth. Microwave sintering can heat the material both inside and outside evenly at the same time, thereby reducing the thermal

stress inside the material. While the traditional sintering process, heating is achieved by diffusion from the outside to the inside of the material resulting in the uneven distribution of the temperature. In addition, this heating mechanism of microwave sintering is advantageous due to very rapid heating rates and decreased sintering temperatures. However, their application is limited to the manufacture of high-power microwave oven equipment.

Spark plasma sintering (SPS) is a newly developed rapid sintering technique with a great potential for achieving high densification compacts with minimal grain growth in a shorter sintering time[46]. SPS is a technology of pressing and sintering the powders pressed into the mold with graphite and other materials by using the upper and lower die punching and pulse current. In the process of sintering, the rapid breakdown of the pulse current destroys the oxide layer of the powder surface and makes the surface of the particles be purified and activates the powders. Moreover, under the pressure, pulse energy and Joule heat caused by the instantaneous high temperature, make powders form the dense compacts by hot plastic deformation. SPS combines plasma activation, resistance heating and hot pressing with the advantages of sintering in the process of pressurization. The plasma produced by the pressure and pulse current in the sintering process will reduce the sintering temperature of the powders. Simultaneously, the sintering process with high current and low voltage will promote the rapid densification of the powders[47].

As a non-equilibrium sintering technology, SPS has been widely used, but its complex sintering mechanism has not yet reached a unified understanding. Chen[48-50] studies the effect of DC pulse and current on sintering as well as the distribution of current and temperature within the sintering system, providing a better understanding of the SPS process. Chen[51] studies the densification process of SPS and proposes the two-particle model of neck formation mechanism to explain the mechanism of rapid sintering. The model predictions are consistent with the experimentally observed neck size distributions. SPS as an advanced sintering technology has been applied to fabricate various materials including metals and alloys, compounds, ceramics and composites.

1.5 Objective and outline of the thesis

The objective of this thesis is to develop the ubiquitous FeB system hard materials with Fe or Ni by spark sintering process. Firstly, the sintering behaviors and mechanical properties of FeB-Fe system hard materials mixed by elemental blending method are investigated. Then the sintering behavior and mechanical properties of FeB with Ni added by electroless plating process hard materials are also investigated. In addition, the electroless Ni plating and spark sintering parameters are optimized to obtain the homogeneous distribution of the Ni binder phase and full dense compacts. Finally, the practical application experiments of the FeB-Ni system hard materials including the interrupted cutting tests under different cutting speed are investigated.

Chapter 1 reviews the scientific background of this research, points out the objective and illustrates the overall content of the thesis.

Chapter 2 introduces the sintering behaviors and mechanical properties of FeB with 0, 10 an 50vol.% Fe as the binder phase mixed by elemental blending method. The effect of Fe content on the sintering behaviors and mechanical properties of the FeB-Fe system hard materials is investigated. The FeB with 10vol.% Fe compact prepared under different temperature is further investigated to evaluate whether Fe is an appropriate binder phase for FeB or not.

Chapter 3 introduces the FeB-Ni system hard materials prepared by electroless plating and spark sintering process. The effect of electroless plating process on the Ni content, Ni distribution and surface morphologies of the FeB-Ni powders are investigated. The sintering behaviors and mechanical properties of FeB with 5, 10, 25 an 30vol.% Ni prepared by the optimized plating process are investigated to determine the suitable Ni content. And then the effect of the sintering parameters on the microstructure and mechanical properties of FeB with suitable Ni content compacts are also investigated to obtain fully dense FeB-Ni compacts.

Chapter 4 discusses the potential practical applications for the FeB-Ni system alloys such as the interrupted cutting tests. The pin on disc wear and friction tests are also carried out using the fully dense FeB-Ni compacts. The friction coefficient, wear volume loss and wear ratio of the volume loss of pin vs disc are investigated to evaluate the wear

resistance of FeB-Ni compacts. The interrupted cutting tests are carried out to measure the cutting performance of FeB-Ni compacts. Flank wear width (VB) is measured as a function of cutting length with different cutting speeds. The wear resistance and cutting performance of WC-7.8Co are also measured as reference.

References

1) M.C. Shaw. Metal Cutting Principles, second ed., Oxford University Press, New York, 2005.
2) V.P. Astakhov. Tribology of Metal Cutting, ScienceDirect (Online service), first ed., Elsevier, Amsterdam, San Diego, CA, 2006.
3) M. Binder, F. Klocke and B. Doebbeler. Simul Model Pract Theory, 2017,70, 65–82.
4) W. Grzesik. Advanced machining processes of metallic materials: theory, modelling and applications. Elsevier, 2008, 163-164.
5) M. Lee, J. Horne, and D. Tabor. The mechanism of notch formation at the depth of cut line of ceramic tools machining nickel base superalloys, Proceedings of the International Conference on Wear of Materials, ASME, New York, 1979, 460–469.
6) V. P. Astakhov and J. C. Outeiro. Modeling of the contact stress distribution at the tool-chip interface. In Proceeding of the 7th CIRP International Workshop on Modeling of Machining Operations, ENSAM, Cluny, France, 2004.
7) B. M. Kramer. On tool material for high speed machining, ASME J. Eng. Ind. 1987,109, 87–91.
8) S. J. Burden, J. Hong, J. W. Rue, et al. Comparison of hot-isostatically -pressed and uniaxially hot-pressed alumina-titanium-carbide cutting tools, Ceramic Bull. 1988, 67, 1003–1005.
9) R. Komanduri and J. D. Desai. Tool Materials for Machining, Technical Information Series, Report No.82CRD220, General Electric, Schenectady, NY, August 1982.
10) T. J. Drozda and C. Wick. Tool and Manufacturing Engineers Handbook: Vol. I-Machining, SME, Dearborn, MI, 1988, Ch. 1.
11) J. R. Davis. ASM Specialty Handbook, Tool Materials (USA: ASM Int.), 1995, 4.
12) G. S. Upadhyaya. Materials science of cemented carbides-an overview. Materials & Design, 2001, 22(6), 483-489.
13) T. Yang, L. Ni, Q. Zheng, et al. Cutting wear, microstructure and mechanical properties of $(Ti_{0.5},W_{0.5})C$-based cermet inserts containing Mo_2C. International Journal of Refractory Metals and Hard Materials, 2017, 68, 151-158.

14) J. Zhao, X. Yuan and Y. Zhou. Cutting performance and failure mechanisms of an Al_2O_3/WC/TiC micro-nano-composite ceramic tool. International Journal of Refractory Metals and Hard Materials, 2010, 28(3), 330-337.

15) I. A. Choudhury and M. A. El-Baradie. Machinability of nickel-base super alloys: a general review. Journal of Materials Processing Technology, 1998, 77(1-3), 278-284.

16) M. Eriksson, M. Radwan and Z. Shen. Spark plasma sintering of WC, cemented carbide and functional graded materials. International Journal of Refractory Metals and Hard Materials, 2013, 36, 31-37.

17) M. F. Huston, G. W. Knobeloch and G. L. Hyatt. Cutting materials, tools, market trends in USA. VDI BERICHTE, 1998, 1399, 21-54.

18) G. Gille, B. Szesny, K. Dreyer, et al. Submicron and ultrafine grained hardmetals for microdrills and metal cutting inserts. International Journal of Refractory Metals and Hard Materials, 2002, 20(1), 3-22.

19) I. Konyashin, F. Schäfer, R. Cooper, et al. Novel ultra-coarse hardmetal grades with reinforced binder for mining and construction. International Journal of Refractory Metals and Hard Materials, 2005, 23(4), 225-232.

20) P. C. Jindal, A. T. Santhanam, U. Schleinkofer, et al. Performance of PVD TiN, TiCN, and TiAlN coated cemented carbide tools in turning. International Journal of Refractory Metals and Hard Materials, 1999, 17(1), 163-170.

21) T. W. Penrice. Alternative binders for hard metals. Journal of Materials Shaping Technology, 1987, 5(1), 35-39.

22) REACH. http://ec.europa.eu/environment/chemicals/reach/reach_intro.htm.

23) S. H. Chang and S. L. Chen. Characterization and properties of sintered WC–Co and WC–Ni–Fe hard metal alloys. Journal of Alloys and Compounds, 2014, 585, 407-413.

24) G. Gille, J. Bredthauer, B. Gries, et al. Advanced and new grades of WC and binder powder–their properties and application. International Journal of Refractory Metals and Hard Materials, 2000, 18(2), 87-102.

25) H. Suzuki. Cemented carbide and sintered hard material foundation and application, Maruzen press, 1986.

26) V. A. Tracey. Nickel in hardmetals. International Journal of Refractory Metals and Hard Materials, 1992, 11(3), 137-149.

27) Trans. Japan-Soviet-Press: Data Book of Compounds with High Melting Temperature, Japan-Soviet-Press, Wakayama, 1977.

28) C. Kapfenberger, B. Albert, R. Pöttgen, et al. Structure refinements of iron borides Fe_2B and FeB. Zeitschrift für Kristallographie-Crystalline Materials, 2006, 221 (5-7), 477-481.

29) A. A.Chaudry. Formation and reactivity of some metal borides and carbides, 1973.

30) Matkovich and I. Vlado. Boron and refractory borides, Springer-Verlag, New York, NY 1977, 797

31) L. G. Yu, X. J. Chen, K. A. Khor, et al. FeB/Fe_2B phase transformation during SPS pack-boriding: boride layer growth kinetics. Acta Materialia, 2005, 53(8), 2361-2368.

32) N. N. Greenwood, R. V. Parish and P. Thornton. Metal borides. Quarterly Reviews, Chemical Society, 1966, 20(3), 441-464.

33) Y. Bai, C. Wu, F.Wu, et al. Investigation of FeB alloy prepared by an electric arc method and used as the anode material for alkaline secondary batteries. Electrochemistry Communications, 2009, 11(1), 145-148.

34) R. Steinitz, I. Binder and D. Moskowitz. System molybdenum-boron and some properties of the molybdenum borides. Trans. AIME, 1952, 983.

35) K. Matsugi, K. Tomigahara, Y. B. Choi et al. Production of hard materials with ubiquitously Fe-B system by spark sintering and their characteristics, Jpn. Soc. Powder Powder Metallurgy, 2011, 58(8), 487-494.

36) K. Matsugi, K. Tomigahara, Y.B. Choi, et al. Spark sintering behaviors on mixtures of Fe-B and Fe powders. J. Jpn. Soc. Powder Powder Metallurgy, 2013, 60(9), 379-386.

37) L. Prakash. Proc. 13th Int. Plansee Seminar, ed. by H. Bildstein and R. Eck, Reutte, Tirol, Austria, 1993,80.

38) M. Oghbaei and O. Mirzaee. Microwave versus conventional sintering: a review of fundamentals, advantages and applications. Journal of Alloys and Compounds, 2010, 494(1), 175-189.

39) S.J.L. Kang. Sintering: densification, grain growth and microstructure. Butterworth-Heinemann, 2004, 3.

40) F. X. Zimmerman. Isostatic pressing offers production advantages for complex shapes. Ceramic industry, 1998, 148(3), 33-37.

41) I. Azcona, A. Ordonez, J. M. Sanchez, et al. Hot isostatic pressing of ultrafine tungsten carbide-cobalt hardmetals. Journal of materials science, 2002, 37(19), 4189-4195.

42) G. Ziegler, J. Heinrich, G. Wötting. Relationships between processing, microstructure and properties of dense and reaction-bonded silicon nitride. Journal of Materials Science, 1987, 22(9), 3041-3086.

43) M. H. Bocanegra-Bernal. Hot isostatic pressing (HIP) technology and its applications to metals and ceramics. Journal of Materials Science, 2004, 39(21), 6399-6420.

44) D. H. Xiao, Y. H. He, M. Song, et al. Y_2O_3-and NbC-doped ultrafine WC–10Co alloys by low pressure sintering. International Journal of Refractory Metals and Hard Materials, 2010, 28(3), 407-411.

45) M. Bhattacharyaa and T. Basak. A review on the susceptor assisted microwave processing of materials. Energy, 2016, 97, 306-338.

46) V. Mamedov. Spark plasma sintering as advanced PM sintering method. Powder Metallurgy, 2002, 45(4), 322-328.

47) Z. A. Munir, U. Anselmi-Tamburini and M. Ohyanagi. The effect of electric field and pressure on the synthesis and consolidation of materials: a review of the spark plasma sintering method. Journal of Materials Science, 2006, 41(3), 763-777.

48) U. Anselmi-Tamburini, S. Gennari, J. E. Garay, et al. Fundamental investigations on the spark plasma sintering/synthesis process: II. Modeling of current and temperature distributions. Materials Science and Engineering: A, 2005, 394(1), 139-148.

49) U. Anselmi-Tamburini, J. E. Garay, Z. A. Munir. Fundamental investigations on the spark plasma sintering/synthesis process: III. Current effect on reactivity. Materials Science and Engineering: A, 2005, 407(1), 24-30.

50) X. Song, X. Liu, J. Zhang. Neck formation and self-adjusting mechanism of neck growth of conducting powders in spark plasma sintering. Journal of the American Ceramic Society, 2006, 89(2), 494-500.

51) D. A. Stephenson and J. S. Agapiou. Metal cutting theory and practice. CRC press, 2016.

Chapter 2

Sintering Behaviors and Mechanical Properties of ubiquitous FeB-Fe Alloys by Elemental Powder Blending and Spark Sintering Methods

2.1 Introduction

Iron borides (FeB/Fe_2B) were expected to substitute the WC-Co hard materials. As low deformable refractory material, it was difficult to achieve full density just using single iron borides. Introducing the binder phase to improve the sinter ability of iron borides was necessary. Fe or Ni from the same transition metal group as Co were chosen as the binder phase. Fe presented a magnetic bcc crystal structure in room temperature, also known as the α-Fe (ferrite). At temperatures above 1185 K and up to 1673 K, α-Fe undergone a phase transition from bcc to fcc, also called γ-Fe (austenite). Fe was a kind of soft metal with low cost. Although the mutual solid solubility between B and Fe was low, two intermetallic compounds Fe_2B and FeB could be formed[1)]. Fe-alloys tended to form martensite, which could improve the properties of the composite[2)]. In addition, Prakash[3)] presented a review of Fe-based binders processing and applications. However, there were few studies on the iron borides with Fe as binder phase. The effect of Fe content on the sintering behavior and mechanical properties of FeB-Fe hard materials were investigated to evaluate whether Fe was suitable as a binder phase for FeB.

2.2 Experiment procedure

2.2.1 Powder preparation

As- received FeB (Fukuda Metal Foil and Powder Co., Ltd.) and Fe powders (DOWA IP CREATION Co., Ltd.) were used as the raw materials. The mean particle size of FeB and pure Fe powders were 45 and 7.7 μm, respectively. The chemical

composition of as-received FeB powder included 78.4% Fe, 19.1% B, 0.04 % C, 0.48% Si, 0.02% P, 0.003% S and 1.9% Al (mass %). The price of FeB powder was about 3000 ¥/kg. While, the price of WC-7.8Co powder was about 20000 ¥/kg which was more expensive than that of as-received FeB powder. As-received FeB powder consisted of FeB, Fe_2B, Fe and B phases. In order to reduce the impurity phase content, as-received FeB powders were ball milled using a planetary ball mill (Fritsch Pulverisette 5) at 150 rpm for 24 hours. The milling was using 500 mL vial and stainless-steel balls with a diameter of 10 mm. The ball to powder weight ratio was 20:1. After ball milling, FeB powders and 10%, 50%Fe powders were elemental powder blended by the same ball mill machine for 1.8 ks at 50 rpm (here after called FeB-10Fe, FeB-50Fe).

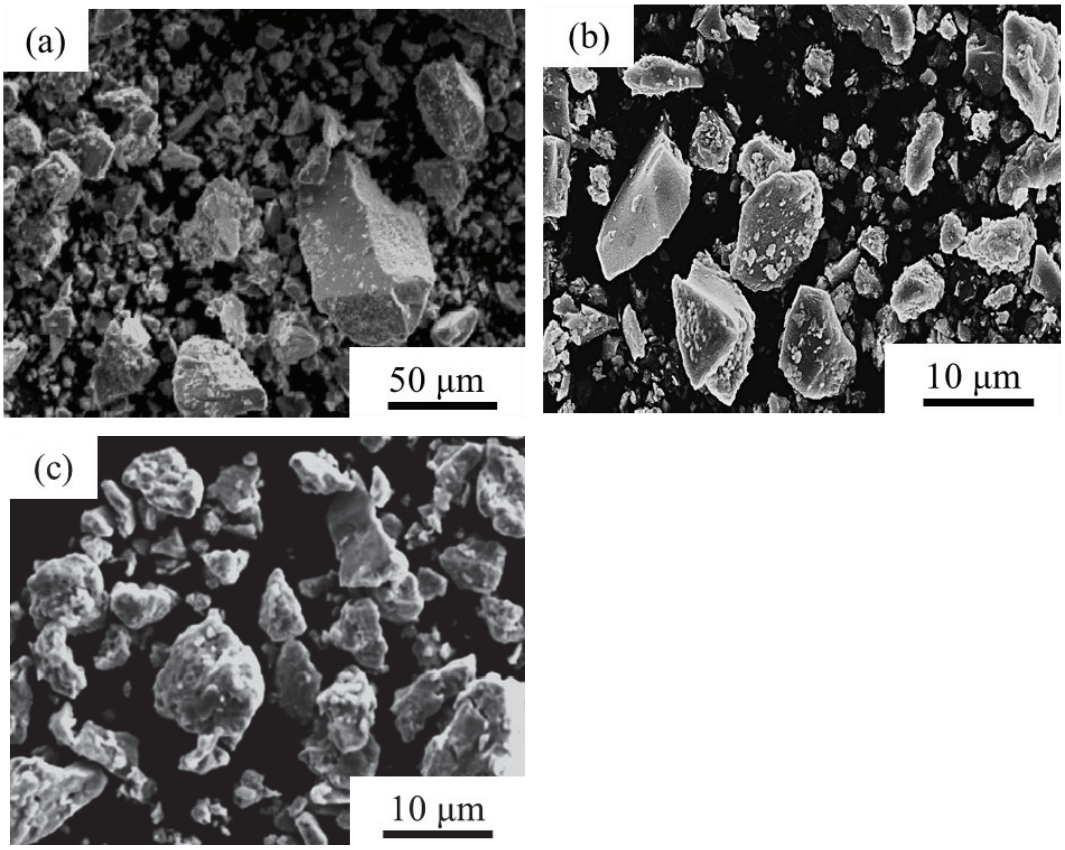

Figure 2.1 SEM images of (a) as-received, (b) ball milled FeB and (c) pure Fe powders.

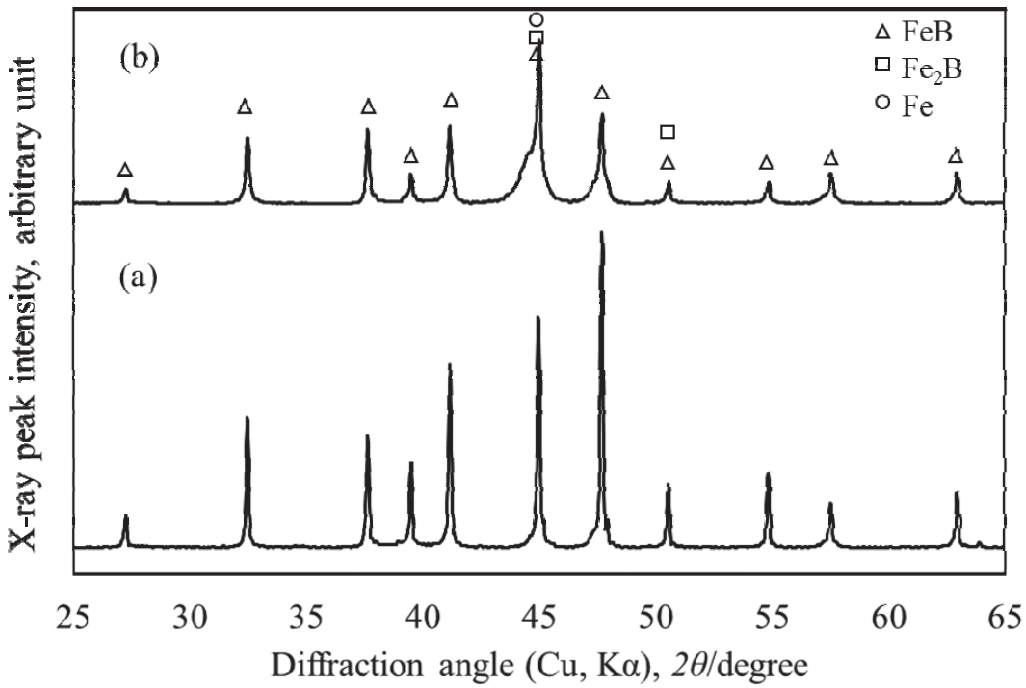

Figure 2.2 X-ray patterns of (a) as-received and (b) ball milled FeB powders.

The SEM images of (a) as-received FeB, (b) ball milled FeB and (c) pure Fe powders were shown in Fig.2.1. As-received FeB powders showed irregular shape and large scale of the size distribution as shown in Fig.2.1(a). The mean particle size of FeB powders rapidly decreased from 45 to 10 μm after ball milling. The scale of the size distribution of FeB powder after ball milling also decreased as shown in Fig.2.1(b). The shape of ball milled FeB powders also showed irregular as well as the Fe powders. No powder agglomeration was observed in these powders.

The X-ray diffraction was carried out to characterize the phase construction of the FeB powders before and after ball milling. Figure 2.2 showed X-ray patterns of as-received and ball milled FeB. The phases of both powders were FeB, Fe_2B, and Fe. It was difficult to detect B phase due to the low content. The predominant phase was FeB. The FeB content was 65 and 77 % for as-received and ball-milled powders, respectively. The Fe_2B and Fe phase content also decreased after ball milling.

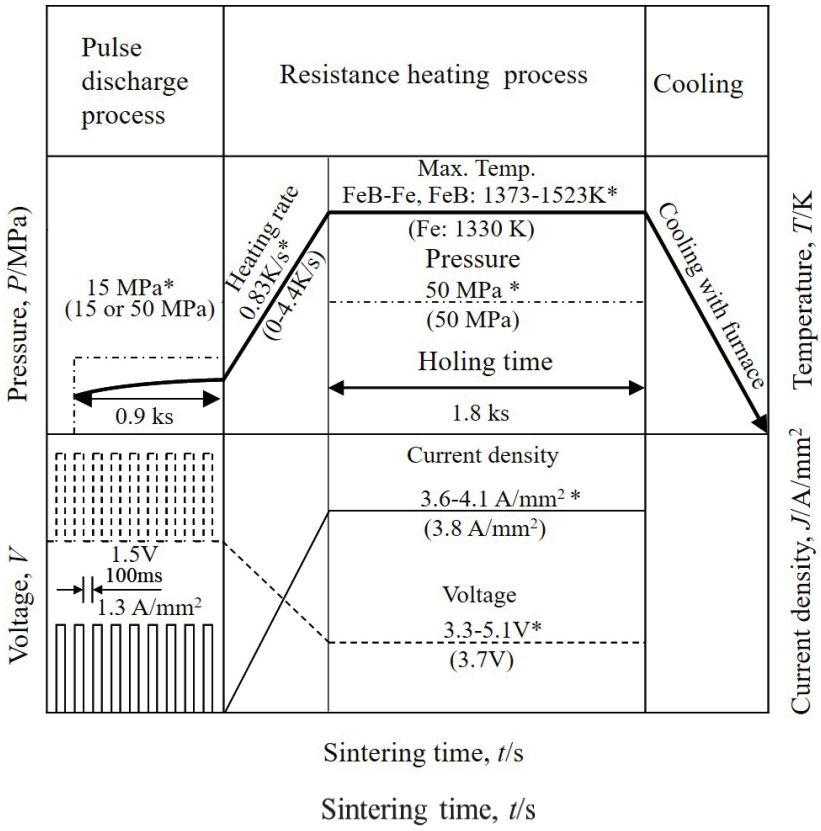

Sintering time, *t*/s

Figure 2.3 Flow chart of spark sintering process. *: from FeB, FeB-10Fe and FeB-50Fe powders, (): from pure Fe powders.

2.2.2 Sintering process of FeB-Fe system powder

During the spark sintering, two graphite punches with diameter of 10 mm and height of 30 mm and a graphite die with an inner diameter of 10 mm, an outer diameter of 40 mm and height of 60 mm were used. The spark sintering process had two modes, pulse discharge sintering mode and resistance heating mode[4]. All the powders were consolidated under a vacuum condition (<10^{-2} Pa). The sintering process was shown in the Fig.2.3. The sintering temperature was measured using a thermocouple (R-type) inserted in the cylindrical of the die. The tip of the thermocouple was about 2 mm away to the compact. The voltage, current, sintering temperature and the displacement of the compact were monitored from a software (Naviwave System, SSAlloy Co., Ltd.) of the spark sintering.

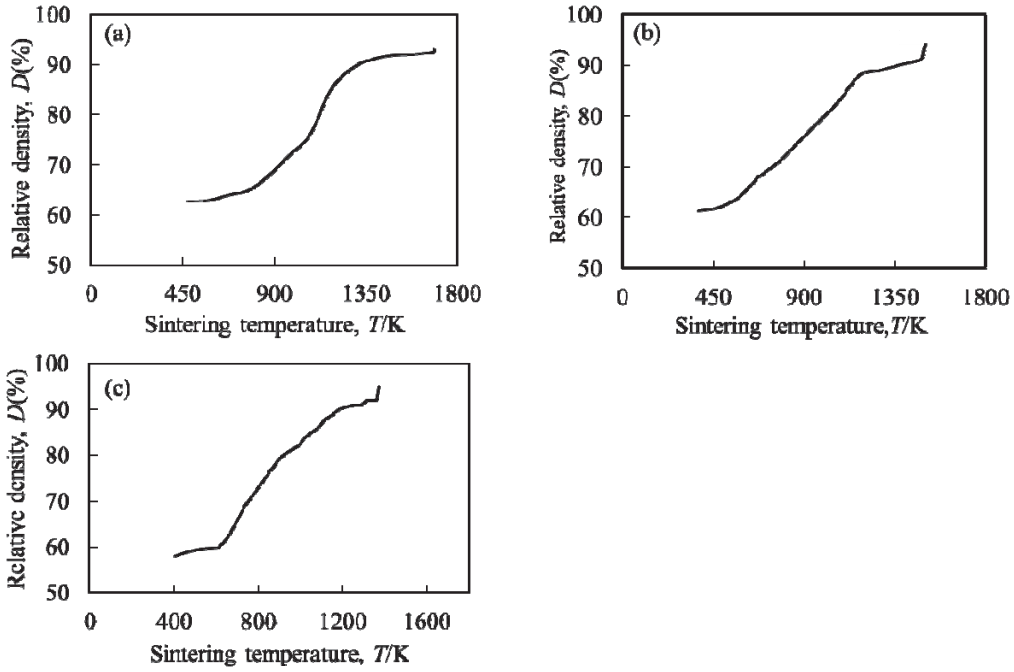

Figure 2.4 Relation between the relative density and sintering temperature of the (a) FeB compact sintered at 1693 K, (b) FeB-10Fe compact sintered at 1493 K and (c) FeB-50Fe compact sintered at 1373 K.

2.2.3 Characterizations of FeB-Fe system compacts

Densities of the compacts were measured by Archimedes' method. Apparent relative density of compacts was calculated based on the displacement of between electrodes, by the height of the compacts dividing the ideally height of 10 mm. Morphology of the powder was measured by scanning electron microscope (SEM, TOPCON SM-520, Japan). Microstructure of the sintered compacts was observed by the optical microscope (Metal Microscope OPTIPHOT-2, Nikon Corporation, Japan). Average grain size and porosity of the compacts were measured by image analysis methods[5]. Phases in the compacts were characterized by X-ray powder diffraction method (XRD, MAC-M03-XHF22, Japan) using Cu Kα radiation (λ=1.5406 Å) at 40 kV and 40 mA. The macro and micro hardness of the compacts were measured by Vickers hardness tester (MHT-1, Japan). Compressive and bending strength of the compacts were measured at room temperature by a mechanical testing machine

(Autograph DCS-R-5000, Shimadzu Corporation, Japan) with a constant crosshead speed of 0.5 mm/min.

2.3 Results and discussion

2.3.1 Effect of the Fe content on the microstructures and properties of the FeB-Fe system compacts

2.3.1.1 Sintering behaviors and microstructures of the FeB-Fe system compacts

Figure 2.4 showed the relation between sintering temperature and relative density of FeB, FeB-10Fe and FeB-50Fe compacts. The relative density of FeB, FeB-10Fe and FeB-50Fe was 92%, 95% and 96%, respectively. As shown in Fig. 2.4 (a), preparation FeB compact with same level relative density to the FeB compact with Fe addition required high sintering temperature. It was considered that FeB materials had low sinterability. With the addition of Fe binder phase, the sintering temperature for producing compacts with the almost same relative density was significantly reduced as shown in Fig. 2.4 (b) and (c). In this case, Fe binder phase was effective to improve the sinterability of FeB as well as energy saving. Furthermore, the sintering temperature to obtain compact with same relative density decreased significantly with the continuous addition of Fe binder phase. As can be seen in this figure, the slop of the FeB-10Fe and FeB-50Fe compacts were higher than that of FeB compact. That means the densification of the FeB-Fe system compacts was increased with the addition of Fe binder phase due to the high ductility of the Fe binder phase.

Figure 2.5 showed the microstructures of FeB, FeB-10Fe and FeB-50Fe compacts. However, after sintering at high temperature for a long time, pores were still observed in the FeB compacts due to the low sinterability as shown in Fig. 2.5 (a). The porosity decreased with the addition of Fe binder phase as shown in Fig. 2.5 (b) and (c). The individual phases in each compact were indicated in this figure. FeB and FeB-10Fe compacts were sintered in liquid phase sintering according to the phase diagram[6]. The appearance of liquid phase promoted grain growth and the diffusion between Fe and B. The eutectic reaction between Fe and Fe_2B occurred between the grain boundaries. The

B phase was still in the FeB compact due to the low content of Fe phase. While, with the addition of 50% Fe binder phase, the B phase still appearance in this compact as shown in Fig. 2.5 (c). It was considered that the reaction between Fe and B was very difficult in low sintering temperature.

Figure 2.6 showed the X-ray patterns of FeB, FeB-10Fe and FeB-50Fe compacts sintering at different temperature. There were FeB, Fe_2B, Fe and B phases in as-received FeB powders. The B phase was difficult to detect due to the low content. The appearance of liquid phase promoted the diffusion between Fe, B, Fe_2B and FeB which caused the variation of constituent phase. In addition, Fe_2B and Fe were precipitated from the liquid phase. Furthermore, the content of Fe_2B phase increased with the addition of Fe binder phase which in contrary to the FeB phase. It was mainly due to the diffusion between the Fe and FeB phases.

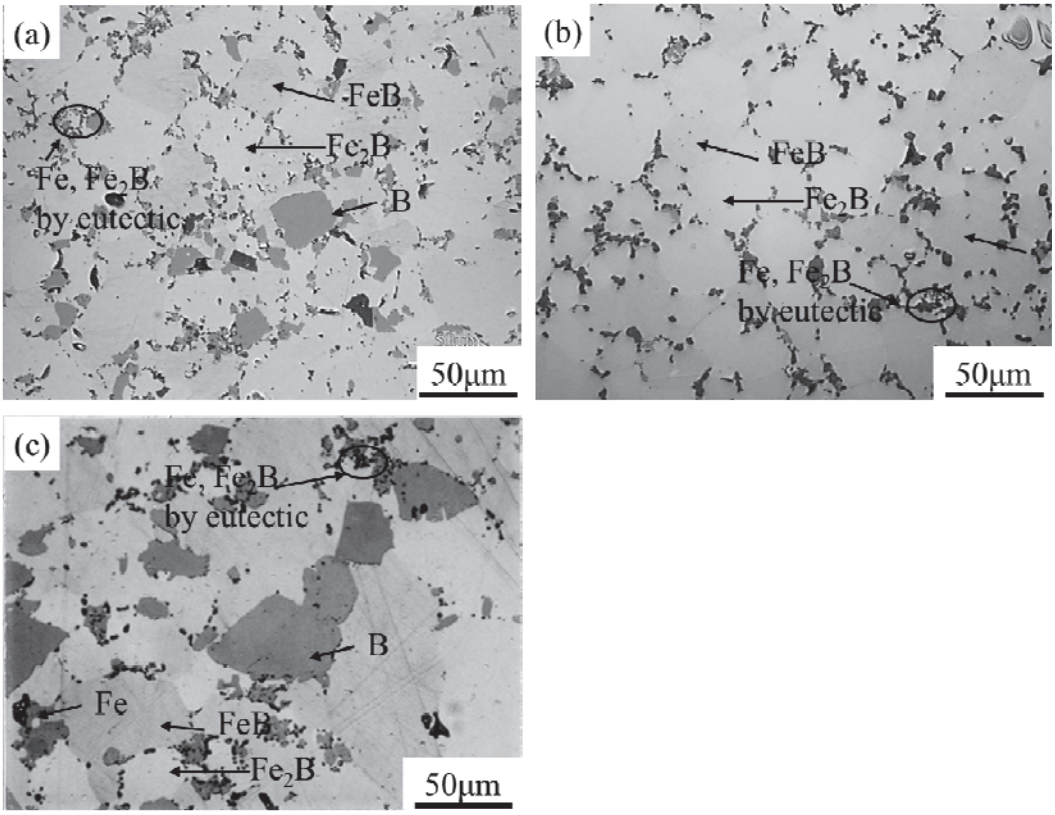

Figure 2.5 Optical micrographs of the (a) FeB, (b) FeB-10Fe and (c) FeB-50Fe compacts sintered at 1693, 1493 and 1373 K, respectively.

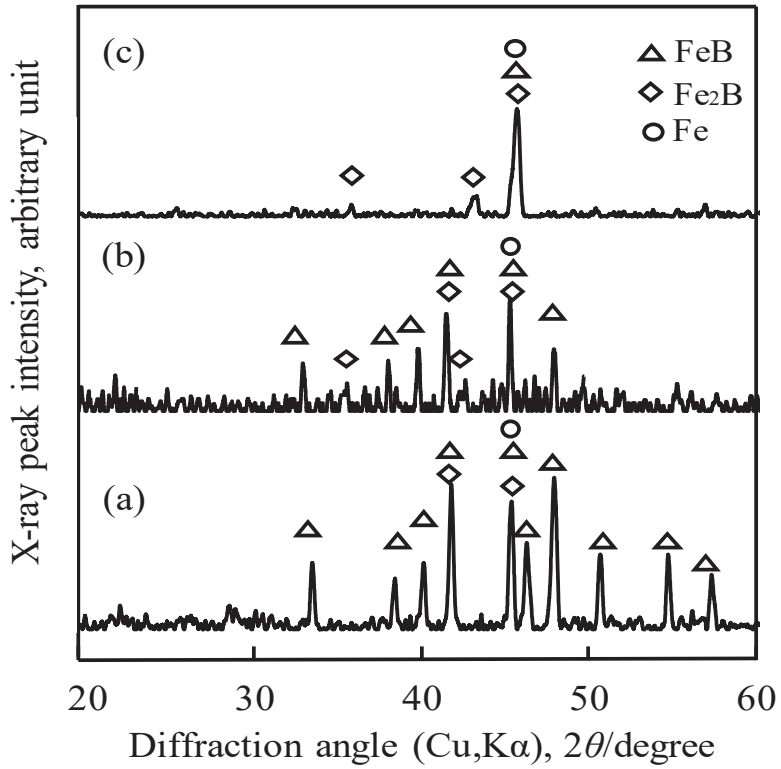

Figure 2.6 X-ray patterns of (a) FeB, (b) FeB-10Fe and (c) FeB-50Fe compacts sintered at 1693, 1493 and 1373 K, respectively.

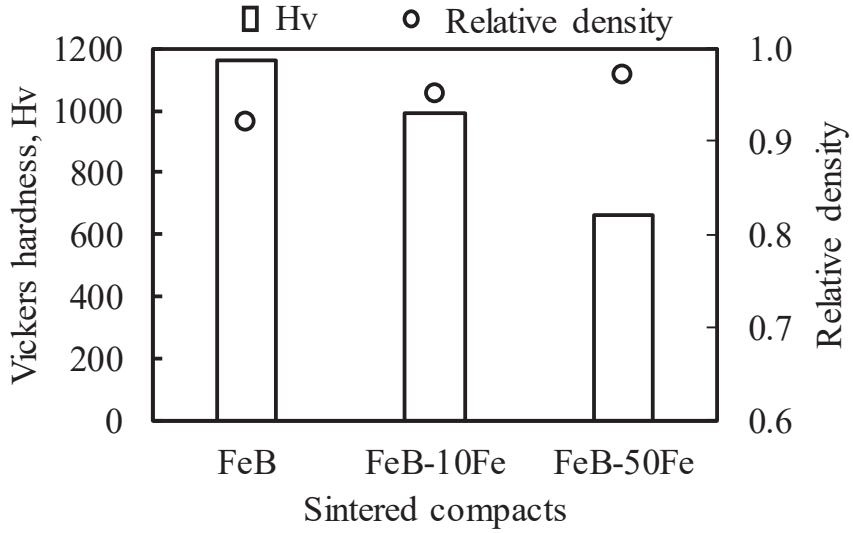

Figure 2.7 Relation between Vickers hardness and relative density of FeB, FeB-10Fe, FeB-50Fe sintered at 1693, 1493 and 1373 K, respectively.

2.3.1.2 Mechanical properties of the FeB-Fe system compacts

Figure 2.7 showed the relation between Vickers hardness and the relative density of FeB, FeB-10Fe and FeB-50Fe sintered at different temperature. The hardness of the sintered compacts was decreased with the increasing of the Fe binder phase. FeB compact with lowest relative density possessed the highest hardness in contrast to the FeB-50Fe compact. For the hard materials, the hardness depended on the relative density. In this case, the high relative density with low hardness was due to the addition of large amount of soft Fe phase. The addition of binder phase should be considered carefully.

Figure 2.8 showed the stress-strain curves obtained from three points bending tests by using FeB, FeB-10Fe, FeB-50Fe compacts. The FeB-50Fe showed the highest bending strength with large strain. The porosity had a great influence on the bending strength. The pores in the sintered compacts became the source of cracks, resulting in the reduction of the bending strength. The porosity would decrease with the increase of the Fe binder phase. Therefore, the bending strength increased with the increasing of the Fe binder phase.

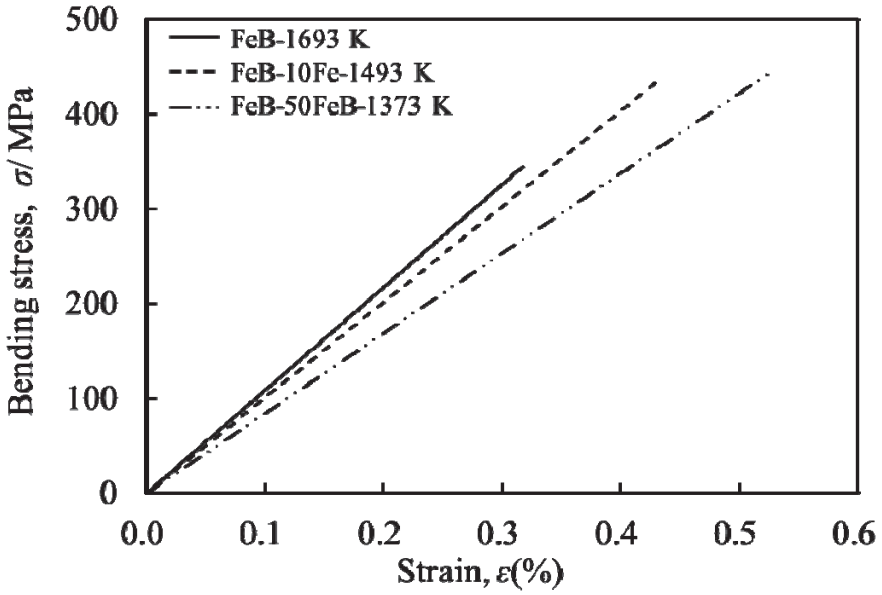

Figure 2.8 The stress-strain curves obtained from three points bending tests by using FeB, FeB-10Fe, FeB-50Fe compacts sintered at 1693, 1493 and 1373 K, respectively.

Overall, the fully dense FeB-10Fe compacts was prepared at low sintering temperature. In addition, the relative density and bending strength of FeB-10Fe was close to that of FeB-50Fe compact. The hardness of FeB-10Fe compact was much higher than that of FeB-50Fe compact. In this case, the addition of 10vol% Fe was suitable for FeB. Therefore, the sintering behavior, microstructure and mechanical properties of FeB-10Fe were further investigated.

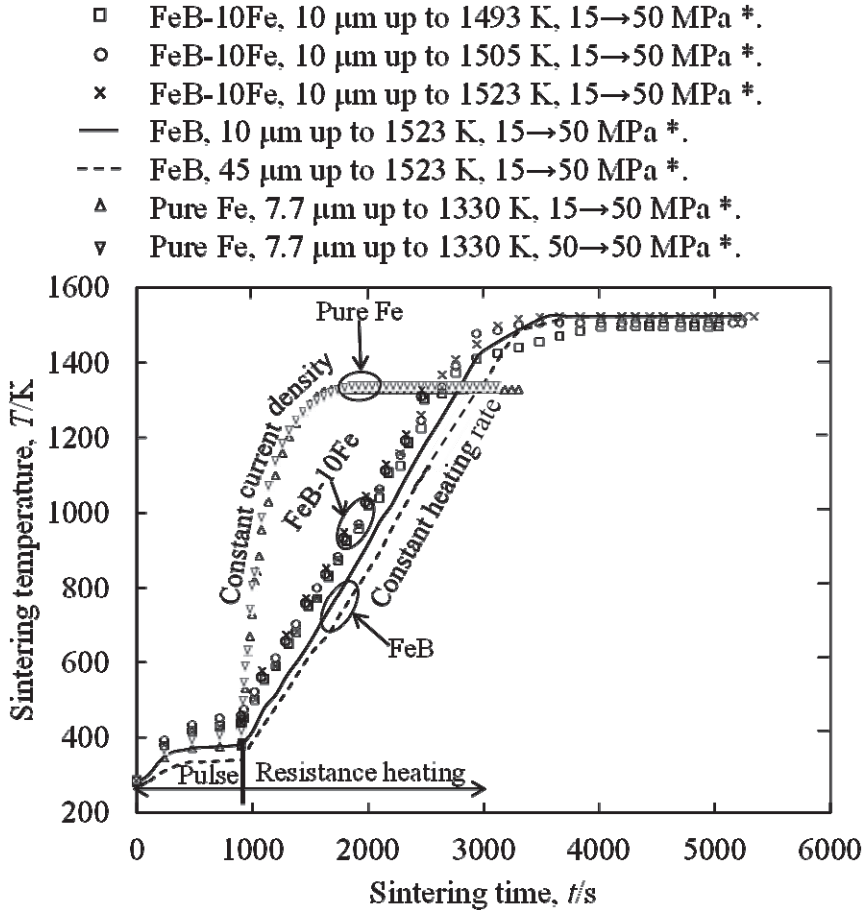

Figure 2.9 Relation between sintering time and sintering temperature of FeB-10Fe sintered at 1493 K, 1505 K and 1523 K, FeB sintered at 1523 K and pure Fe sintered at 1330 K. 15→50 MPa*: Applied pressure in pulse discharge to resistance heating were changed 15 to 50 MPa, respectively. 50→50 MPa*: Applied pressure in pulse discharge to resistance heating were keep constant.

2.3.2 Sintering behaviors, microstructures and mechanical properties of FeB-10Fe compacts

2.3.2.1 Sintering behaviors of FeB-10Fe compacts

The relations between electric discharged time and compact-temperature or apparent relative density by displacement between electrodes were shown in Fig 2.9 and 2.10. There were two heating conditions in constant current values of 3.8 A/mm^2 and constant heating rate of 50 K/min in these figures. The unsteady and steady state of temperature occurred during sintering. The temperatures of compacts depended on their thermal and electrical conductivity, which resulted in the higher and lower values in temperatures for pure Fe and FeB compacts. In contrast, apparent relative densities referred to the nominal relative densities were also increased corresponding to the behaviors in temperature-change. The relative densities to the sintering time of 900 s, were decided depending on the shapes of powders and pressure (15 or 50 MPa). Figure 2.11 showed the relation between the sintering temperature and apparent relative density, which were already shown in Figs 2.9 and 2.10. There were good and poor sinterability on pure Fe and FeB powders, respectively, and FeB-10Fe showed the sintering behaviors between both powders. The slope of sintering curves below about 1260 K for FeB-10Fe compacts was higher than that of FeB compacts using the powders of 45 μm during spark sintering. It was mainly because of the effect of the addition of Fe binder phase. In addition, the slope of the sintering curve of FeB powders with 10 μm was higher than that of FeB powders with 45 μm because of higher sinterability for the fine size of FeB powders. In other words, the high slope in the sintering curve meant high densification rate in the temperature range.

The sintering behaviors of FeB-10Fe powders in the temperature range below the 1493 K showed good reproducibility, although their maximum temperatures changed from 1493 to 1523 K. The apparent relative density of FeB-10Fe compacts was increased monotonously in the temperature range below this temperature. And then the apparent relative density became almost constant above about 1260 K. Moreover, during holding time at the maximum temperature, the final apparent relative density of FeB-10Fe compacts sintered at 1505 and 1523 K were increased significantly,

compared with FeB-10Fe compact sintered at 1493K. It meant that the sintering at 1505 and 1523 K proceeded at liquid state sintering.

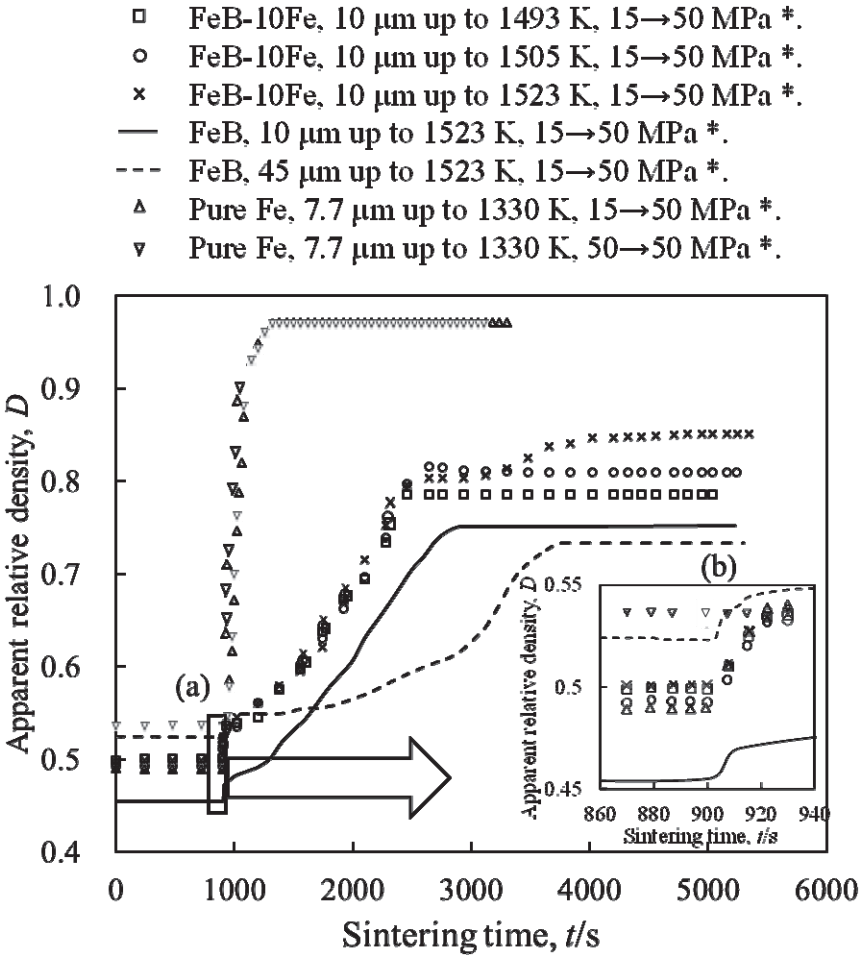

Figure 2.10 Relation between sintering time and apparent relative density of FeB-10Fe sintered at 1493 K, 1505 K and 1523 K, FeB sintered at 1523 K and pure Fe sintered at 1330 K. 15→50 MPa*: Applied pressure in pulse discharge to resistance heating were changed 15 to 50 MPa, respectively. 50→50 MPa*: Applied pressure in pulse discharge to resistance heating were keep constant. Insert (b) was the enlargement of the square area of (a).

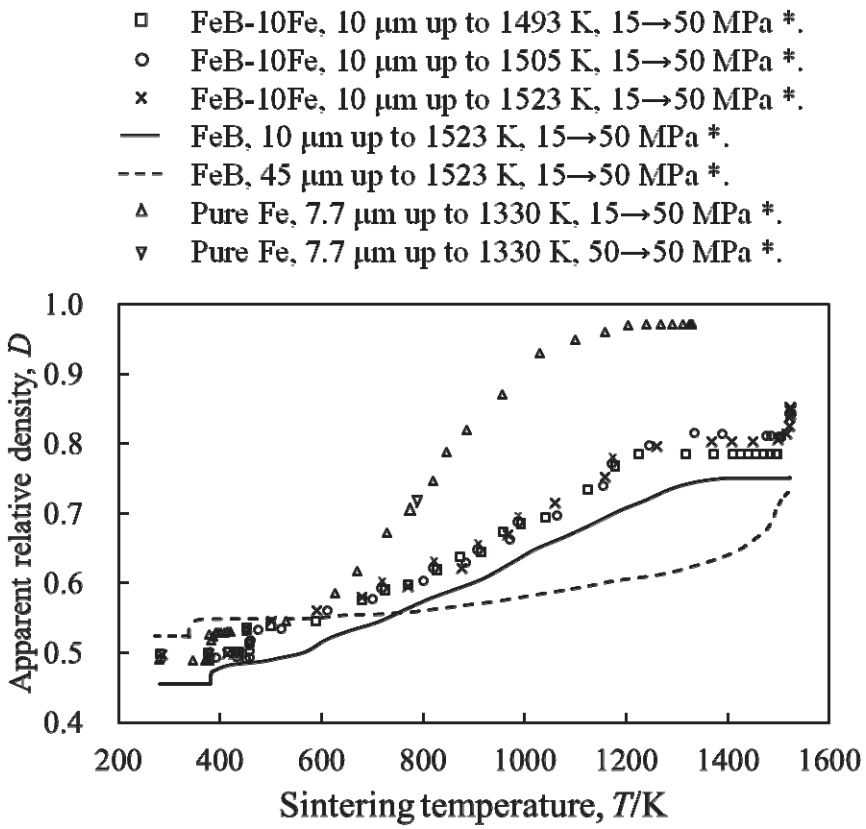

Figure 2.11 Relation between sintering temperature and apparent relative density of FeB-10Fe sintered at 1493 K, 1505 K and 1523 K, FeB sintered at 1523 K and pure Fe sintered at 1330 K. 15→50 MPa*: Applied pressure in pulse discharge to resistance heating were changed 15 to 50 MPa, respectively. 50→50 MPa*: Applied pressure in pulse discharge to resistance heating were keep constant.

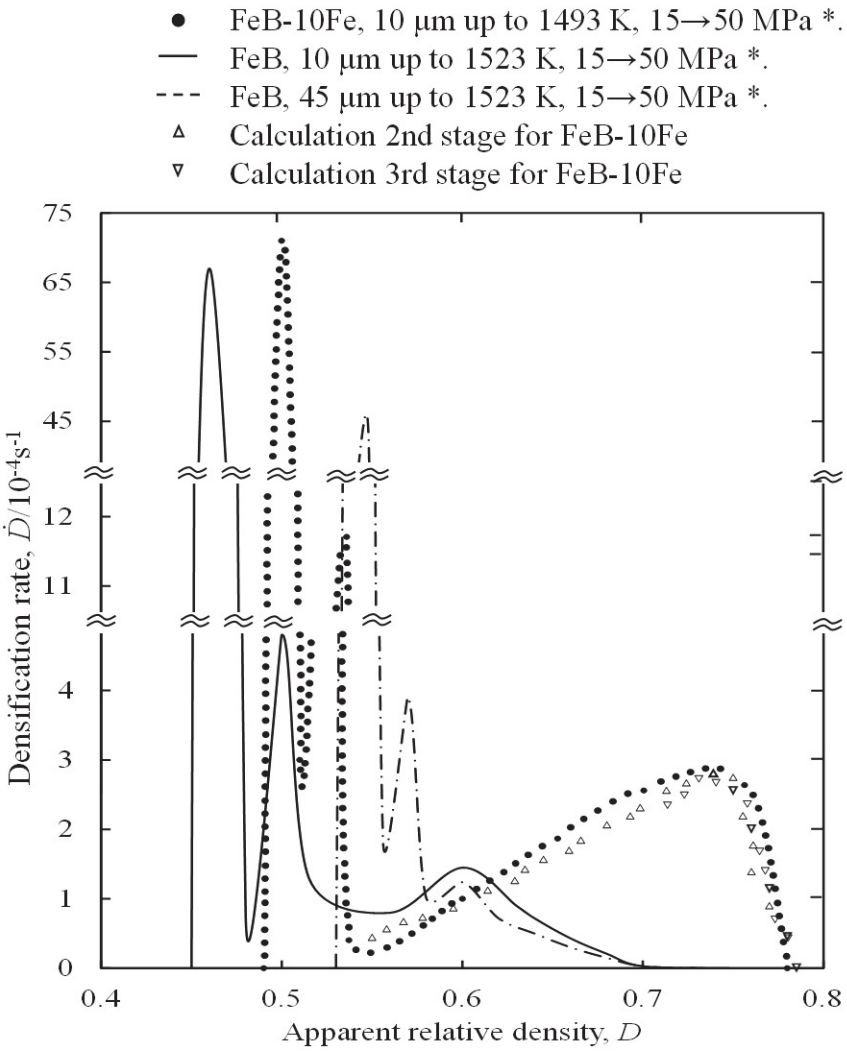

Figure 2.12 Relation between densification rate and apparent relative density of FeB-10Fe sintered at 1493 K, FeB sintered at 1523 K and the calculation results of Ḋ for FeB-10Fe compact. 15→50 MPa*: Applied pressure in pulse discharge to resistance heating were changed 15 to 50 MPa, respectively.

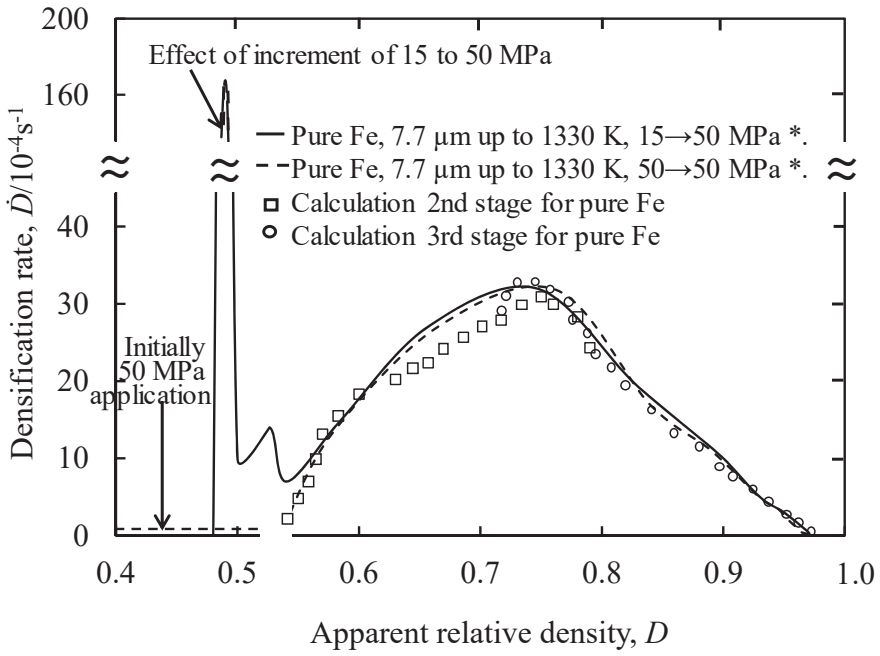

Figure 2.13 Relation between densification rate and apparent relative density of pure Fe sintered at 1330 K and the calculation results of $\dot{D}$ for pure Fe compact. 15→50 MPa*: Applied pressure in pulse discharge to resistance heating were changed 15 to 50 MPa, respectively. 50→50 MPa*: Applied pressure in pulse discharge to resistance heating were keep constant.

In order to investigate the mechanism of densification in spark sintering process, the densification rate of FeB-10Fe, FeB and pure Fe powders were obtained experimentally as shown in Figs. 2.12 and 2.13. The densification rate was obtained by dividing the apparent relative density, *dD*, increment by time increment, *dt*.

$$\dot{D} = dD / dt \quad (1)$$

where D and t were currently apparent relative density and time, respectively. Three peaks of $\dot{D}$ showed at D of 0.49, 0.52 and 0.76 for pure Fe compacts as shown in Fig.1.12. The highest densification rate was found in the curve for pure Fe compacts which was applied to 50 MPa after 15 MPa application in pulse discharge. In contrast, in the $\dot{D}$ curves of pure Fe which was initially 50 MPa applied, no peaks appeared in the initial stage in below 0.5 D. It was considered that the rearrangement of the particles by increment of the pressure resulted in the firstly high densification rate in D of

approximately 0.5 showing the start of resistance heating. The secondary peak of $\dot{D}$ at the D of 0.52 was caused by the particle-rearrangement due to the plastic deformation in local heat generated areas between particles at a little higher temperature.

There also were three peaks of $\dot{D}$ at D of 0.5, 0.52 and 0.75 for FeB-10Fe in Fig.2.13. The values in $\dot{D}$ peaks and the final D of FeB were lower than those of FeB-10Fe powders. The deformation of FeB phase could not be expected in this temperature range below 1260 K, as shown in Fig. 2.12. Therefore, the plastic deformation of Fe binder phase caused by Joule's heat generation between particles played a dominant role in increasing the apparent relative density for FeB-10Fe compacts, which meant the increase of relative density from about 0.7 for FeB to 0.8 for FeB-10Fe by the 10 vol.% Fe additions.

Generally, the densification process could be divided into three stages. The first stage was performed in the pulse sintering process. The second and third stages were plastic deformation and power law creep deformation stages[7]. In order to further investigate the sintering mechanism after rearrangement of the particles, the follow eq. (2) as plastic deformation (2nd stage) and the eq. (3) as power law creep deformation (3rd stage) were used for theoretical analysis[7].

$$\dot{D}=\left[\left(\frac{d\sigma_{yield}}{dT}\right)/\left(\frac{d\kappa(D)}{dD}\right)\right]\left(\frac{\kappa(D)}{\sigma_{yield}}\right)\dot{T} \quad (2)$$

$$\dot{D}=AV_{ex}^{m}D\kappa(D)^{n+1}e^{\left(-\frac{Q}{RT}\right)}P^{n} \quad (3)$$

where T, $\dot{T}$, P, σ_{yield}, A, Q, n, m and R were temperature, heating rate of compact, applied pressure, yield stress of powder material, creep constant, activation energy of power law creep, stress exponent, coefficient representing the contribution of macroscopic stress and gas constant respectively. And $\kappa(D)$ was the function of apparent relative density and Vex was an extended volume fraction for densification[9]. In this study, the values of k, m, n and Q were used to be 3.5[7], 0.3[7], 4.8[7] and 326 kJ/mol[10], respectively. Assuming σ_{eq} was equal $\sigma_{0.2}$, the relationship between 0.2 % proof stress and temperature of pure Fe was obtained by high temperature tensile tests. In our laboratory, the densification processes of Cu and mixture powder of Cu and Al_2O_3 were investigated by experiments and theoretical calculation of the $\dot{D}$ using the eq. (2) and (3) mentioned above[11-13]. The experimental results were consistent with the

estimated results calculated by equations (2) and (3) for Cu and Cu+Al_2O_3. It was considered that plastic deformation of the Cu powders occurred before reaching maximum point of the $\dot{D}$ at the D of approximately 0.7～0.75. The power law creep deformation of Cu powders occurred after that.

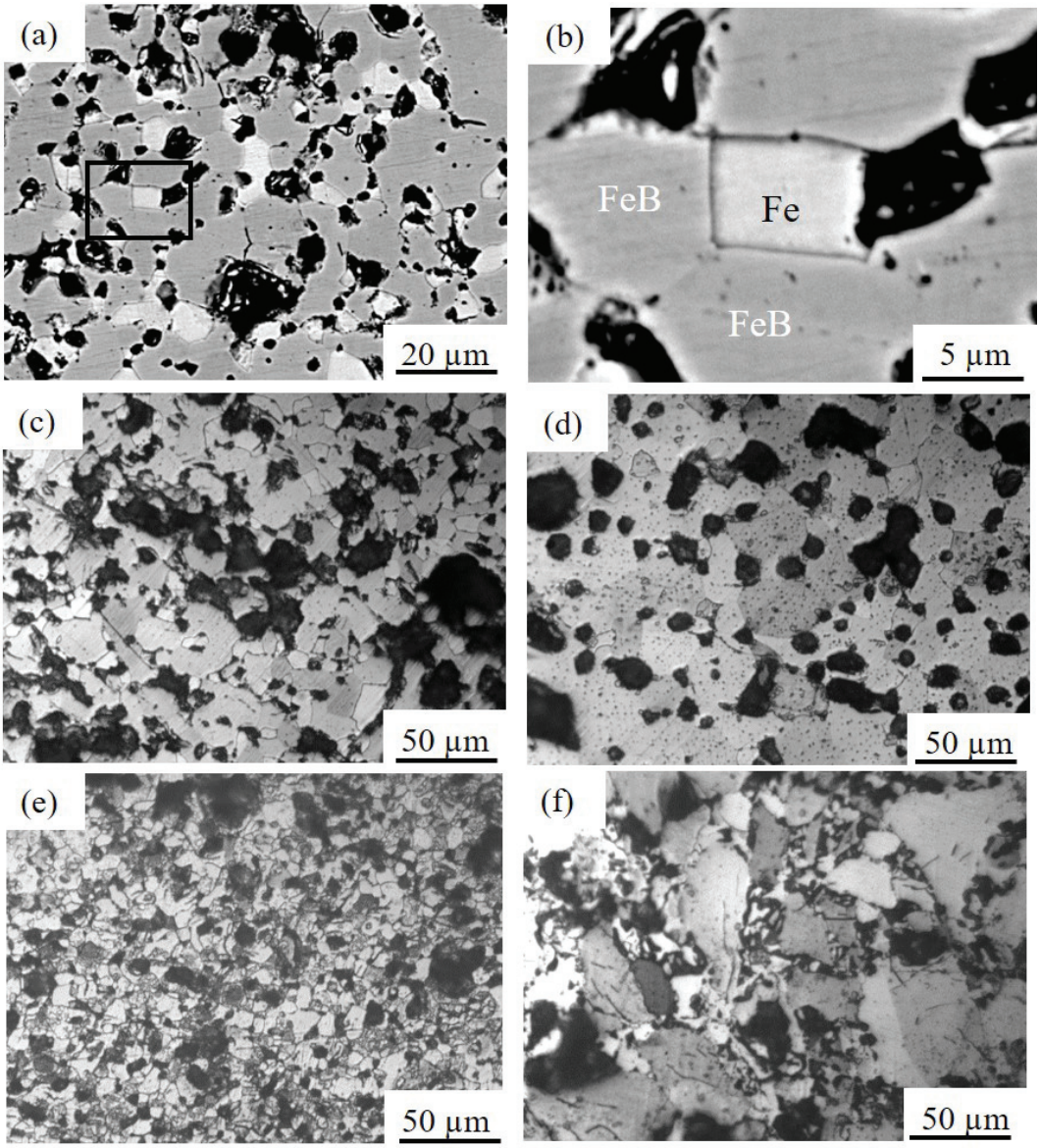

Figure 2.14 Compositional microstructures of FeB-10Fe compacts sintered at (a) 1493 K, (c) 1505 K and (d) 1523 K, FeB compacts using powders of (e) 10 and (f) 45 μm sintered at 1523 K. (b) was the enlargement of the square area of (a).

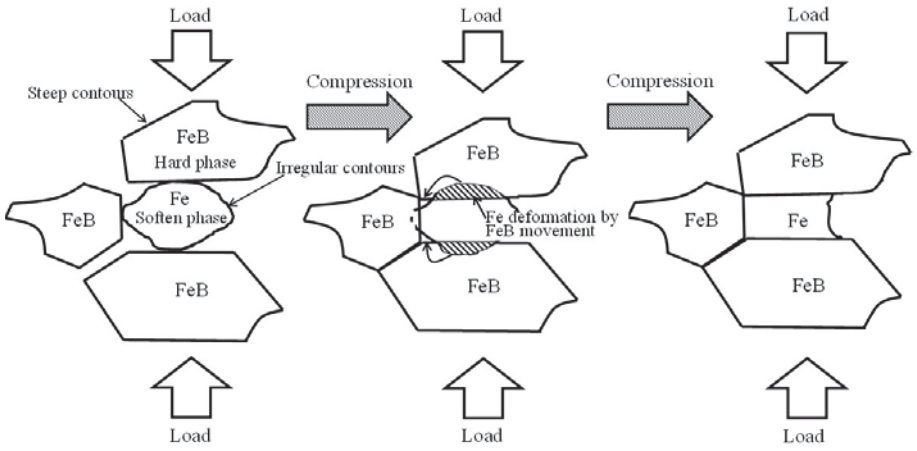

Figure 2.15 Deformation process of Fe binder around FeB powders at lateral pressure condition as seen in Fig. 2.14 (b).

In this study, the experimental results of $\dot{D}$ both of pure Fe and FeB-10Fe compacts were consistent with the estimated results using equations (2) and (3), as shown in Fig.2.12 and 2.13. Therefore, it was considered that the increment of the densification rate of FeB-10Fe compacts was caused by the plastic deformation of Fe binder phase before reaching maximum point of the $\dot{D}$ at the D of 0.75. After that power law creep deformation of Fe binder phase occurred above D of 0.75.

The morphologies of the FeB-10Fe compact sintered different temperature were shown in Fig.2.14. The Fe phase with steep shaped grain boundary was observed in FeB-10Fe compacts which corresponded to the morphologies of pure Fe and FeB particles showed in Fig.2.1. As shown in Fig.2.14(b), it was considered that the plastic deformation of Fe phase and movement of the FeB hard particles toward the Fe phase were performed together in the plastic deformation of the 2nd stage. This phenomenon was illustrated as shown in Fig.2.15. The plastic deformation of the Fe phase surrounded by the FeB hard phase was largely caused to the higher temperature of 1100 K showing the D of 0.75, seen in Fig.2.12 and 2.13, because of just 10 vol.% Fe contents in the uniaxial die press at the lateral pressure condition. However, it was interesting that exchanging value of the D from plastic deformation to powder law creep deformation was shown to be approximately 0.76, even for the different powders and various binder contents.

2.3.2.2 Microstructures of the FeB-10Fe compacts

Figure 2.14 showed the microstructures of FeB-10Fe compacts sintered at 1493 K, 1505 K and 1523 K, FeB compacts using powders of 10 and 45 μm sintered at 1523 K. In addition, The enlarged image of the deformation of Fe binder phase was also shown. The average sizes of pores in FeB-10Fe compacts sintered at 1493, 1505 and 1523 K were 9.7, 13.6 and 15.7 μm, respectively. Moreover, the shape of pores in FeB-10Fe compacts gradually changed from the irregular shape to round shape with the increment of sintering temperature. The state of pores also gradually changed from continuous state to isolated state. It was mainly because the much more liquid phase consisting of Fe and Fe_2B in FeB-10Fe compacts sintered above 1505 K was appeared during the holding time according to the sintering curves of Fig.6. As reference, the average size of pores of FeB compacts using 10 and 45 μm size powders were 15.9 and 19.1 μm. As shown in table 2.1, the porosities of FeB-10Fe compacts were increased with the increment of sintering temperature. This attributed to the liquid phase in FeB-10Fe compacts squeezed out from die during holding time at 1505 K and 1523K because of the poor wettability between liquid phase and FeB[14].

Table 2.1 Average grain sizes, porosity and density of FeB-10Fe compacts sintered at 1493 K, 1505 K and 1523 K and FeB compacts using 10 and 45 μm size powders sintered at 1523 K.

Powders	Sintering temperature/K	Average grain size/μm	Porosity(%)	Density /×10^{-3} kg/m^3
FeB-10Fe with 10μm	1493	9.7	19	6.18
	1505	13.8	25	6.16
	1523	18.1	29	6.07
FeB with 10μm	1523	11.3	28	6.01
FeB with 45μm	1523	50.1	31	5.88

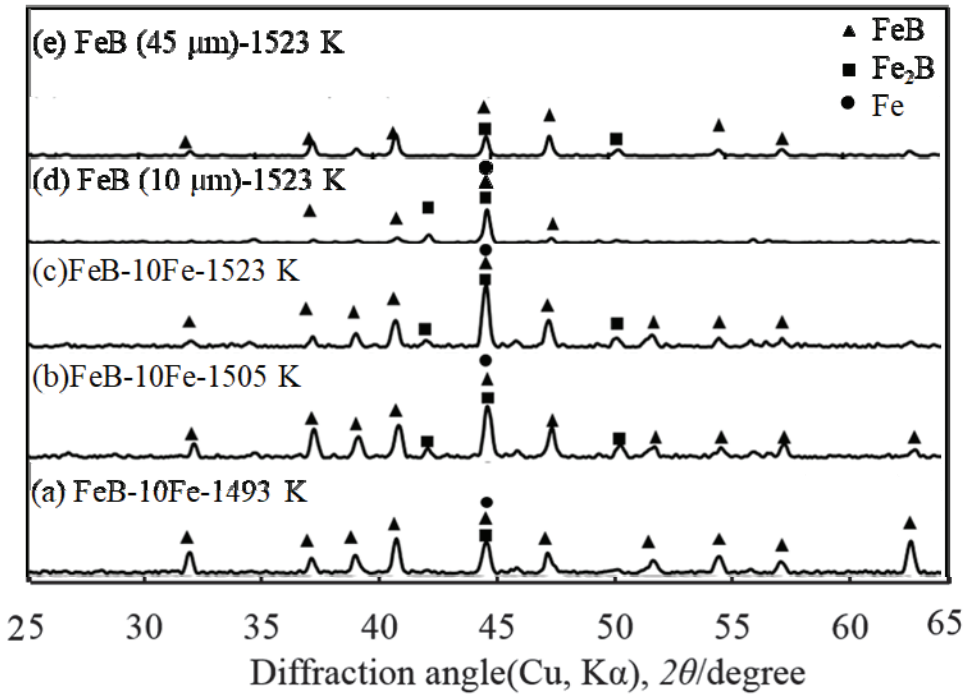

Figure 2.16 XRD patterns of FeB-10Fe compacts sintered at (a) 1493, (b) 1505 and (c) 1523 K and FeB compacts using powders of (d) 10 and (e) 45 μm sintered at 1523 K.

The densities of FeB-10Fe compacts measured by Archimedes' method were shown in table 2.1. The increment of the porosity with the sintering temperature resulted in the decrease of the densities of FeB-10Fe. As reference, the porosities and densities of FeB compacts using powders of 10 and 45 μm were also shown in table 2.1. It was found that manufacturing of compacts using fine particle size of FeB contributed to decrease the porosity compared that of FeB compacts using large particle size powders. The average grain sizes of FeB-10Fe compacts were slightly increased as the sintering temperatures were increased, compared with average particle sizes of starting powder, as shown in table 2.1. High sintering temperature promoted the atomic diffusion between particles, and the liquid phase resulted in the further grain growth of FeB-10Fe compacts.

Figure 2.16 showed the XRD patterns of FeB-10Fe compacts sintered at 1493, 1505 and 1523 K and FeB compacts using powders of 10 and 45 μm sintered at 1523 K. As shown in the XRD patterns, the mainly phase of FeB-10Fe and FeB compacts was

FeB phase. And the contents of FeB phase in the FeB-10Fe compacts sintered at 1493, 1505 and 1523 K were 78, 85 and 90%, respectively. It was considered that the increment of the sintering temperature promoted the atomic diffusion, which resulted in the increment of FeB amount.

2.3.2.3 Mechanical properties of FeB-10Fe compacts

Figure 2.17 showed Vickers hardness of FeB-10Fe compacts sintered at 1493, 1505 and 1523 K and FeB compacts sintered at 1523 K. The hardness of FeB-10Fe compacts sintered at 1493 K was higher than that of compacts sintered above 1505 K. It was mainly because the mean densities of FeB-10Fe compacts were decreased with increment of sintering temperature. Moreover, the grain coarsening in FeB-10Fe compacts sintered above 1505 K corresponded to the decrement of the hardness. Moreover, the hardness of FeB compacts with 10 and 45 μm powders sintered at 1523 K were 960 and 916, respectively. As mentioned above, the FeB compacts using small size powder sintered at 1523 K possessed the smaller porosity and lager mean density, which resulted in the increment of hardness of FeB compacts. On the other hand, the hardness of FeB-10Fe compact sintered at 1493 K was close to that of FeB compact using 10 μm size powders sintered at 1523 K. The hardness of FeB compact mainly depended on the porosity. The porosity of FeB-10Fe compact sintered at 1493 K was lower than that of FeB compact using 10 μm size powders sintered at 1523 K. However, the hardness of FeB-10Fe compact sintered at 1493 K was not high, because of the addition of 10vol.% Fe binder (Hv 0.608 GPa). Therefore, the hardness of FeB-10Fe compact sintered at 1493 K was close to that of FeB compact (Hv 16.5 GPa) using 10 μm size powders sintered at 1523 K.

Figure 2.18 showed Vickers hardness at the interfaces of FeB/FeB, FeB/Fe_2B and Fe_2B/Fe_2B in FeB-10Fe compacts. Vickers hardness values–of FeB and Fe_2B intra-grains in FeB-10Fe compacts were 16.5 and 12.0 GPa, which were consistent with hardness values in the literature[14]. As shown in Fig.13, Vickers hardness values of some interfaces in FeB-10Fe compacts sintered at 1505 and 1523 K were higher than that of compacts sintered at 1493 K. It was because the higher sintering temperature promoted the diffusion of atoms between grains, which resulted in the increment of the

interface-hardness between grains. It was probable that the atomic diffusion coefficients of Fe and B atoms in the interface of FeB/FeB and Fe_2B/Fe_2B grains were different, which should be studied more in the future. In addition, the Vickers hardness of the interfaces of FeB/FeB and Fe_2B/Fe_2B in FeB-10Fe sintered at 1523 K was close to the hardness of their intra grains. It was considered that the atomic diffusion was well completed at 1523 K.

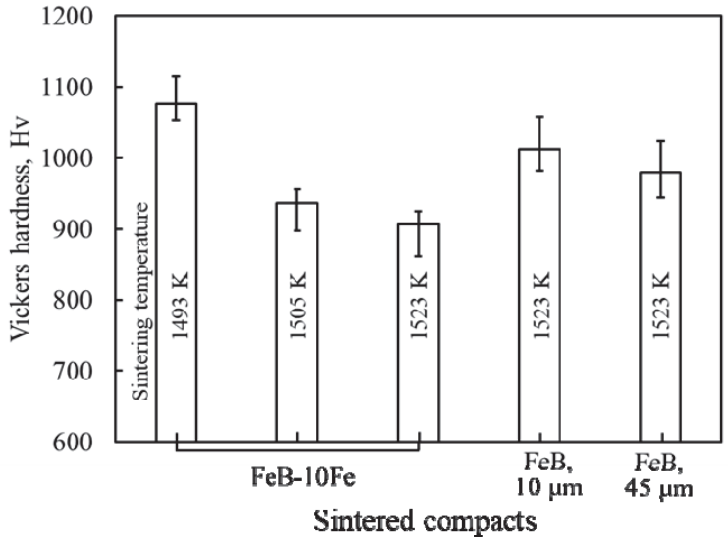

Figure 2.17 Vickers hardness of FeB-10Fe compacts sintered at 1493 K, 1505 K and 1523 K and FeB compacts using powders of 10 and 45 μm sintered at 1523 K.

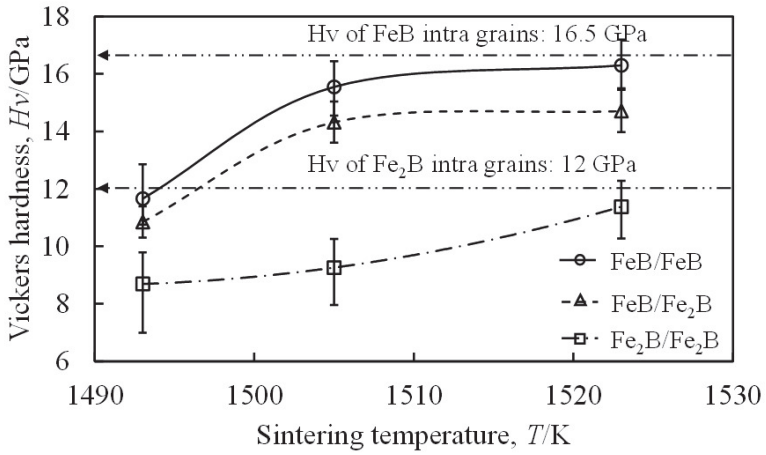

Figure 2.18 Vickers hardness of the interfaces of FeB/FeB, FeB/Fe_2B and Fe_2B/Fe_2B in FeB-10Fe compacts. The inserted dotted lines showed the Vickers hardness of FeB and Fe_2B intra grains.

Figure 2.19 showed the compressive stress-strain curves of FeB-10Fe compacts sintered at 1493, 1505 and 1523 K. As shown in Fig.2.19, the maximum compressive stress and strain of compacts were increased with increment of the sintering temperature. Moreover, the maximum compressive stress of FeB-10Fe compacts sintered at 1523 K with larger grain size and high porosity were larger than that of compacts sintered at 1493 K. It was considered that the high strength between grains in compacts sintered at high sintering temperature resulted in the increment of compressive stress and strain. However, Young's modulus of compacts was decreased with increment of the sintering temperature. The porosity of FeB-10Fe compacts sintered at 1493 K, 1505 K and 1523 K were 18%, 25% and 29%, respectively. The high porosity resulted in the decrement of Young's modulus[16]. In addition, the average grain size of FeB-10Fe compacts sintered at 1493 K, 1505 K and 1523 K were 9.7 μm, 13.8 μm and 18.1 μm, respectively. The large grain size also resulted in the decrement of Young's modulus of FeB-10Fe compacts[17].

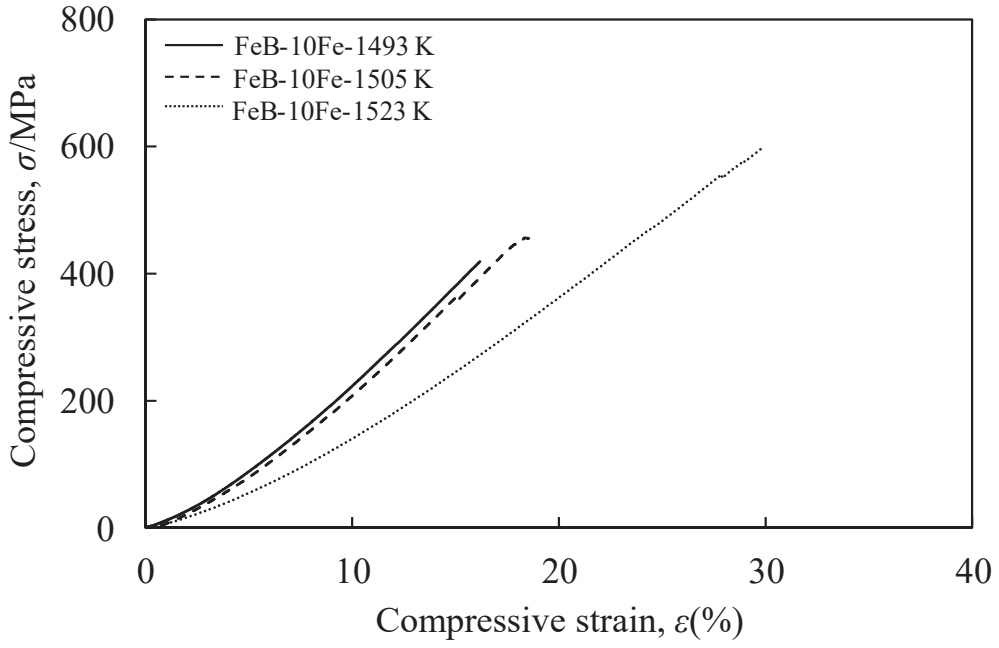

Figure 2.19 Compressive stress-strain curves of FeB-10Fe compacts sintered at 1493 K, 1505 K and 1523 K.

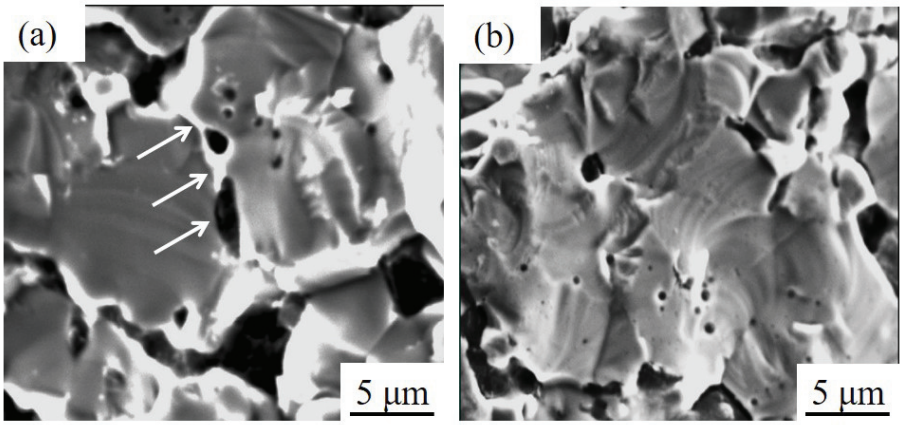

Figure 2.20 SEM images of fracture surfaces of FeB-10Fe compacts sintered at different temperatures: (a) 1493 K and (b) 1523 K. The pores and bonded part of the grain boundary were indicated by the arrows.

Figure 2.20 showed the SEM images of fracture surfaces of FeB-10Fe compacts sintered at 1493 K and 1523 K. As shown by arrows in Fig.2.20, grain boundaries with many pores were clearly observed in the FeB-10Fe compacts sintered at 1493K indicating the insufficient atomic diffusion. In contrast, no obviously pores were observed in the interface between grain boundary in the FeB-10Fe compacts sintered at 1523 K indicating the sufficient atomic diffusion. It was considered that the grain boundary strength was increased with the increment of the sintering temperature. As a result, the compressive stress and strain of FeB-10Fe compacts increased with the increment of the sintering temperature because of strength between FeB/FeB grains which corresponded to that of compressive tests as shown in Fig.2.19.

2.4 Summary

In this chapter, the spark sintering behaviors and mechanical properties of FeB-Fe system alloys were investigated. The summaries were shown below.

(1) FeB with 0, 10 and 50% Fe alloys were successful prepared by spark sintering process. The sinterability of FeB was significantly improved by the addition of Fe binder phase. FeB-10Fe alloy showed high relative density, hardness and bending strength. In this case, the FeB alloy with 10 vol% was optimum.

(2) The relative density of FeB-10Fe compacts increased with the increment of the sintering temperature of 1493 K to 1523 K. FeB-10Fe alloys sintered at different temperature showed the same sintering behaviors according to the sintering and densification rate curves. The densification rate, $\dot{D}$, of FeB-10Fe and pure Fe were obtained theoretically and experimentally, and its maximum point of $\dot{D}$ was shown in the D of approximately 0.75. The plastic deformation and power law creep deformation of Fe binder phase in FeB-10Fe compacts occurred before and after reaching maximum point of $\dot{D}$, respectively. The experimental and theoretical results were in good agreement.

(3) The hardness of FeB-10Fe compacts decreased with increment of sintering temperature because of the increment of porosities in FeB-10Fe compacts. While, the values of micro hardness on the interfaces between grains increased with increment of sintering temperature, because of the promotion of atomic diffusion between particles. There were maximum values of compressive stress and strain on compacts sintered at highest temperature, also because of promotion of the sintering in the interfaces between grains.

(4) Although FeB-10Fe compacts sintered at 1493 K showed high relative density and well mechanical properties, a large number of pores still existed in this compact due to heterogeneous of the Fe binder phase. In this case, Fe was not suitable as binder phase of FeB.

References

1) Massalski, B. Thaddeus, et al. Binary alloy phase diagrams. Vol. 1. No. 2. Metals Park, American society for metals, 1986, 480-483.
2) S. Norgren, J. García, A. Blomqvist, et al. Trends in the P/M hard metal industry. International Journal of Refractory Metals and Hard Materials, 2015, 48, 31-45.
3) L. Prakash and B. Gries. WC hardmetals with iron based binders, Proc 17th International Plansee Seminar, Reutte, Vol. 2, Austria, 2009.
4) K. Matsugi, K. Tomigahara, Y. B. Choi, et al. Production of hard materials with ubiquitously Fe-B system by spark sintering and their characteristics, Jpn. Soc. Powder Powder Metallurgy, 2011, 58(8), 487-494.
5) D. Zhang, K. Sugio, K. Sakai, et al. Effect of spatial distribution of SiC particles on the tensile deformation behavior of Al-10vol% SiC composites. Materials transactions, 2007, 48(2),171-177.
6) T. B. Massalski, H. Okamoto, P. R. Subramanian, et al. Binary alloy phase diagrams. vol. 3. ASM International, 1990.
7) K. Matsugi, O. Yanagisawa and G. Sasaki. Analysis and control in spark sintering process and its micro-macro modelling. J. Jpn. Soc. Powder Powder Metallurgy, 2009, 56(6), 355-370.
8) A. K. Sinha. Boriding (boronizing). ASM Int handbook, Vol.4 Materials Park, OH, USA, The Materials International Society, 1991, 437-447.
9) Y. Wang, K. Matsugi, O. Yanagisawa. Constitutive equation for cold isostatic compaction of metal powders. J. Japan Inst. Metal, 2002, 66(4), 393-399.
10) Japan Inst. Metals. Kinzoku Data Handbook. (Maruzen) 1993, 10.
11) H. Kuramoto, K. Matsugi, K. Kawahara, et al. Sintering rate of pure copper powder uniaxially compressed in closed die in spark sintering process, J. Japan Inst. Metals, 2002, 66(6), 621-626.
12) K. Matsugi, H. Kuramoto, O. Yanagisawa, et al. A case study for production of perfectly sintered complex compacts in rapid consolidation by spark sintering. Materials Science and Engineering: A, 2003, 354(1), 234-242.

13) H. Kuramoto, K. Matsugi, K. Kawahara, et al. Densification rate of Cu-Al_2O_3 composite in the spark sintering process. J. Japan Inst. Metals, 2003, 67(10), 528-537.

14) T. Tokoro and T. Ono. Development of borides dispersed materials with high values in hardness, wear resistance and heat resistance. R. Shiga Prefecture Industrial Center, 2011, 40-43.

15) R. A. Cutler. Engineering properties of borides: Engineering Materials Handbook, Ceramic and Glasses, vol. 4. (USA: ASM Int.) 1991, 787-803.

16) W. Zhou, Y. Tang, B. Liu, et al. Compressive properties of porous metal fiber sintered sheet produced by solid-state sintering process. Materials & Design, 2012, 35, 414-418.

17) M.G. Loshak and L.I. Aleksandrova. Phys. Metals Metallog. 1967, 12, 993-995.

Chapter 3
Preparation of FeB-Ni Alloys by both Electroless Plating and Spark Sintering Methods

3.1 Introduction

In previous study, FeB with Fe as binder phase consolidated by spark sintering was investigated, where the FeB-Fe powders were mixed by an elemental powder blending method. Although a high apparent relative density was obtained, a large number of pores still occurred between the FeB hard phases which resulted in the decrease of the hardness and compressive strength. It was considered that the heterogeneous distribution of the Fe binder in the FeB–Fe mixed powders resulted in the residual irregular-shaped pores. Although increasing the Fe content could decrease the porosity, the hardness of the compact would significantly decrease. In this case, Fe was inappropriate to be used as the binder phase of FeB hard phase.

Ni as an alternative binder phase had received the most attention. Its face centered cubic structure showed well ductile. In addition, Ni as binder phase in the FeB increased the corrosion resistance. The conventional method of adding binder phase to FeB powders was usually carried out by mechanical mixing for prolonged time. However, the heterogeneity of the mixed FeB and Ni powders would encounter the same problem with FeB and Fe powders. Electroless Ni plating on the FeB particles was introduced to solve the above mentioned drawbacks[1)]. By using this technical, it was expected to obtain homogeneous distribution of Ni over the entire substrate surface[2, 3)]. This technical did not require a current supply and set no limits on the shape and type of substrate[4, 5)]. However, electroless Ni plating on powders may be very different from that on bulk materials.

Powders had much higher specific surface area than the bulk materials. High

specific surface area would form large autocatalytic oxidation – reduction reaction interface and accelerate the reaction, which resulted in the rapidly changing of the pH, the heavy consumption of metal ions and decomposition of the bath[6]. Furthermore, high specific surface area with large surface activity was easily resulted in powder agglomeration. Consequently, the coating on the powders was not uniform. In addition, electroless Ni plating process such as pretreatment, pH and temperature also has a great influence on the coatings of the powder.

In this chapter, the effect of the electroless Ni plating parameters including the treating amount of the bath, electroless plating temperature and time on the coatings and Ni content of the powder were investigated. So far, there was no comprehensive describtion of the FeB compacts with Ni addition. Therefore, the effect of Ni content and sintering parameters on the behaviors and the mechanical properties of FeB-Ni compacts were investigated.

3.2 Experimental procedure

3.2.1 Powder preparation

As-received FeB powders with mean particle size of 45 μm were used as the raw materials to do the electroless plating. The powders were cleaned by acetone and immersed in hydrochloric acid (50 mL/L) for 60 s for pretreatment. The FeB powders were pretreated before electroless plating to produce a surface with catalytic activity. Then, the pretreated FeB powders were cleaned and put into a beaker placed in a thermostatic water bath for electroless plating. The acid plating bath, which contained less than 1% B, was purchased from Okuno Chemical Industries Co. Ltd. The plating bath consisted of main salt, reducing agent, complexing agent, stabilizing agent. Ni sulfate was the main salt, dimethylamine borane (DMAB) was the reducing agent. The reactions of electroless Ni–B plating from acid bath could be explained by main reactions of equations (1) -(3)[7]:

$$3Ni^{2+} + (CH_3)_2HN \cdot BH_3 + 3H_2O \rightarrow 3Ni + H_3BO_3 + (CH_3)_2H_2N^+ + 5H^+ \quad (1)$$

$$4Ni^{2+} + 2(CH_3)_2HN \cdot BH_3 + 3H_2O \rightarrow 2Ni + Ni_2B + H_3BO_3 + 2(CH_3)_2H_2N^+ + 6H^+ \quad (2)$$

$$HCl + (CH_3)_2HN \cdot BH_3 + 3H_2O \rightarrow H_3BO_3 + (CH_3)_2HN \cdot HCl + 2H_2 \uparrow \quad (3)$$

pH was within the range of 6.5 to 6.8. Temperature of electroless plating was within the range of 323 to 338 K. Keep constant of pH (6.5), temperature (323 K) and plating time (300 s) of the bath, the effect of the variation of the treating amount of the bath on the Ni coatings and content would be investigated. The treating amount was set 1, 3, 5 and 10 g/l according to the processing capability of the bath. The same method was used to determine the effect of plating temperature and time. During the electroless plating, the plating bath was continuously stirred to disperse and reduce agglomeration of powders. After the electroless plating, the powders were cleaned with de-ionized water and ethanol and dried in a vacuum oven at 323 K for 2 hours. Then the electroless Ni plated FeB powders were consolidated by spark sintering process.

3.2.2 Characterizations of the FeB-Ni powders and compacts

The FeB-Ni powders prepared by above process were consolidated by spark sintering process. Scan electron microscopy (SEM) was utilized to analyze the surface morphology of the original FeB powder before pretreatment, FeB powder after pretreatment, composite powder obtained after electroless plating, sintered compacts. The quantitative analysis was conducted on selected compacts by electron probe micro analysis (EPMA). The treating amount of the bath was characterized by the ratio of the mass of the FeB powder to the volume of the plating bath. The porosity of compacts was measured by the image analysis method[8]. The densities of the compacts were measured by Archimedes' method. The thermal analysis was carried out by differential scanning calorimetry (DSC, NETZSCH STA 449 C, Germany) at a constant heating and cooling rate of 0.083 K/s at 298–1000 K in an atmosphere of pure argon with a flow rate of 0.83 mL/s. X-ray diffraction (XRD) was employed for phase identification by using Cu Kα radiation (λ= 15.406 nm) at 40 kV and 0.1 A. The hardness of the compacts was measured by a Vickers hardness tester (load 1kg, 10s). The fracture toughness, K_{IC}, of the FeB–Ni compacts was determined by measuring the crack length

near the indent made by a Vickers indentation (MHT-1, Japan) load of 9.8 N and calculated by using the following equation (4)[9]. This equitation was used for calculating the fracture toughness of borides.

$$K_{IC}=0.064\sqrt{\frac{E}{H}}P/c^{3/2} \quad (4)$$

The Young's modulus, *E*, was 307 GPa according to the rule of mixtures calculation between the Young's modulus of FeB and that of Ni. The Young's modulus of FeB and Ni were approximately 343 GPa and 200 GPa, respectively[10]. H was the Vickers hardness, P was the indentation load, and c was the half of the indentation crack length near the indent. The compressive strength of the compacts was measured at room temperature by using a mechanical testing machine (Autograph DCS-R-5000, Shimadzu Corporation, Japan) with a constant crosshead speed of 0.83 μm/s.

3.3 Results and discussion

3.3.1 Effect of the plating parameters on the electroless plating

3.3.1.1 Effect of the pretreatment on the FeB powders

The surface morphologies of the initial FeB powders before and after pretreatment was shown in Fig. 3.1 (a) and (b). The surface of the initial FeB powders was smooth without obvious steps before pretreatment; the surface was flat and smooth. A mechanical surface resulting from the pelletizing process was observed. After pretreatment, a mass of steps and holes formed on the surface. The electroless plating on the powder was related to the catalytic activation of the plated surface. Catalytic activation referred to the number of active centers on the powder surface, which related to surface defects such as margin, steps, margin of adsorbate, and certain surface atoms or atom groups with space unsaturation. These positions with high energy was easy to deposit metal ions. Having more defects on the surface of FeB powder after pretreatment increased the deposition of Ni grains. So that the nucleated and grown plated Ni layer could distribute more evenly.

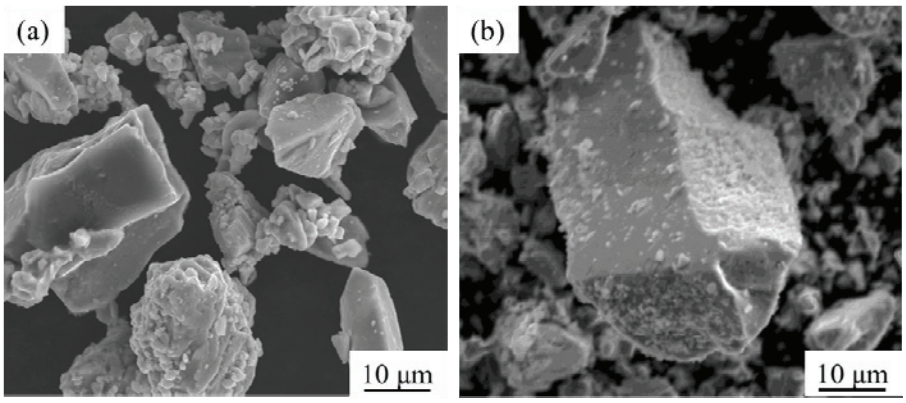

Figure 3.1 Surface morphologies of (a) initial FeB powders and (b) pretreated FeB powders.

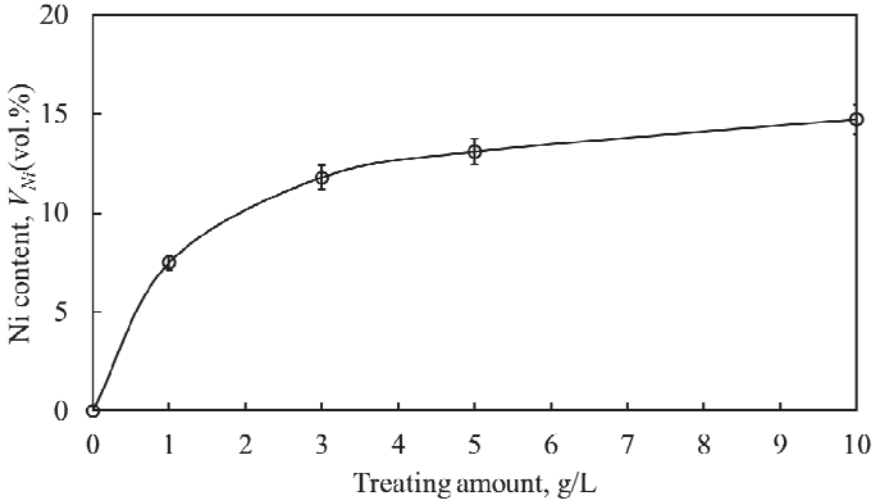

Figure 3.2 The relationship between the treating amount and the Ni content at the temperature of 323 K.

3.3.1.2 Effect of the treating amount of the bath on the Ni content and coatings

The treating amount of the bath was the ratio of the surface area of the electroless plating to the volume of the bath. The treating amount affected the Ni content and properties of the coating due to the large specific surface area of the FeB particles. The effect of treating amount of the bath on the Ni content was shown in Fig.3.2. The Ni content of the FeB powder increased rapidly when the treating amount was lower than 5 g/l. The more FeB powder with larger specific surface area resulted in the faster

reaction rate. It was considered that excessive reaction rate exceeded the processing capacity of the bath, even cause decomposition and failure of the bath. Consequently, the Ni content increased slightly when the treating amount of the bath was larger than 10 g/l.

In addition, the effect of the treating amount of the bath on the morphologies of electroless plated FeB at constant bath temperature of 323 K were also investigated as shown in Fig.3.3. As can be seen in this figure, electroless Ni plating in (a) and (b) was better than that of (c) and (d). Large treating amount accelerated the reaction rate, caused the reaction concentrated at the surface defect. As a result, the Ni layer was not distributed evenly before the end of the electroless plating. Moreover, it was difficult to disperse the FeB powder with too much FeB powder. The agglomeration of the FeB powder further caused the uneven of the Ni coatings, as shown in Fig.3.3(c) and (d). In addition, little treating amount of the bath also caused the low efficiency of the electroless plating. In this case, the treating amount of the bath set at 3g/l was suitable.

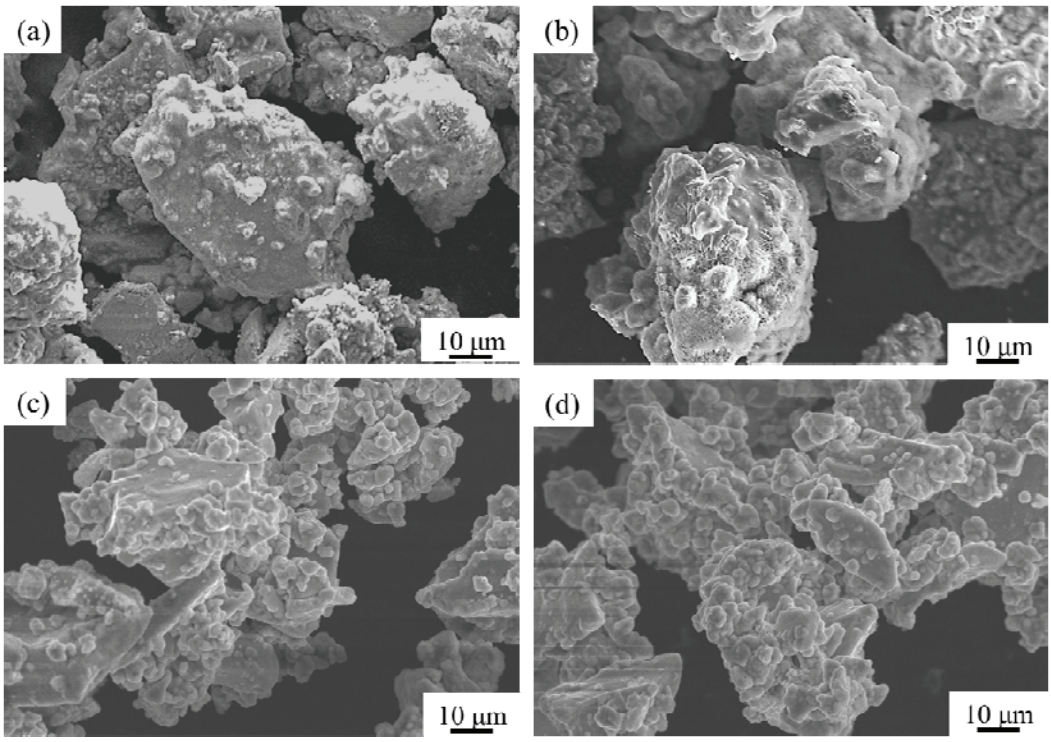

Figure 3.3 The morphologies of Ni coated FeB powder under the treating amount of (a) 1 g/L, (b) 3 g/L, (c) 5 g/L and (d) 10 g/L.

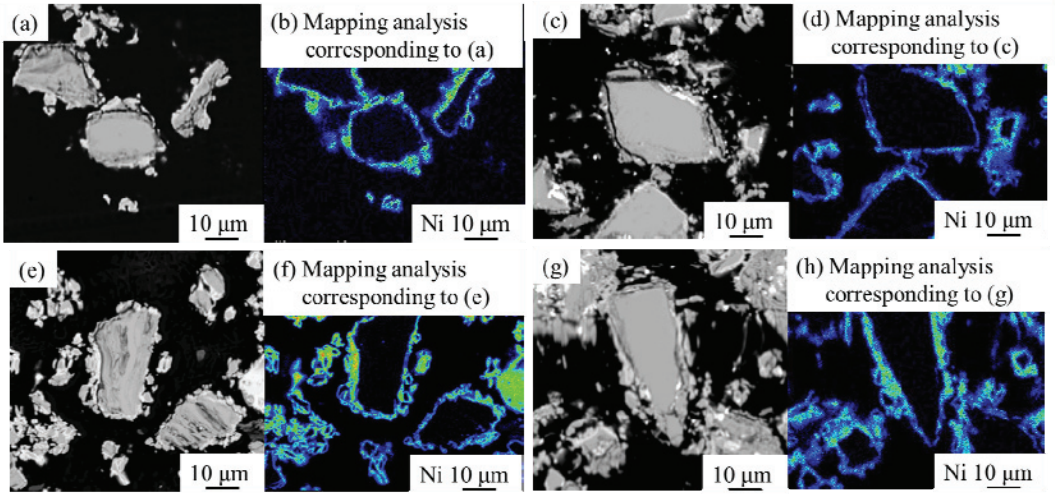

Figure 3.4 Compositional images of cross-section of Ni coated FeB powder under treating amount of (a) 1 g/L, (c) 3 g/L, (e) 5 g/L and (g) 10 g/L. (b), (d), (f) and (h) were the mapping images of Ni corresponding to (a), (c), (e) and (g), respectively.

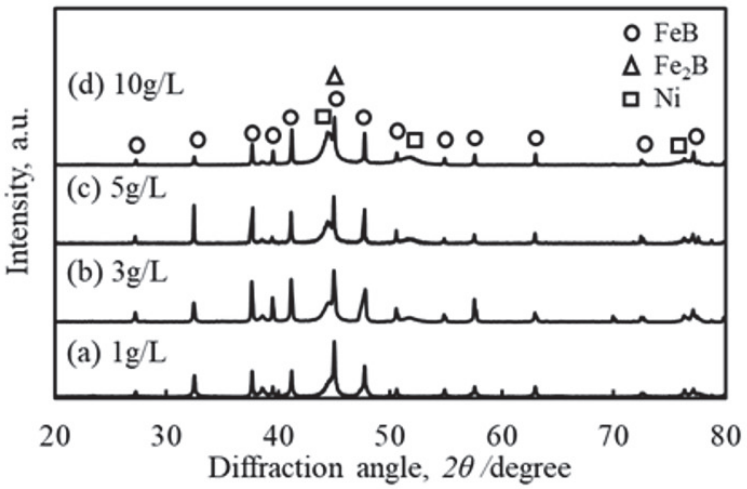

Figure 3.5 XRD patterns of Ni coated FeB powder under treating amount of (a) 1 g/L, (b) 3 g/L, (c) 5 g/L and (d) 10 g/L.

As shown in Fig. 3.4, Ni plating on the surface of the FeB powder was observed. The distribution of Ni layer in (a) and (b) was more even than that of (c) and (d). However, with increasing the treating amount of the bath, agglomeration of the powder

was observed. Small Ni particles may be the decomposition of the Ni layers[10]. The XRD patterns of electroless Ni plated FeB powder under different treating amount of the bath were shown in Fig. 3.5. It was found that the peak intensity of Ni increased with the increase of the treating amount of the bath which means the increasing of the Ni content. The broadening peak of Ni also indicated that the coated Ni coatings were amorphous structure.

3.3.1.3 Effect of the bath temperature on the Ni content and coatings

The temperature of the bath had a considerable influence on the chemical reaction rate. With the increase of the bath temperature, the activity of metal ions in the plating bath was enhanced, which was easier to adsorb on the surface of the FeB powder to participate in the chemical reaction. Thus, the deposition rate of the Ni increased with the increase of bath temperature. Consequently, the Ni content of FeB powder increased with the bath temperature as shown in Fig. 3.6. But the temperature of the bath could not be too high. it was noted that the high bath temperature would cause the decomposition of the bath.

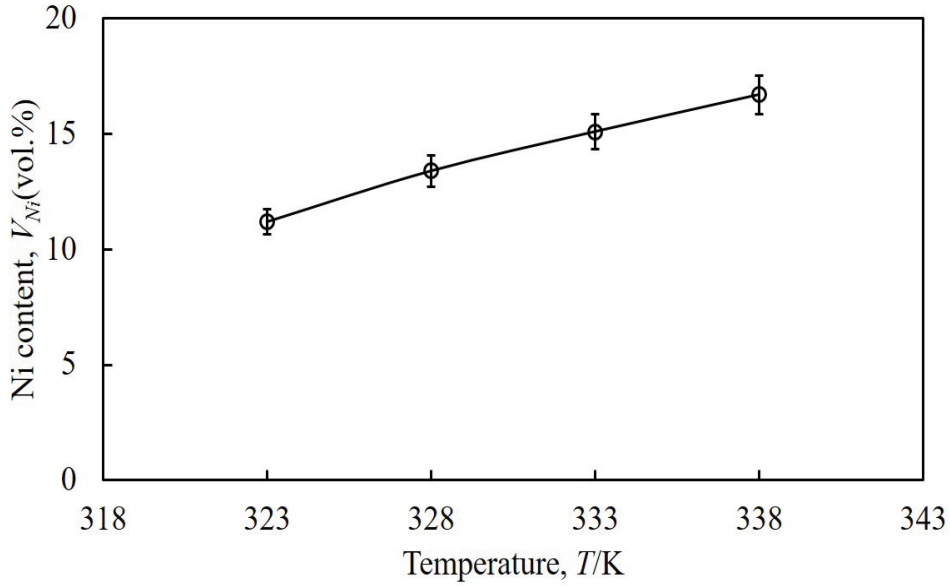

Figure 3.6 The relationship between the bath temperature and the Ni content at the constant treating amount of 3g/L.

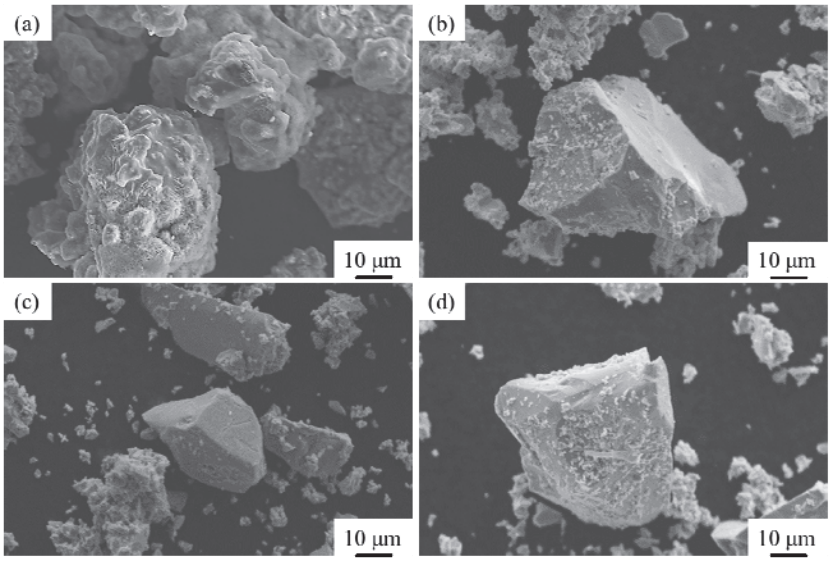

Figure 3.7 The morphologies of Ni coated FeB powders under different temperature. (a) 323 K, (b) 328 K, (c) 333 K and (d) 338 K.

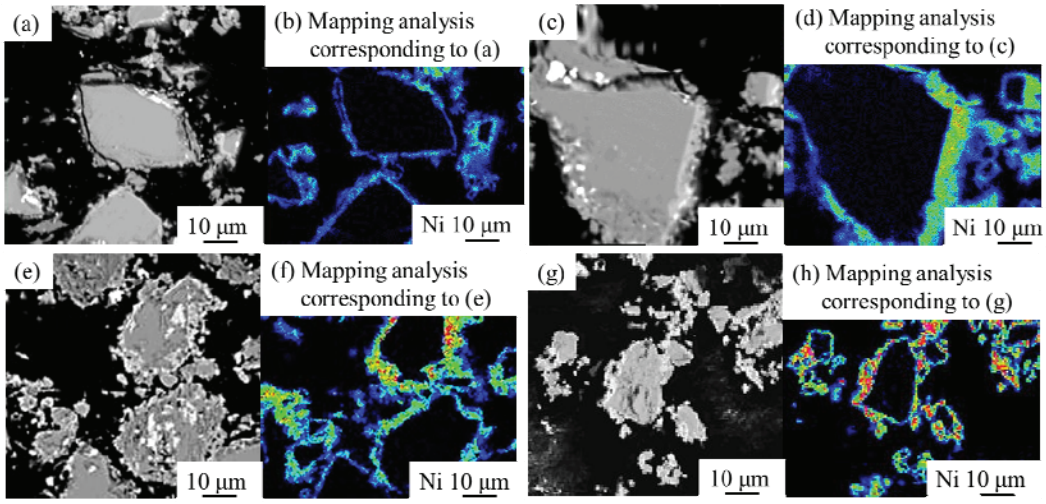

Figure 3.8 Compositional images of cross-section of Ni coated FeB powder under the bath temperature of (a) 323 K, (b) 328 K, (c) 333 K and (d) 338 K. (b), (d), (f) and (h) were the mapping analysis corresponding to (a), (c), (e) and (g), respectively.

The effect of the bath temperature on the morphologies of electroless plated FeB was shown in Fig.3.7. As can be seen in this figure, with the increase of bath temperature, the distribution of the Ni coating was not good, accompanied by powder agglomeration. This may be related to the fast-chemical reaction and the gas produced

in the chemical reaction. The increase of temperature would accelerate the rate of gas release in plating bath which would hinder the deposition of the metal ion. It could be further understanding from the mapping analysis shown in Fig. 3.8. Too fast chemical reaction also resulted in the loose and flaking of coatings and irregular growth of coating particles in Fig.3.8 (b), (c) and (d). The flaking of coatings formed the available nucleation sites that caused heterogeneous nucleation[10]. Moreover, it was easily lead to decomposition of the bath. The Ni coated FeB was further investigated by the XRD, as shown in Fig. 3.9. The broadening of Ni was detected without new phase existing. It means that variation of temperature had no effect on the composition of the coating.

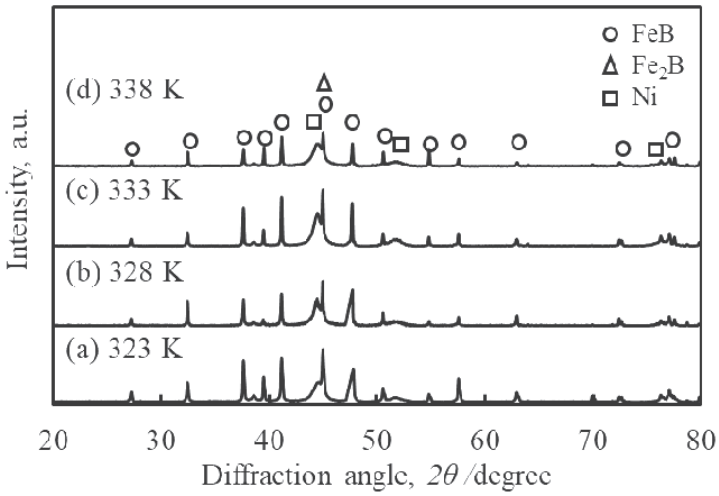

Figure 3.9 XRD patterns of Ni coated FeB powder under different temperature of the bath. (a) 323 K, (b) 328 K, (c) 333 K and (d) 338 K.

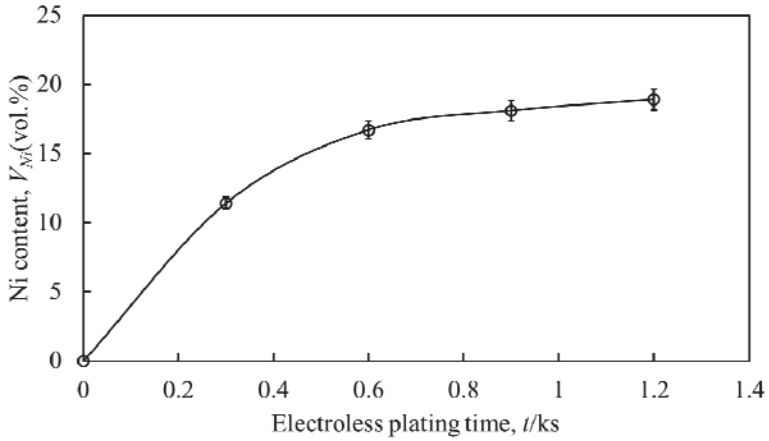

Figure 3.10 The relationship between the electroless plating time and the Ni content, treating amount 3 g/L at the bath temperature of 323 K.

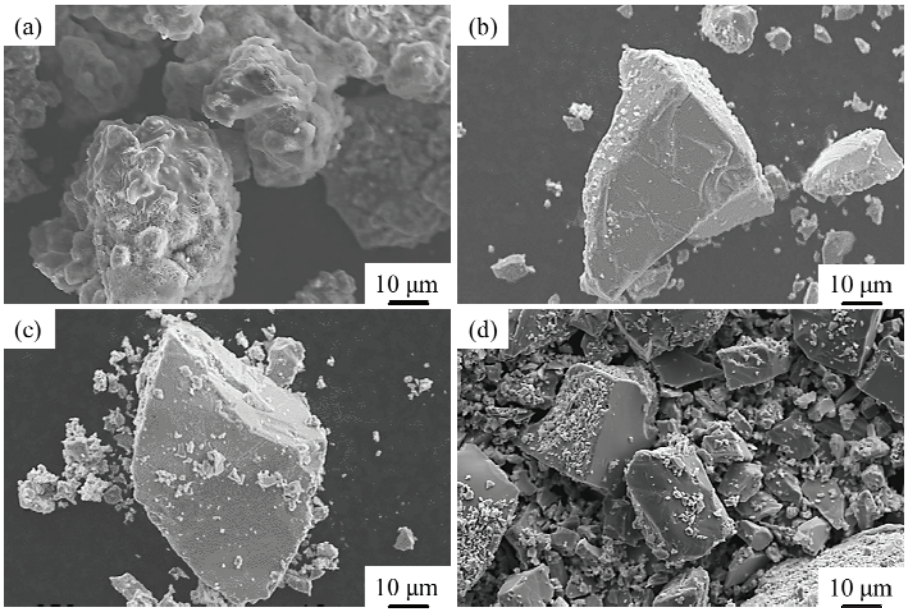

Figure 3.11 The morphologies of Ni coated FeB powder after electroless plating for (a) 0.3 ks, (b) 0.6 ks, (c) 0.9 ks and (d) 1.2 ks.

3.3.1.4 Effect of the electroless plating time on the Ni content and coatings

The FeB powder with different Ni content could be obtained at different electroless plating time. Figure 3.10 showed the relation between the electroless plating time and the Ni content of the FeB powder. It can be seen from the figure that the chemical reaction rate was very fast in the initial 0.3 ks. This may be because the high surface activity and more nucleation sites of the FeB powder adsorbed a large number of Ni ions on its surface in the initial state of electroless plating. The adsorbed Ni ions involved in the chemical reaction and formed the Ni coating. With the increase of plating time to 0.6 ks, the increase of Ni content was slightly decrease. The Ni ions around the powder were consumed in large quantities due to the fast reaction rate. It was difficult to be supplemented effectively in a short period of time. The decrease of the Ni ion in the reaction resulted in the decline of the reaction rate. After 0.9 ks, the Ni content increased gently. In this case, the reducing agent and Ni ions were consumed too much so that the reaction tended to stop.

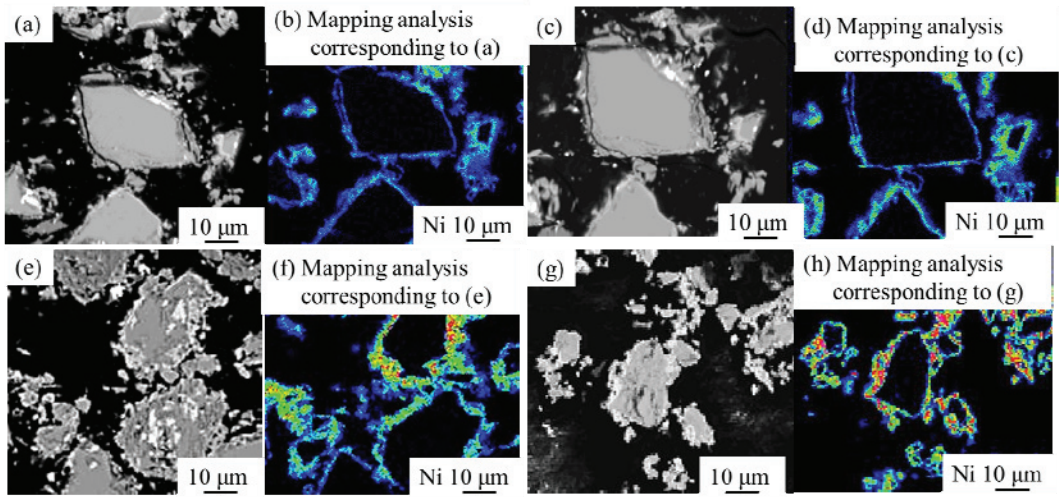

Figure 3.12 Compositional images of cross-section of Ni coated FeB powder under the bath temperature of (a) 0.3 ks, (b) 0.6 ks, (c) 0.9 ks and (d) 1.2 ks. (b), (d), (f) and (h) were the mapping images of Ni corresponding to (a), (c), (e) and (g), respectively.

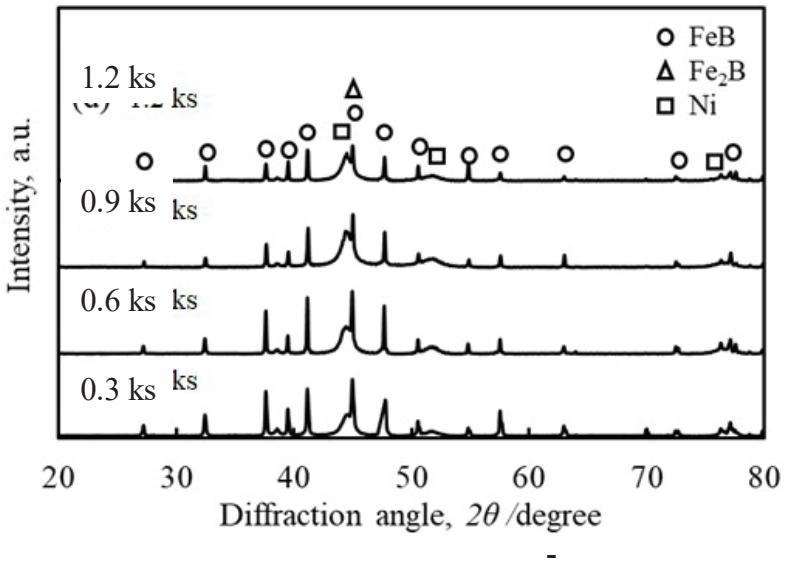

Figure 3.13 XRD patterns of Ni coated FeB powder after electroless plating for (a) 0.3 ks, (b) 0.6 ks, (c) 0.9 ks and (d) 1.2 ks.

The effect of the electroless plating time on the morphologies of electroless Ni plated FeB were shown in Fig. 3.11. As can be seen in this figure, with the increase of electroless plating time, there was no obvious phenomenon of powder agglomeration.

This may be related to the uniform distribution of the Ni coating suppressed the agglomeration of the powder. With the increase of the plating time, the Ni content of the powder increased gradually, which indicated that the thickness of the coating also increased. Electroless plating for too long time, large particles were observed in Fig. 3.11(d). It would make the coating loose and poor quality as can be seen in Fig.3.12(d).

Figure 3.13 showed the XRD patterns of Ni coated FeB powder for different electroless plating time. The broadening peak of Ni was detected under different plating time. The intensity of FeB phase decreased with the increase of the plating time which associated with the increased thickness of Ni coating.

Table 3.1 Composition of the plating bath for Ni coating on FeB powders.

Chemical composition	Concentration
Nickel sulfate, g/l	30
DMAB($(CH_3)_2HN{\bullet}BH_3$), g/l	4
complexing agent, g/l	40
Reducing agent, g/l	40

Table 3.2 Operating conditions for Ni coating on FeB powders

Operating conditions	Temperature, K	Treating amount, g/L	Stirring speed, rpm	pH
	323	3	100	6.5

Overall, the composition and operating conditions of the plating bath for Ni coating on FeB powders were concluded as shown in the table 3.1 and 3.2. The processing and properties of FeB-Ni hard materials were highly dependent on the basic nature of the hard phase and soft metal binder phases[11]. FeB as the hard phase was hard and brittle with low sinterability[12]. Ni as the binder phase was added to improve the sinterability of the FeB. Moreover, the content of Ni affected the hardness and fractur toughness of FeB-Ni hard materials[13]. Therefore, the plating time was set 180, 300, 600 and 900 s to obtain FeB containing 5vol.%, 10vol.%, 25vol.% and 30vol.% Ni (hereafter called FeB-5Ni, FeB-10Ni, FeB-25Ni and FeB-30Ni). The effect of the Ni content of the FeB

powder on the sintering behaviors and mechanical properties of the FeB were investigated.

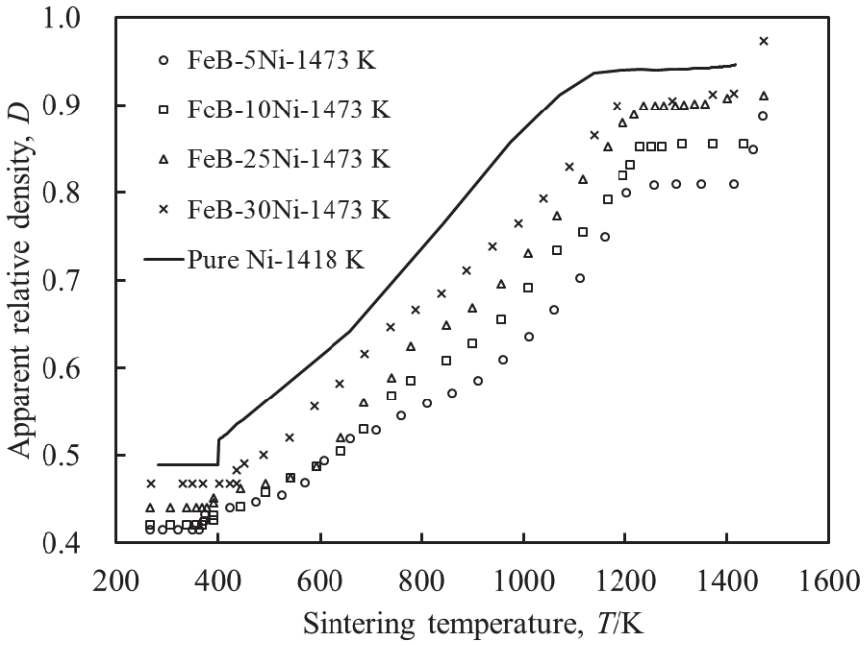

Figure 3.14 Relation between sintering temperature and apparent relative density of FeB-5Ni, FeB-10Ni, FeB-25Ni, FeB-30Ni and pure Ni compacts.

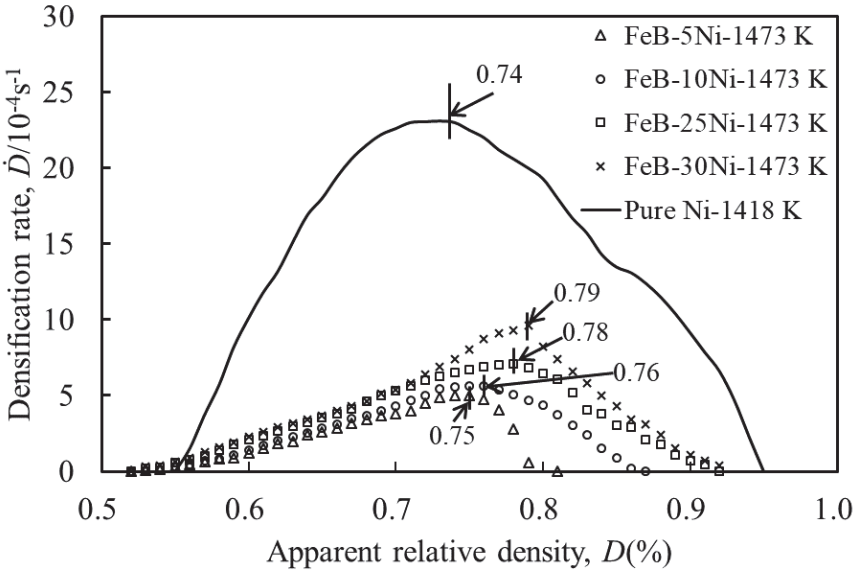

Figure 3.15 Relation between densification rate and apparent relative density of the FeB-5Ni, FeB-10Ni, FeB-25Ni, FeB-30Ni, and pure Ni.

3.3.2 Effect of Ni content on the microstructures and properties of the compacts.

3.3.2.1 Sintering behaviors of the FeB-Ni compacts

Figure 3.14 showed the relation between sintering temperature and apparent relative density of FeB-5Ni, FeB-10Ni, FeB-25Ni, FeB-30Ni and pure Ni compacts. The sintering curves of FeB-Ni compacts with different Ni contents were shown in this figure. Sintering curves of FeB-Ni compacts with different Ni contents showed the similar sintering behaviors regardless of Ni contents, although their apparent relative densities were increased with the increment of Ni contents. The apparent relative densities of FeB-Ni compacts with different Ni contents were increased monotonously in the temperature range below 1200 K. And then the apparent relative density became almost constant above this temperature. After that the apparent relative density increased rapidly due to the appearance of liquid phase. Moreover, the slope of sintering curves below about 1200 K for FeB-Ni compacts was increased with the increase of Ni content. The slope in the sintering curves meant the consolidation rate in the temperature range below 1200 K. On the other hand, the deformation of FeB hard phases could not be expected below 1200 K because of the slightly increment of the apparent relative density according to the sintering curve of FeB compact[14]. It was found that the increment of the apparent relative density of FeB-Ni compacts was mainly due to the addition of Ni. As shown in Fig.3.14, the sintering curve of FeB-5Ni compact with low apparent relative density compared with FeB with high volume fraction of Ni. The sintering curve of the pure Ni compact showed good sinterability due to the high slop and apparent relative density.

In order to investigate the mechanism of densification in spark sintering process, the densification rate of FeB-Ni with different Ni contents and pure Ni compacts were obtained experimentally as shown in Fig.3.15. The densification rate, $\dot{D}$, was obtained by dividing the apparent relative density increment, dD, by time increment, dt.

$$\dot{D} = dD / dt \tag{5}$$

where D and t were apparent relative density and the corresponding sintering time, respectively. It was reported that plastic deformation of the compacts occurred before reaching maximum point of the $\dot{D}$. After that power law creep deformation of compacts

occurred using pure copper, pure Ti and Al_2O_3 added copper powders[15-19]. The peaks of $\dot{D}$ of FeB-5Ni, FeB-10Ni, FeB-25Ni and FeB-30Ni compacts occurred at 0.75, 0.76, 0.79 and 0.78, respectively which were similarity. On the basis of the previous results, it was considered that the plastic deformation of Ni layer in FeB-Ni compacts occurred before reaching maximum point of the $\dot{D}$. After that power law creep deformation of Ni layer occurred in compacts. Pure Ni compact showed high densification rate, and its peak value was 0.74 at D which was close to FeB-5~30Ni compacts. In contrast, the value in $\dot{D}$ peak of FeB-0Ni compact was much lower than those of FeB-Ni compacts. It was proved that the FeB phase showed little deformation in this temperature range below 1200 K[14]. Therefore, the plastic deformation of Ni layer caused by Joule's heat generation among particles played the dominant role in increasing the apparent relative density for FeB-Ni compacts. It meant that increment of apparent relative density for FeB-10Ni caused by the electroless plating 10vol.% Ni on FeB powder surfaces. Moreover, the apparent relative density could be further improved by more Ni addition.

3.3.2.2 Microstructures and mechanical properties of the FeB-Ni compacts.

Figure 3.16 showed compositional images of the (a) FeB-5Ni, (b) FeB-10Ni, (c) FeB-15Ni and (d) FeB-30Ni compacts. It was noted that uniform Ni layers formed on FeB powder surfaces were observed after consolidation. The FeB-Ni compacts with different Ni contents achieved less porosity because the Ni binder phase filled the existing voids between FeB particles. Moreover, the Ni layer around the FeB particles reduced the direct contact of the hard phases during sintering which also decreased the porosity. The average porosities in FeB-5Ni, FeB-10Ni, FeB-25Ni and FeB-30Ni compacts sintered at 1473 K were 0.5%, 0.82%, 0.49% and 0.36%, respectively. As reference, the porosity of FeB compact was 28.1%. It was considered that the porosity was decreased with increment of the Ni contents. However, much more Ni addition may result the enrichment of the Ni as shown in Fig.3.16(c) and (d). Figure 3.17 showed XRD patterns of the (a) FeB-5Ni, (b) FeB-10Ni, (c) FeB-25Ni and (d) FeB-30Ni compacts. XRD patterns of FeB-Ni compacts with different Ni contents revealed the presence of FeB, Fe_2B and Ni peaks. There were main constituent FeB phase of 92%,

82%, 69% and 63% in FeB, 5, 10, 25 and 30 Ni compacts. As shown in contrast to Fig 3.5, 3.9 and 3.13, Ni phases with crystalline structure were detected in the XRD patterns indicating that the structure of the Ni layers was transformed from amorphous to crystalline. In addition, the weaker intensity of FeB peaks in Ni coated FeB powders were related to the covering of Ni on the surface of FeB.

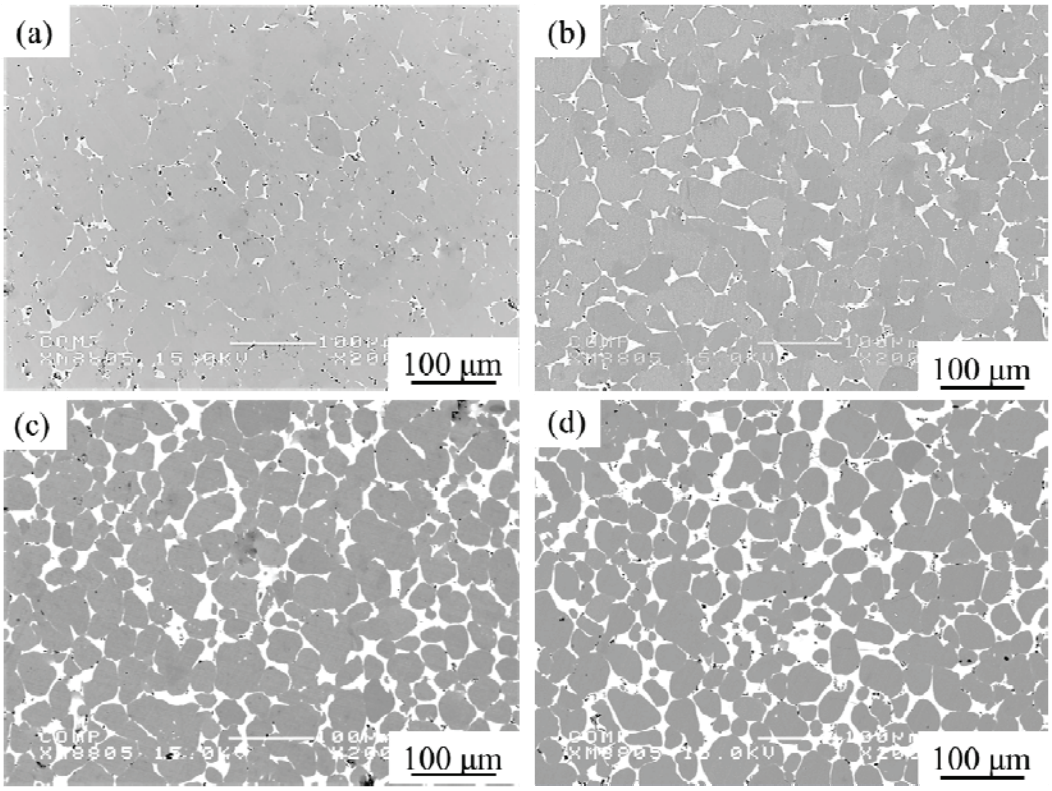

Figure 3.16 Compositional images of the (a) FeB-5Ni, (b) FeB-10Ni, (c) FeB-15Ni and (d) FeB-30Ni compacts sintered at 1473 K.

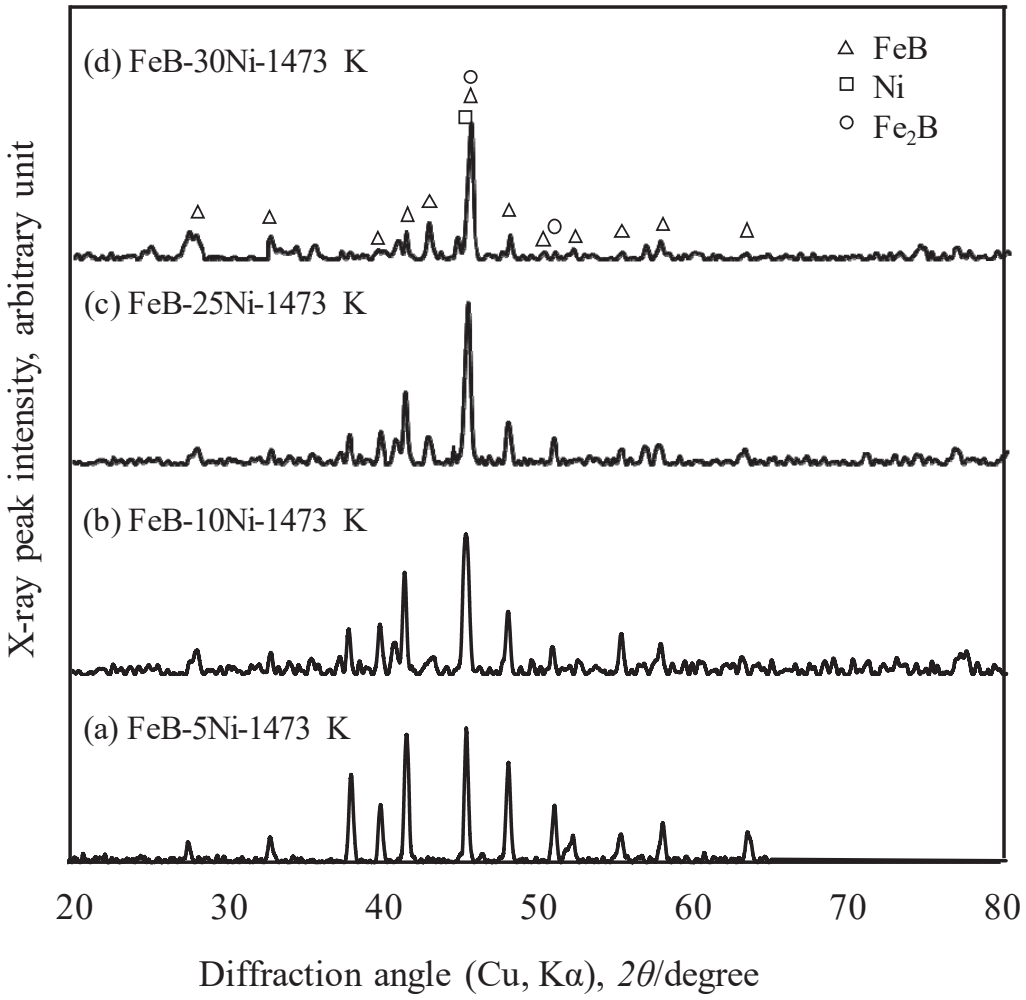

Figure 3.17 XRD patterns of the (a) FeB-5Ni, (b) FeB-10Ni, (c) FeB-25Ni and (d) FeB-30Ni compacts sintered at 1473 K.

Figure 3.18 showed the relation between Vickers hardness and porosity of the FeB-5Ni, FeB-10Ni, FeB-25Ni, FeB-30Ni compacts. The Vickers hardness of FeB-10Ni compact was higher than that of FeB-5Ni, FeB-25Ni and FeB-30Ni compacts sintered at the same temperature. It was considered that the increment of the soft Ni contents resulted in the decreased of the hardness. In addition, the Vickers hardness of FeB-30Ni compact was close to that of FeB-25Ni compact due to same level porosity and the enrichment of the Ni binder phase. Moreover, the Vickers hardness of FeB-10Ni compact was higher than that of FeB-5Ni compact due to the low porosity, although the Ni with low hardness was added.

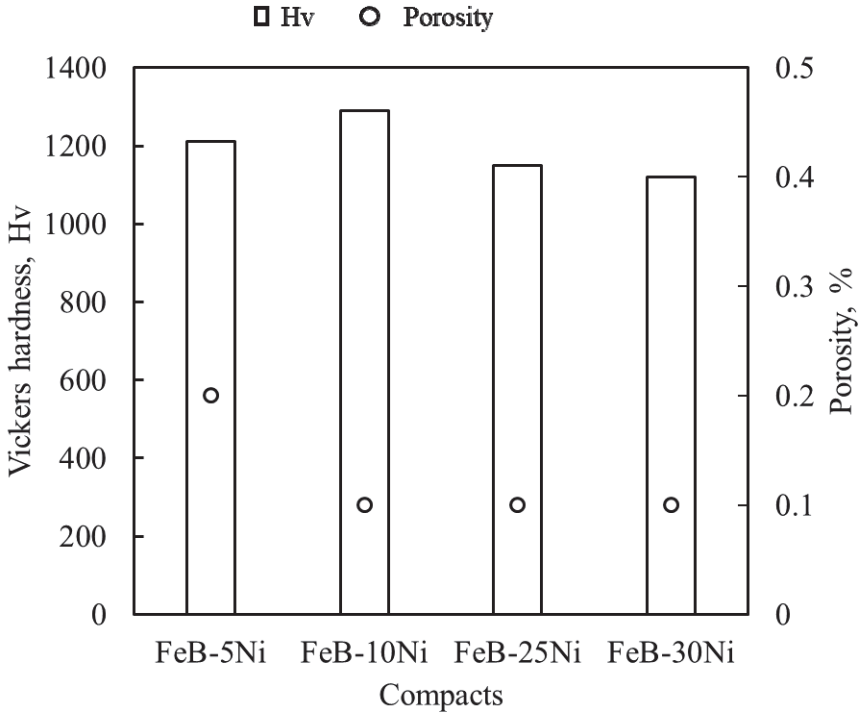

Figure 3.18 Relation between Vickers hardness and porosity of the FeB-5Ni, FeB-10Ni, FeB-25Ni, FeB-30Ni compacts sintered at 1473 K.

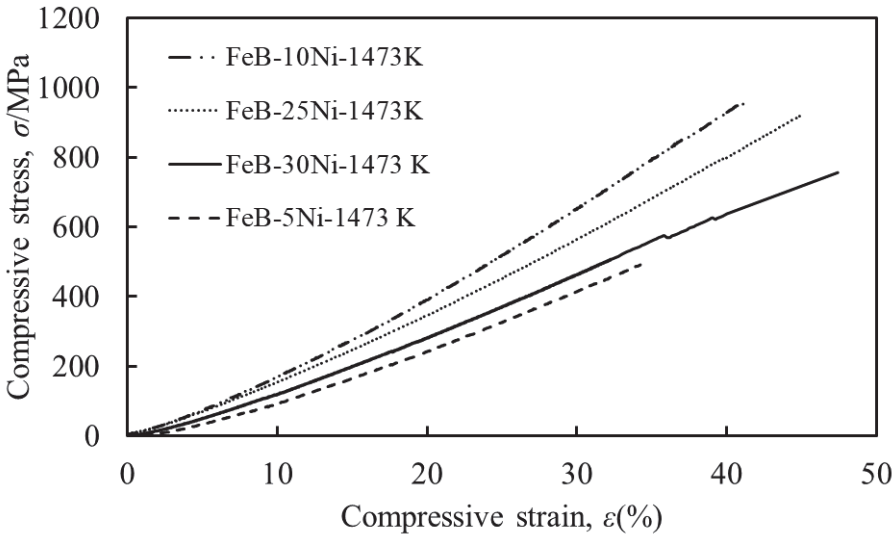

Figure 3.19 Compressive stress-strain curves of the FeB-5Ni, FeB-10Ni, FeB-25Ni and FeB-30Ni compacts sintered at 1473 K.

Figure 3.19 showed compressive stress-strain curves of the FeB-5Ni, FeB-10Ni, FeB-25Ni and FeB-30Ni compacts. FeB-Ni compacts showed the high compressive strain more than 40%, although that of approximately 35% was shown in the FeB-5Ni compact. The compressive stress of FeB-Ni compacts increased with the increment of the Ni contents until the Ni content up to 10%. Then, the compressive stress of FeB-Ni compacts decreased with the further increment of the Ni contents. It was considered that the Ni phase surrounding FeB hard phase improved the interfacial strength between FeB phases. However, excessive addition of Ni could also result in enrichment of Ni phase and reduced the compressive strength. The typical fracture surfaces of FeB-5Ni and FeB-10Ni compacts were shown in Fig.3.20. Smooth surface with cleavage steps were observed in these two fracture surfaces. The fracture mode of FeB-5Ni and FeB-10Ni was the mixture of intragranular fracture and intergranular fracture. Grain boundaries between FeB phases with many pores and fragmentation of the fine grains between the FeB phases were observed in Fig.3.20 (a). It was considered that no continuous Ni layers were formed around the FeB particles due to the insufficient Ni addition. While, no obviously pores were observed between the FeB particles as shown in Fig. 3.20(b). It was considered that continuous Ni layers were formed around the FeB particles and avoided the directly contact of the FeB hard phase which improved the interfacial strength.

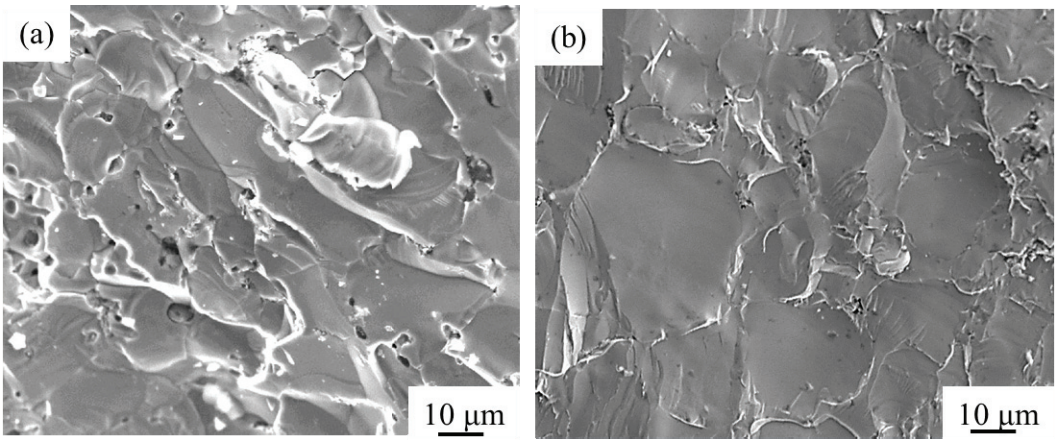

Figure 3.20 SEM images of fracture surfaces of the (a) FeB-5Ni and the (b) FeB-10Ni compact sintered at 1474 K.

3.3.2.3 Candidate ability of FeB-Ni hard materials

The spark sintering process was utilized to consolidate FeB-Ni materials under the same sintering temperature. The sintering ability, microstructures and mechanical properties of FeB compacts with different Ni content were investigated. It was concluded that FeB-10Ni hard materials had the possibility to substitute the WC-Co hard materials according to above mentioned results. However, the majority of the work by far dealt with the improvement of the sinterability of FeB, homogeneous distribution of the Ni binder and the influence of the Ni content. There were few research on the influence of the sintering process on the microstructure and mechanical properties of the FeB-Ni compacts. Spark Plasma Sintering (SPS) offered many accessible parameters for processing bulk compacts (temperature, holding times, et al.). These process parameters could be varied in order to get different microstructure since the microstructure was responsible for controlling the mechanical properties. Therefore, the processing parameters were investigated in optimizing microstructure and mechanical properties of compacts.

3.3.3 Effect of the process parameters on the microstructures and properties of the FeB-10Ni compacts

3.3.3.1 Effect of the sintering temperature on the microstructures and properties of the FeB-10Ni compacts

In the SPS process, temperature was the main governing parameter for controlling microstructural features. Higher temperature promoted the densification of the compacts. Figure 3.21 showed the influence of sintering temperature on the relative density of FeB-Ni compacts. The heating rate, holding time and pressure were for 50 K/min, 1.8 ks and 50 MPa, respectively. FeB-Ni compacts with high relative density could be obtained above 1473 K. As the temperature increased, the diffusion coefficient of the atom increased, and the atomic diffusion process became more active. The Ni binder phase began to self-diffusion on the surface. With further increased in temperature, the diffusion between FeB hard phase and binder phase occurred and the relative density of

the compacts increased. In addition, the plastic fluidity of the material increased with the increase of temperature. The relative density would be further improved.

Figure 3.22 showed the compositional images of FeB-10Ni compacts sintered at the temperature range of 1273 to 1523 K. It could be seen that the distribution of the Ni binder phase was relatively homogeneous. No obviously grain growth of the FeB was observed in Fig. 3.22 (a), (b) and (c). However, many pores were observed in this compact, which resulted in low relative density. As the sintering temperature increased to 1443 K, the grain growth of the FeB was still not obvious and the porosity decreased as shown in Fig. 3.22 (d). When the sintering temperature exceeded the eutectic temperature of 1443 K, the fully dense FeB-10Ni compact was obtained without obviously pores as shown in Fig. 3.22(e) and (f). With the increase of temperature, the fluidity of the Ni binder phase increased. The improvement of the fluidity of the Ni binder phase was easily to fill the pores between FeB phases, which made the distribution of the binder phase more uniform and increase the relative density.

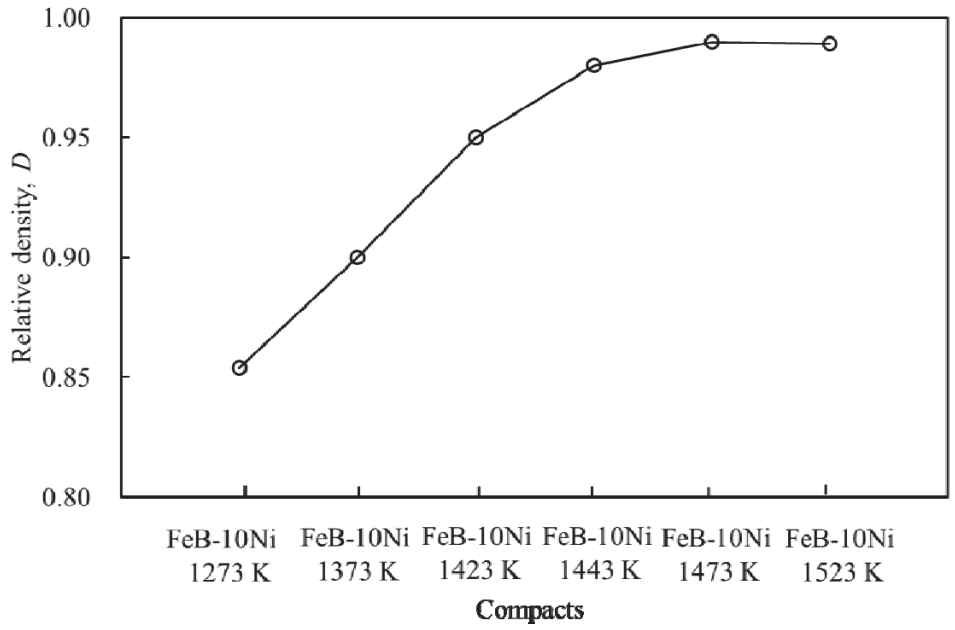

Figure 3.21 Relative densities of FeB-10Ni compacts sintered at the temperature range of 1273 to 1523 K.

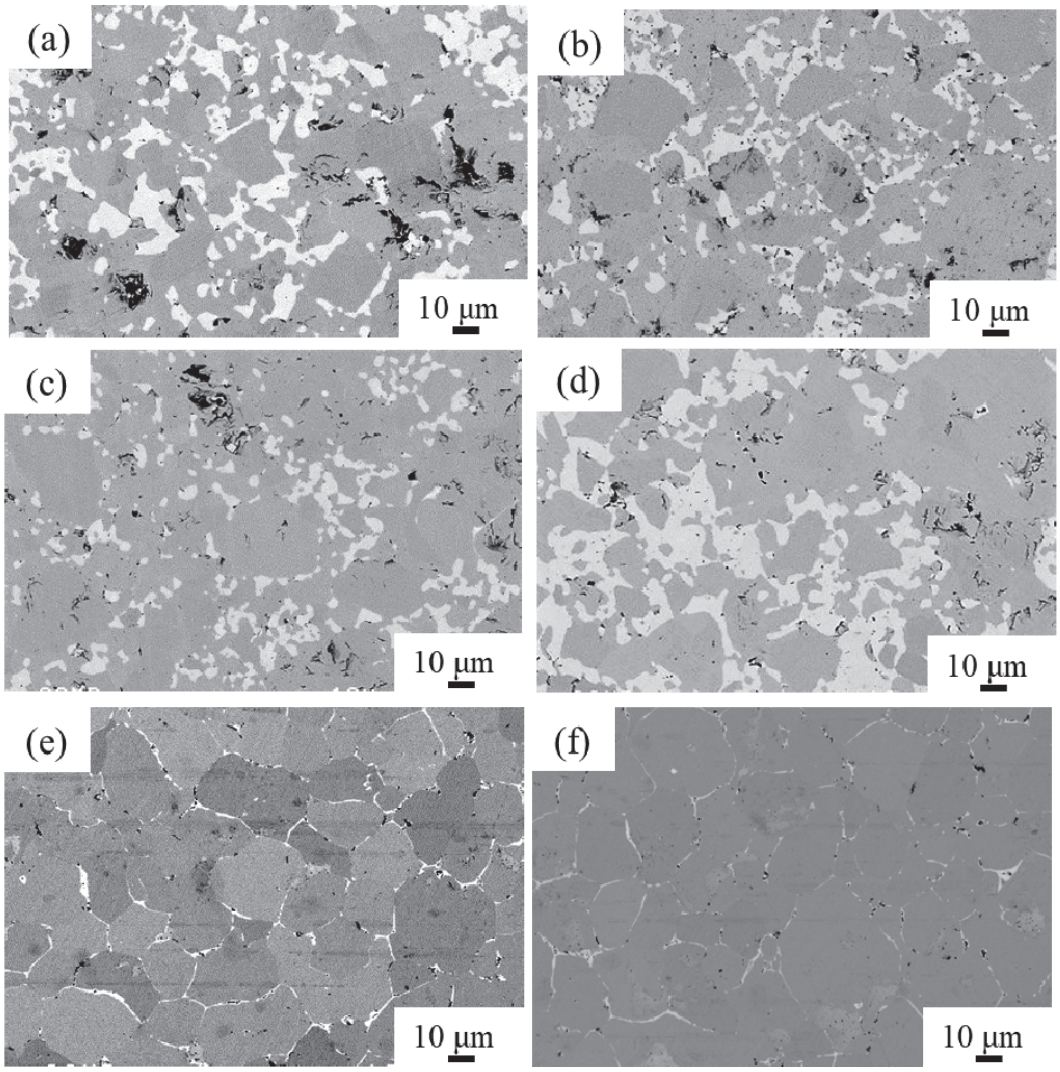

Figure 3.22 Compositional images of FeB-10Ni compacts sintered at (a) 1273 K, (b) 1373 K, (c) 1423 K, (d) 1443 K, (e) 1473 K and (f) 1523 K.

However, excessive high sintering temperature could cause considerable loss of the Ni binder due to the higher vapor pressure of Ni. The loss of Ni in practice had been reported to be 10% or more[20-22]. In addition, high sintering temperature promoted the formation of liquid phase. excessive liquid phase easily resulted in the liquid leakage. No enough binder phases to fill the pores resulting in the decrease of the relative density. In addition, high sintering temperature would result in the grain growth significantly.

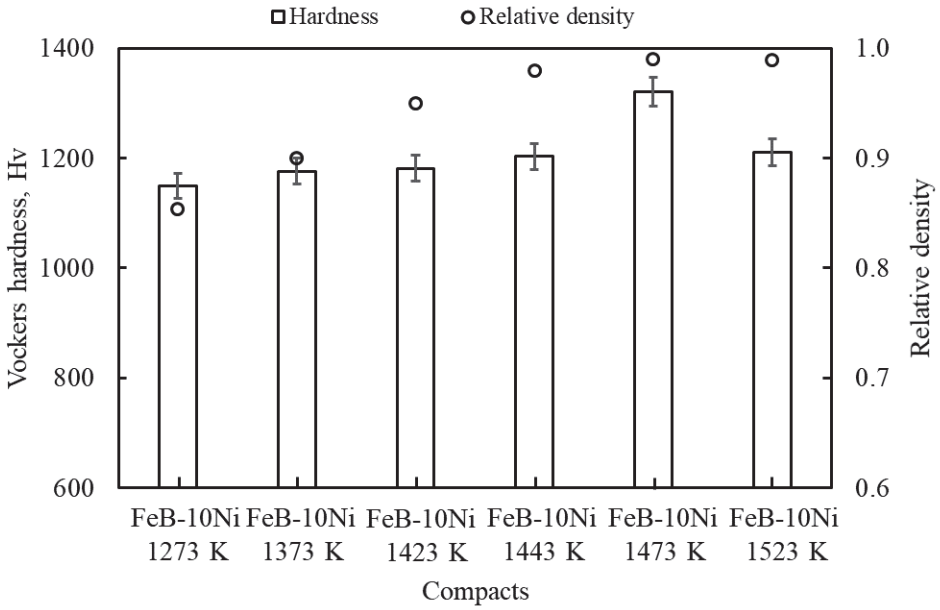

Figure 3.23 Relation between the Vickers hardness and relative density of the FeB-10Ni compacts sintered at the range of 1273 to 1523 K.

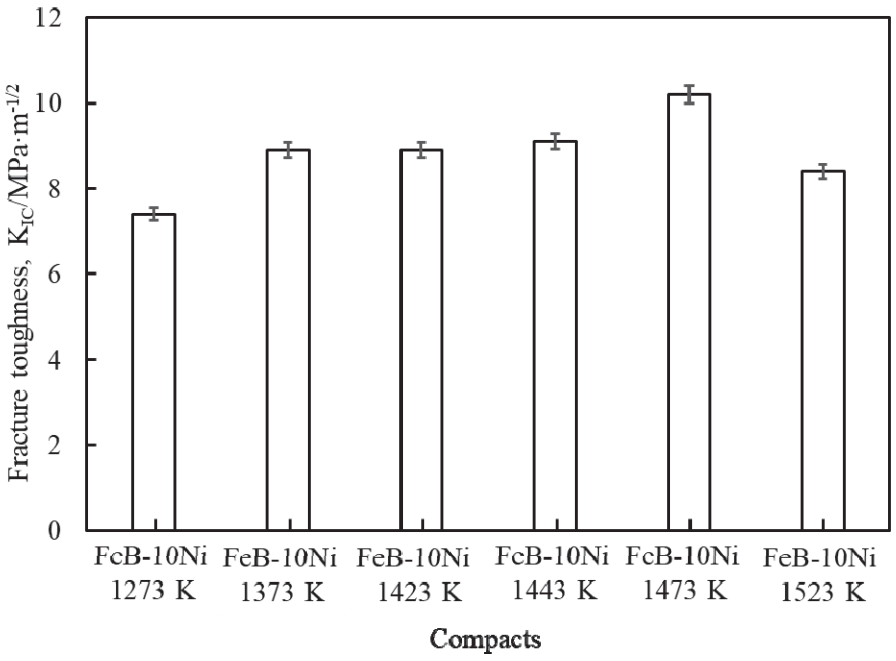

Figure 3.24 Fracture toughness of FeB-10Ni compacts sintered at the temperature range of 1273 to 1523 K.

Figure 3.23 showed the Vickers hardness of the FeB-10Ni compacts sintered at different temperature. As shown in this figure, the hardness of the FeB-10Ni compacts increased with the increase of the sintering temperature at the temperature range of 1273 to 1473 K. It was mainly because the porosity of the compacts decreased with the increment of the sintering temperature. In addition, the grain size and homogeneity of the Ni distribution of the FeB-Ni compacts also affected the hardness of the material. Although the grain size of FeB-10Ni compacts sintered at 1473 K was larger than the compacts sintered at lower temperature, the hardness of the compact improved by the homogeneity distribution of the Ni binder phase and the lower porosity. The decrease of the hardness of FeB-10Ni compact sintered at 1523 K was mainly because of the large grain size.

The fracture toughness of materials was a critical state which characterized the resistance of the compact against crack propagation. Figure 3.24 showed the fracture toughness of the FeB-10Ni compacts sintered at temperature range of 1273 to 1523 K. As can be seen in this figure, the fracture toughness of the FeB-10Ni compacts showed no obvious change at the range of 1373 to 1443K. The fracture toughness of compact sintered at 1473 K was greatly improved. The impurities in the grain boundary, the defects such as pores and the coarse grain size would weaken the fracture toughness of the compacts. As mentioned above, the porosity of the FeB-10Ni compacts sintered at 1473 K was lower than the compacts sintered at lower temperature. Porosity had a greater impact on the fracture toughness due to the pores would be the source of the crack propagation. Moreover, the more even distribution of the Ni binder phase also improved the fracture toughness. The large grain size also caused the lower fracture toughness of FeB-10Ni compact sintered at 1523 K.

Based on the above analysis of the effect of sintering temperature on the material structure and properties, it could be concluded that the grain size was increases with the increasing of the sintering temperature, while the porosity and other defects gradually decreased. Hardness and fracture toughness were low under solid phase sintering. At low liquid phase sintering temperature, a compact with high comprehensive mechanical

properties could be prepared. Therefore, the experiment was selected 1473 K as the best sintering temperature.

3.3.3.2 Effect of the holding time on the microstructures and properties of the compacts

Proper holding time could promote the diffusion of Ni binder phase, homogenize the microstructure and eliminate the internal stress, et al. However, the observations of the sintering curves in Fig.3.14 during heating showed that a considerable portion of the whole densification occurred before reaching the target temperature. This implied that the holding time didn't have a large influence on the relative density of the compacts, which verified by the conclusion obtained from the experimental results shown in Fig. 3.25. The figure was for the FeB-10Ni compact heated to 1473 K and held for times ranging from 0 to 1.8 ks. The variation of the relative density under different holding time was negligible.

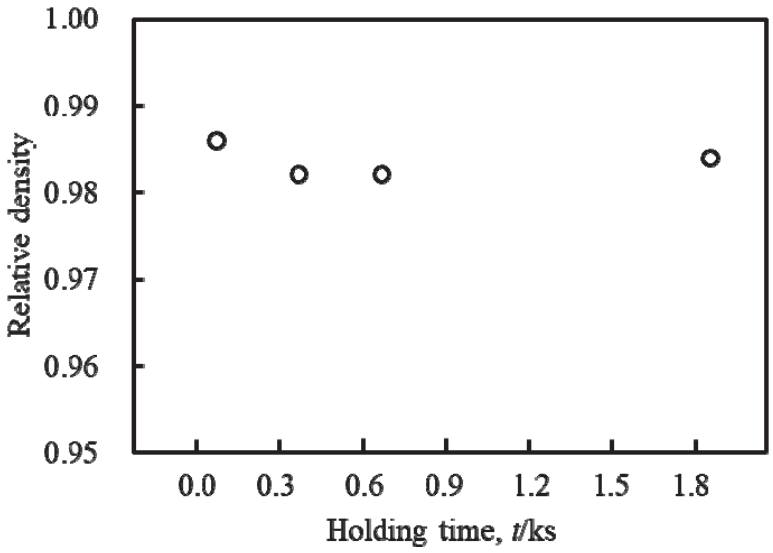

Figure 3.25 Relative densities of FeB-10Ni compacts sintered at 1473 K holding at the range of 0 to 1.8 ks.

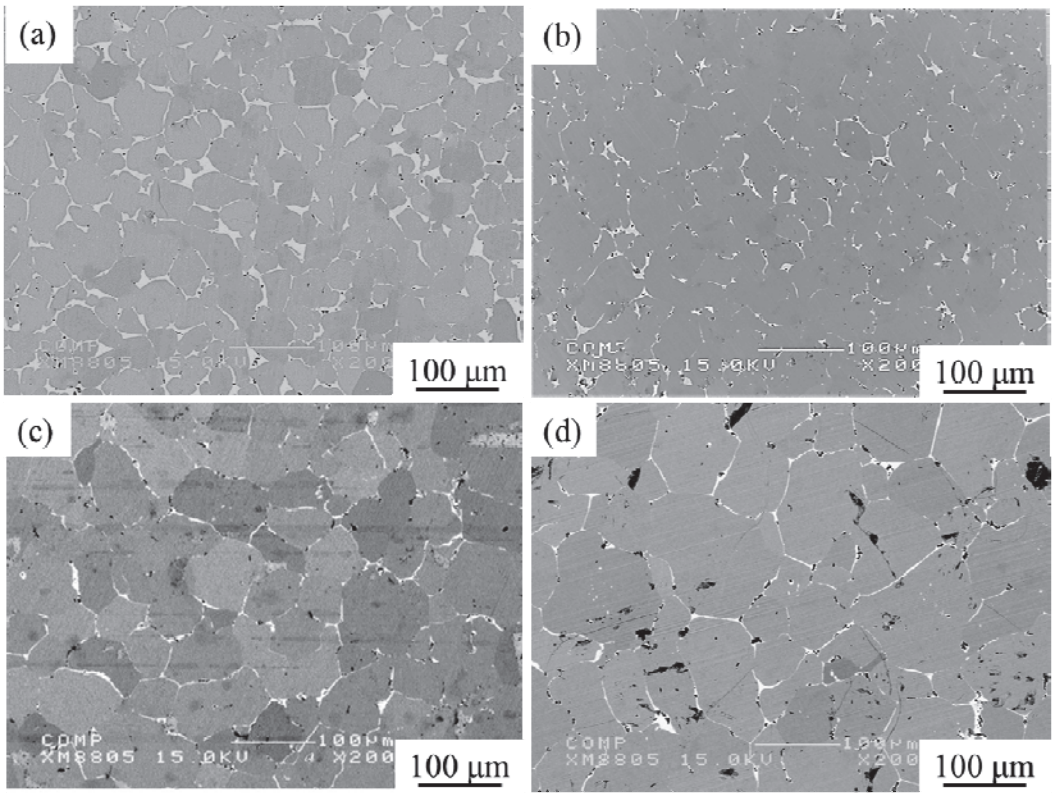

Figure 3.26 Compositional images of FeB-10Ni compacts sintered at 1473 K holding for (a) 0 s, (b) 0.3 ks, (c) 0.6 ks and (d) 1.8 ks.

Figure 3.26 showed the compositional images of FeB-10Ni compacts sintered at 1473 K holding at the range of 0 to 1.8 ks. Gray and white parts indicated the FeB and Ni phases, whereas the residual porosity was referred to black parts. FeB-10Ni compact without no holding time was fully dense with homogeneous distribution of Ni, as shown in Fig 3.26(a). There were almost no obvious pores as can be seen in Fig 3.26(b). The compact exhibited homogeneous and dense microstructure without rich zone of Ni. Fig 3.26(c) and (d) showed that the compactness of FeB-10Ni compacts was poor, and there existed many pores. Ni content of the compacts decreased with the increase of the holding time. FeB-10Ni compact sintered at 1473 K was liquid phase sintering. Long holding time would cause leakage of the liquid phase. In addition, the long holding time also caused considerable loss of the Ni binder. The loss of the Ni binder phase resulted in the increase of the porosity. Moreover, it was clear that holding time had a strong

effect on the grain size. For the holding time less than 0.6 ks, the growth of the grain size could be negligible. In contrast, for the holding time of 1.8 ks, the FeB grains congregated with each other and formed coarse grains. Long holding time resulted in large grain size. Therefore, no holding time for consolidating FeB-10Ni compact was necessary.

The difference of microstructure resulted in the difference of mechanical properties. Figure 3.27 showed the Vickers hardness and grain size of FeB-10Ni compacts sintered at 1473 K holding at the range of 0 to 1.8 ks. It could be seen that the hardness decreased with the increase of the holding time. The FeB-10Ni sintered at 1473 K was in liquid phase sintering. Prolonged the holding time may cause excessive increase of the liquid phase, which also resulted in the grain growth. The hardness of the compact was approximately inversely proportional to the grain size. In addition, long holding time would result in the liquid leakage and volatilization of the Ni binder phase. Lacking sufficient binder phase to fill in the pores resulted in the high porosity as shown in Fig 3.26(d). High porosity and coarse grains resulted in the decrease of the hardness.

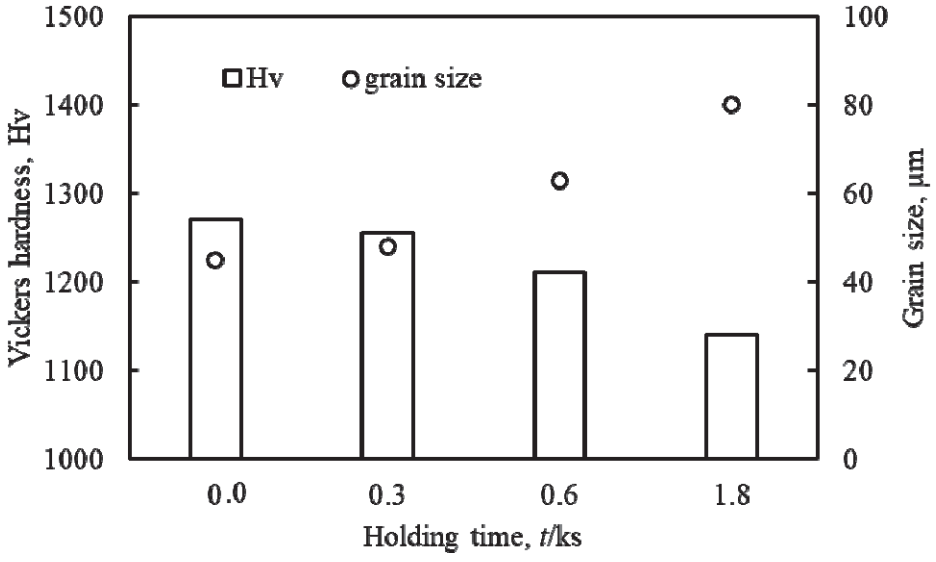

Figure 3.27 Vickers hardness and grain size of FeB-10Ni compacts sintered at 1473 K holding at the range of 0 to 1.8 ks.

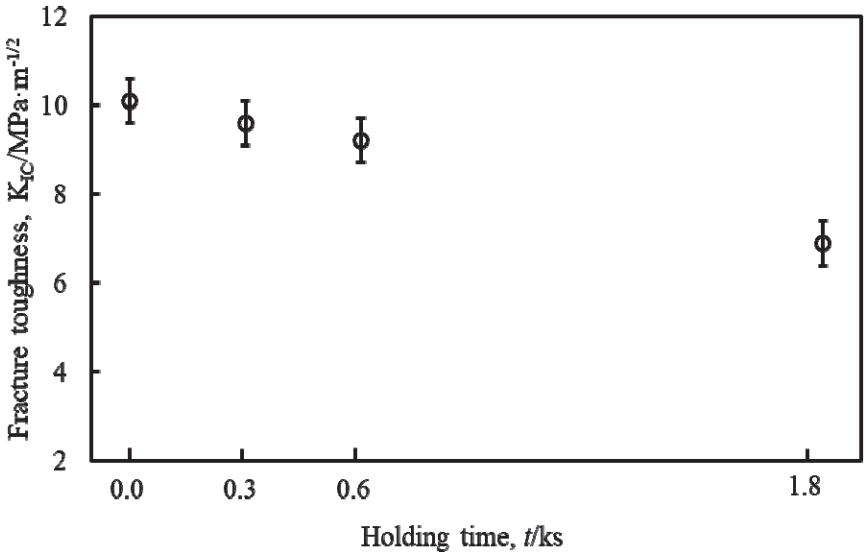

Figure 3.28 Fracture toughness of FeB-10Ni compacts sintered at 1473 K holding at the range of 0 to 1.8 ks.

Mechanical properties were highly related to the relatively density and microstructure[23]. Figure 3.28 showed the fracture toughness of FeB-10Ni compacts sintered at 1473 K for different holding times. In general, the fracture toughness was inversely proportional to the hardness. High hardness would result in low toughness. However, the fracture toughness decreased with the increase of the holding time, as shown in this figure. The fracture toughness was used to describe the resistance to crack growth. It was sensitive to the surface defects such as the pores and the cracks. The porosity increased with the increase of the holding time. High porosity resulted in the low fracture toughness. In addition, the finer grain size could make the crack deflect and improve the toughness. That means coarse grain size resulted in the decrease of the fracture toughness. Therefore, the FeB-10Ni compact sintered at 1473 K without holding time showed high fracture toughness.

3.4 Summary

The FeB-Ni hard compacts were fabricated by both electroless plating and spark sintering processes. The following results were found:

(1) The increased treating amount of bath and bath temperature would accelerate the chemical reaction rate, increase the Ni content and affect the homogeneity of the Ni coating. Electroless plating time had a greater impact on the increase of the Ni content. But they had no effect on the composition and structure of the coatings.

(2) The relative density of the FeB-Ni compacts increased with increase of the Ni content. The densification rate curves showed that the plastic deformation and power law creep deformation of the Ni binder phase in the FeB–Ni compacts occurred before and after reaching the maximum densification rate.

(3) The FeB-Ni compacts were fabricated by spark sintering processes under different conditions. The sintering temperature had a significant influence on the relative density and the homogeneous distribution of the Ni in the FeB-10Ni compacts. While, the holding time had a significant influence on the grain size, porosity and the mechanical properties of the compacts. FeB-10Ni with lower porosity was prepared at 1473 K without no holding time. FeB-10Ni compact possessed the maximum hardness (Hv 1289), compressive strength (953 MPa) and fracture toughness (10.1 $MPa \cdot m^{-1/2}$).

References

1) J. Colaruotolo, D. Tramontana. Engineering applications of electroless nickel. Electroless plating: fundamentals and applications, 1990, 8, 208.

2) S. F. Moustafa, Z. Abdel-Hamid, O. G. Baheig, et al. Synthesis of WC hard materials using coated powders. Advanced Powder Technology, 2011, 22(5), 596-601.

3) R. Thyagarajan, G. M. D. Cantin, B. P. Kashyap, et al. Modelling compaction behaviour of nickel–phosphorus and nickel–boron electroless coated titanium powders. Powder Technology, 2015, 274, 53-61.

4) L. M. Huang, L. M. Luo, X. Y. Ding, et al. Effects of simplified pretreatment process on the morphology of W–Cu composite powder prepared by electroless plating and its sintering characterization. Powder Technology, 2014, 258, 216-221.

5) R. C. Agarwala and V. Agarwala. Electroless alloy/composite coatings: A review. Sadhana, 2003, 28(3-4), 475-493.

6) M. Schlesinger and M. Paunovic. Modern electroplating. Vol. 55. John Wiley & Sons, 2000.

7) A. Chiba, H. Haijima and W. C. Wu. Effect of sonication on the electroless Ni–B deposited powder from acid bath. Ultrasonics, 2004, 42(1), 617-620.

8) D. Zhang, K. Sugio, K. Sakai, et al. Effect of spatial distribution of SiC particles on the tensile deformation behavior of Al-10 vol.% SiC composites. Materials transactions, 2007, 48(2), 171-177.

9) U. Sen, S. Sen, S. Koksal, et al. Fracture toughness of borides formed on boronized ductile iron. Materials & design, 2005, 26(2), 175-179.

10) A. K. Sinha. Boriding (boronizing). ASM Int. Handbook, Vol. 4 Materials Park, OH, (The Materials International Society, USA, 1991) pp. 437-447.

11) G. S. Upadhyaya. Materials science of cemented carbides—an overview. Materials & Design, 2001, 22(6), 483-489.

12) K. Matsugi. Behaviors and Process Analyses of Spark Sintering for Powders Having a Low Sinterability. Journal of Korean Powder Metallurgy Institute, 2012, 19(2), 127-133.

13) B. K. Kim, G. H. Ha and D. W. Lee. Sintering and microstructure of nanophase WC/Co hard metals. Journal of Materials Processing Technology, 1997, 63(1-3), 317-321.

14) K. Matsugi, K. Tomigahara, Y. B. Choi, et al. Production of hard materials with ubiquitously Fe-B system by spark sintering and their characteristics, J. Jpn. Soc. Powder Powder Metallurgy, 2011, 58, 487-494.

15) H. Kuramoto, K. Matsugi, K. Kawahara, et al. Sintering rate of pure copper powder uniaxially compressed in closed die in spark sintering process, J. Japan Institute Metals and Materials, 2002, 66, 621-626.

16) K. Matsugi, H. Kuramoto, O. Yanagisawa, et al. A case study for production of perfectly sintered complex compacts in rapid consolidation by spark sintering, Materials Science and Engineering A, 2003, 354(1-2), 234-242.

17) H. Kuramoto, K. Matsugi, K. Kawahara, et al. Densification rate of Cu-Al_2O_3 composite in the spark sintering process. J. Japan Institute of Metals and Materials, 2003, 67, 528-537.

18) S. Kang, Z. F. Xu, Y. B. Choi, et al. Spark sintering behavior of ubiquitously Fe-B and Fe powders and characterization of their hard composites. Materials Transactions, 2016, 57(5), 600-607.

19) S. Kang, Z. F. Xu, Y. B. Choi, et al. Spark sintering of ubiquitously FeB-25Ni powders and hardness properties. Materials transactions, 2016, 57(12), 2139-2145.

20) V. A. Tracey. Nickel in hardmetals. Int. J. Refract. Met. Hard Mater, 1992, 11(3), 137-149.

21) J. M. Barranco, R. Warenchak. Liquid phase sintering of carbides using a nickel-molybdenum alloy. Int. J. Refract. Met. Hard Mater., 1989, 8(2), 102-110.

22) T. W. Penrice. Alternative binders for hard metals. Carbide Tool J., 1988, 20(4), 12-15.

23) Y. Li, J. Zhang, G. Luo, et al. Densification and properties investigation of W-Cu composites prepared by electroless-plating and activated sintering. Int. J. Refract. Met. Hard Mater., 2018, 71, 255-261.

Chapter 4
Friction Experiments and Cutting Performance of FeB-10Ni Tools during Interrupted Cutting

4.1 Introduction

Cemented carbide was used to designate a metal matrix composite constituted by hard ceramic particles, normally WC, into a metallic matrix. The importance of the invention of WC was confirmed by noting that today, ninety years later, were still a very significant product of tool materials industry. Nowadays, almost 67% of total production of cemented carbides goes into metal cutting tools[1)]. One of the main topics of the actual research in the field of cemented carbides mainly involved the development of new composites, partially or wholly replacing the traditional cobalt binder by other more economic and less toxic materials[2)]. The FeB-10Ni alloy manufactured by the pressing and sintering of Ni coated FeB powders was selected to substitute the WC-Co material. It was necessary to measure the cutting performance of FeB-10Ni alloy as a cutting tool.

The cutting tool was one of the major components of the metal machining system[3)]. Metal machining processes were industrial processes in which metal parts were shaped by the removal of unwanted material using cutting tools. During the cutting process, the tool removed a part of the workpiece by a process of intense plastic deformation at high strain rate[4)]. The cutting face was subjected to sever wear and great pressure which seriously increased tool damage, especially in dry machining of Ti alloys. WC-Co cutting tools had proven their superiority in almost all machining processes of Ti alloys[5)]. Generally, the cutting speed for WC-Co tools was lower than 45 m/min[6,7)]. Ti alloys possessed high chemical activities and tended to weld to cutting tools that caused chipping and premature tool failure during machining. Furthermore, its low thermal conductivity increased the temperature of the tool/workpiece interface which adversely affected tool life[8)]. However, the cutting temperature was in excess of 1073 K at the cutting speed 0.5

m/s[5]. According to the binary phase diagram of Fe-Ti as shown in Fig.4.1[9], the chemical reaction of Fe and Ti would be occur over 973 K. In this case, the cutting speed of FeB-10Ni tool in dry machining of Ti-6Al-4V was investigated lower than 0.5 m/s.

In addition, with the progress in machining technology, dry cutting was applied in consideration of higher demand of die quality, cost, effectiveness and environmental requirement[10]. Friction played an important role in metal cutting. The tool wear during metal cutting process directly affected the quality of the machined surface and increased the consumption of tool materials. In this chapter, the friction and wear characteristics between FeB-10Ni cutting tool and Ti64 friction pair were first investigated. The experimental parameters of friction and wear were consistent with the cutting parameters such as the cutting pressure, speed and length. The influence of sliding speed on the friction coefficient, wear volume loss and wear morphology of FeB-10Ni alloy was analyzed. The mechanism of friction and wear was discussed. On the basis of which, the tool wear mechanism of this alloy in cutting Ti alloy was investigated.

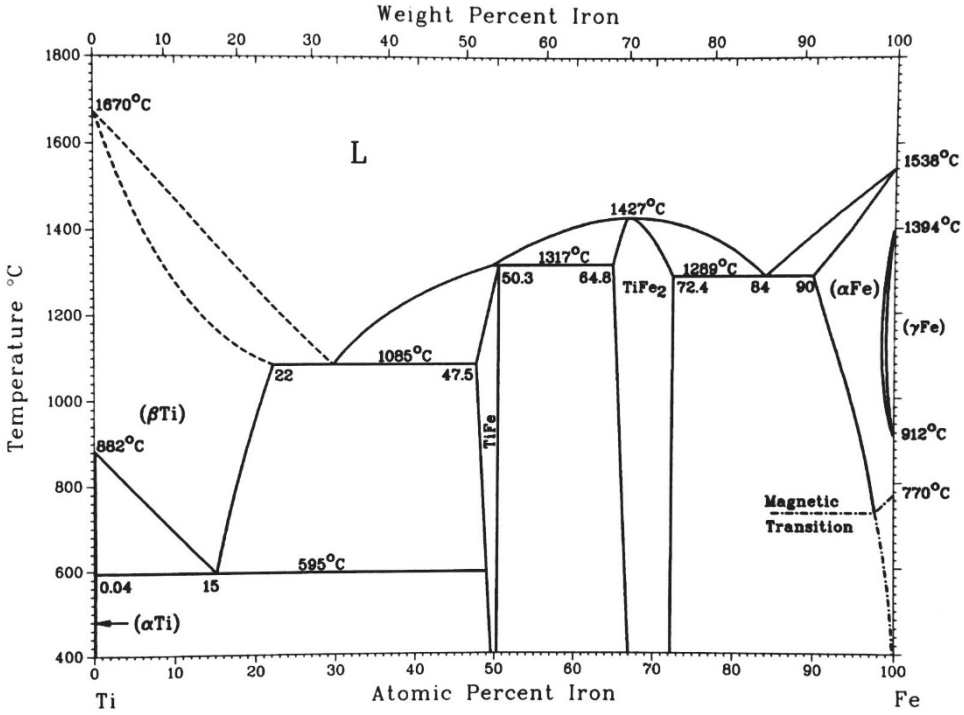

Figure 4.1 Fe-Ti phase diagram[9].

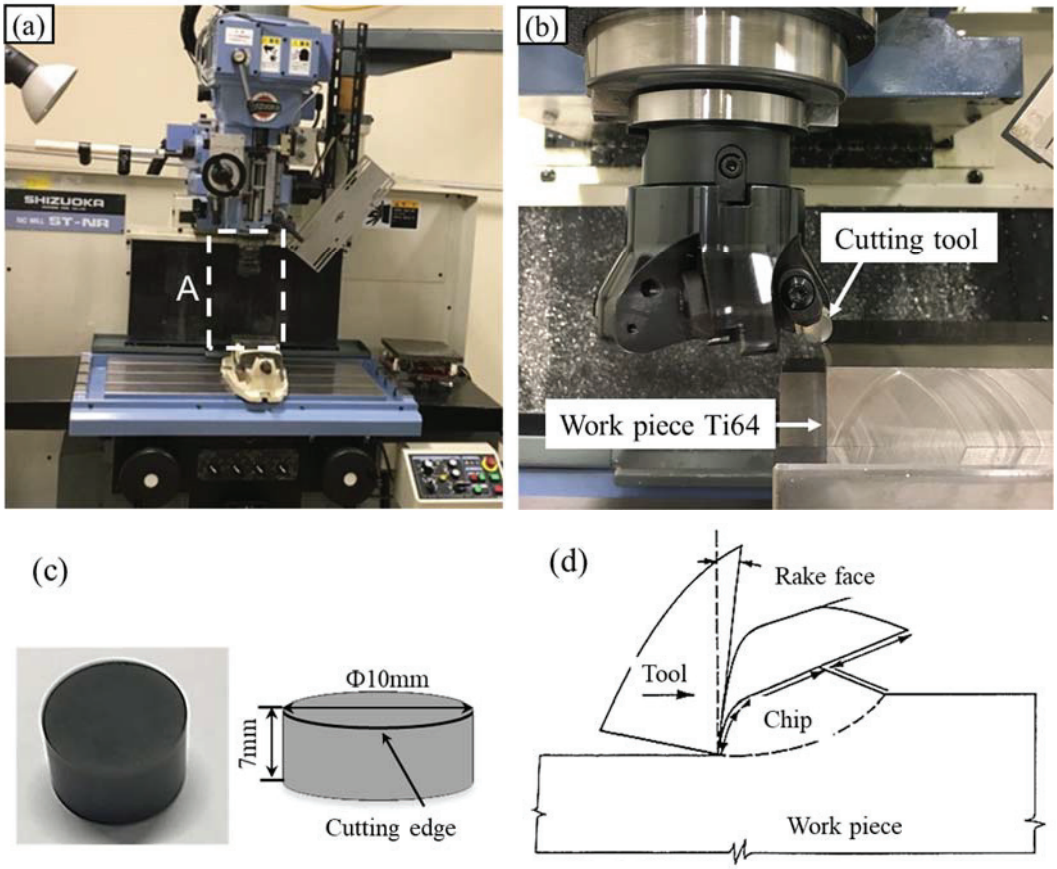

Figure 4.2 (a)The illustration of the milling machine, (b) the enlarge image of the part A in (a), (c) illustration of the cutting tool and (d) the chip-formation process, respectively.

4.2 Experimental procedure

4.2.1 Materials

FeB-10Ni powders were prepared by electroless plating using as-received FeB powders. Then the electroless Ni plated FeB powders were consolidated by spark sintering process at 1473 K without no holding time. The sintered compact was grinding and polishing to the suitable tool size, as shown in Fig. 4.2. The wear and cutting performance of the sintered FeB-10Ni tool were tested in comparison with that of a commercially available cemented carbide tool (WC-7.8Co sintered at 1523 K). The microstructure of FeB-10Ni and WC-7.8Co tools were shown in Fig. 4.3. The mechanical properties of the two kinds of tool materials were listed in table 4.1. Hardness was measured by Vickers hardness tester under a constant load of 9.8 N. The fracture

toughness, K_{IC}, of the WC-7.8Co compact was determined by measuring the crack length near the indent and calculated by using the following equation (1)[11].

$$K_{IC}=0.016\sqrt{\frac{E}{H}}\,P/\,c^{3/2} \quad (1)$$

The Young's modulus, E, was 628 GPa according to the rule of mixtures calculation between the Young's modulus of WC and Co[12,13]. H was the Vickers hardness, P was the indentation load, and c was the crack length near the indent. The counter material was Ti-6Al-4V (Ti64, Ofa Co., Ltd. Japan). The microstructure, chemical composition and properties were shown in Fig. 4.4, table 4.2 and table 4.3, respectively. The initial microstructure of the Ti64 alloy consisted of α matrix and the lamellar structure of (α+β) grains.

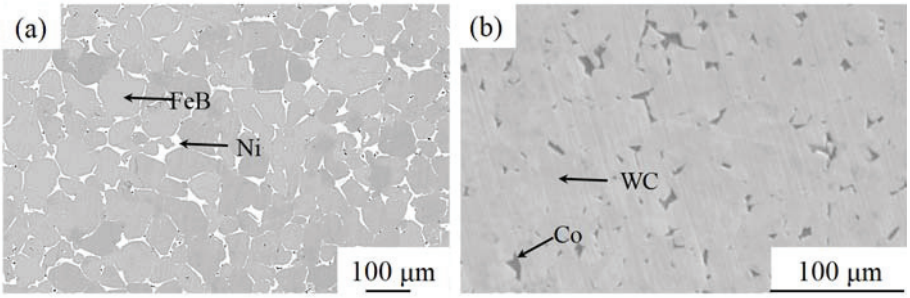

Figure 4.3 Compositional images of (a) FeB-10Ni compact sintered at 1473 K and (b) WC-7.8Co compact sintered at 1523 K.

Table 4.1 Properties of the FeB-10Ni and WC-7.8Co tool materials

Properties	Cutting tools	
	FeB-10Ni	WC-7.8Co
Density, g·cm^{-3}	6.61	14.8
Porosity, %	0.1	0.1
Vickers hardness, Hv	1289	1411
Fracture toughness, (MPa·m$^{-1/2}$)	10.1	11.8
Thermal conductivity, (W/(m·K))	18.7	33.3
Compressive strength, MPa	952	1356

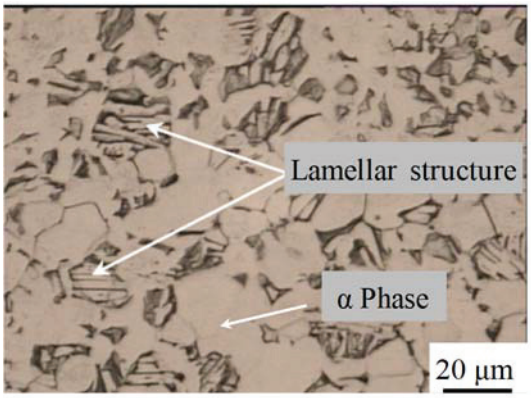

Figure 4.4 Microstructure of Ti-6Al-4V alloy.

Table 4.2 Chemical composition of Ti-6Al-4V alloy.

	N	C	H	Fe	O	Al	V	Ti
wt.%	0.05	0.08	0.15	0.40	0.20	5.5-6.75	3.5-4.5	balance

Table 4.3 Properties of Ti-6Al-4V alloy.

Material / Properties	Ti-6Al-4V
Density, ($g \cdot cm^{-3}$)	4.43
Young's modulus, (GPa)	113
Thermal conductivity, (W/(m·K))	7.5
Vickers hardness, Hv	438
Tensile strength, MPa	895
Yield strength (0.2%), MPa	828
Elongation, %	10.2

4.2.2 Friction and wear tests

The friction and wear tests were conducted under dry sliding conditions using a pin-on-disc type tribometer at room temperature, as shown in Fig.4.5. The size of the pin and disc were shown in Fig.4.6. The disc was corresponding to the sintered FeB-10Ni and

WC-7.8Co compacts. The pin was corresponding to the counter material of Ti64 alloy. The sliding speed was systematically changed at the range of 0.03-0.17 m/s under a constant pressure of 49 N. The sliding distance was 30 m. The constant pressure was estimated by the following empirical equation of cutting pressure[3)]

$$u_s=Ft/fd \quad (2)$$

where u_s was the specific cutting power, also called the unit cutting energy, Ft was the tangential cutting force, f was the feed rate, d was the depth of cut. The typical value of the unit cutting energy for titanium was 0.053-0.066 $kW/cm^3/min$[3)].

The dynamic friction coefficient was measured by the wear tester. For the measurements of wear volume loss, the compacts and counter materials were cleaned before and after each test with acetone in an ultrasonic bath for 0.3 ks and subsequently dried. Wear loss of the compacts (Vs) and counter materials (Vc) was obtained by weighing the pairs before and after the sliding using a digital balance with a scale 0.1 mg. The microstructural and morphological features of the surfaces after friction and wear tests were examined using the EPMA. The point analysis measured by EPMA was also used to reveal the operative wear mechanisms.

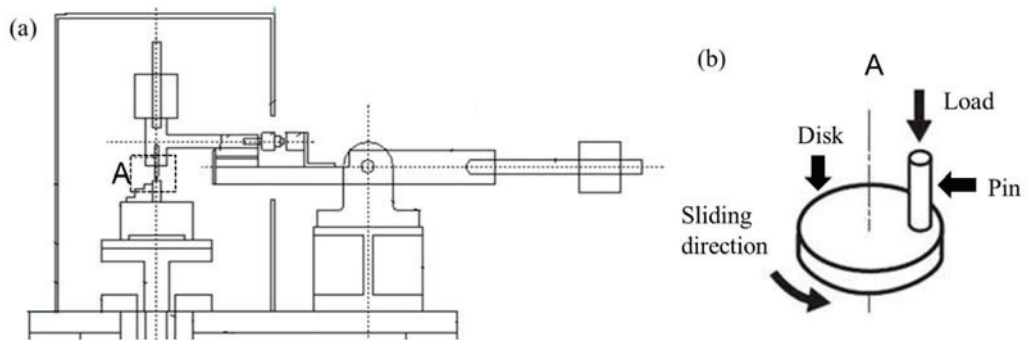

Figure 4.5 (a) Schematic diagrams of pin-on-disk friction and wear tester, (b) the enlarge image of the part A in (a).

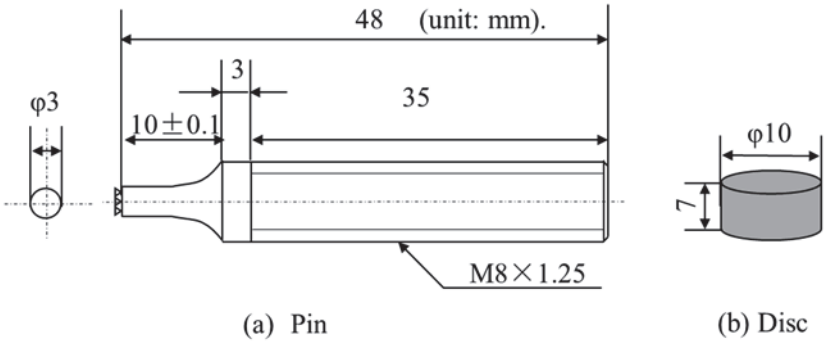

Figure 4.6 Size of the (a) pin and (b) disc.

4.2.3 Cutting tests

The quality of machining, machining costs and cutting productivity were directly affected by the cutting performance of the tools. The cutting performance of the tool material was mainly related to tool life. Tool life could be characterized by the cutting time of cutting tool without adjustment or replacement, the number of parts machined, the cutting length or the area of the machined surface[4]. In this research, the tool life was defined as the cutting length when the flank wear reached the allowed limit equal to the criterion by interrupted cutting tests. This was because flank wear width was easier to measure and related to machined surface quality.

The interrupted cutting was carried out on a ST-NR Mill machine under dry conditions as shown in Fig.4.2. The interrupted cutting cycle (the pattern of the cutting time to air-cutting time) was shown in Fig.4.7 and table 4.4. The cutting parameters were listed in Table 4.5. The workpiece material used in the interrupted cutting was Ti-6Al-4V in the form of cubic 100 mm in length, 80 mm in width and 60 mm in height. Flank wear width VB (0.3) mm was used as the tool life criterion, while excessive chipping (flaking) or catastrophic fracture of the cutting edge was also employed as the failure criteria. The conditions of the cutting edge were examined at constant cutting length. The worn or fractured tool surface of the cutting tool and the distribution components of the adhered material were investigated by the EPMA.

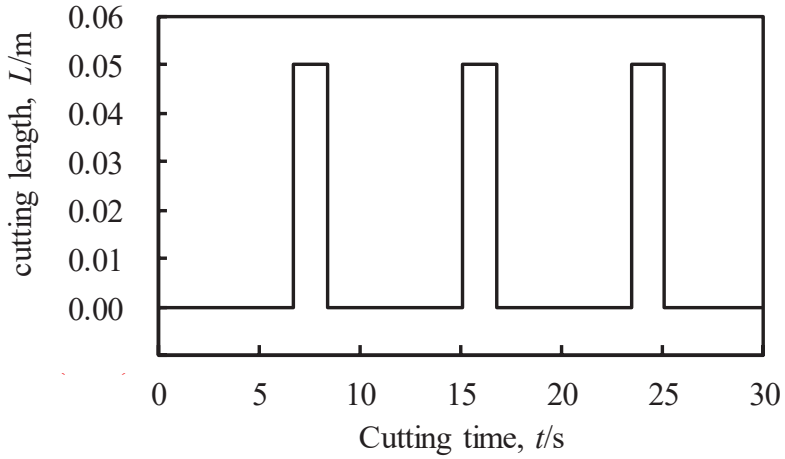

Figure 4.7 Relation between the cutting length and the actual cutting time for every cycle at the cutting speed of 0.03 m/s.

Table 4.4 Relation between the cutting speed and the actual cutting time for every cycle

Cutting speed, m/s	0.03	0.05	0.17	0.33
Cutting time, s	1.67	1.00	0.29	0.15

Table 4.5 Interrupted cutting parameters for FeB-10Ni and WC-7.8Co tools.

Operation	Cutting speed v (m/s)	Feed rate f (mm/r)	Depth of cut a_p (mm)
Interrupted cutting	0.03, 0.05, 0.17 and 0.33	0.05	0.2

4.3 Results and discussion

4.3.1 Wear properties

4.3.1.1 Friction coefficient

Friction coefficient curves as function of sliding distance under 49 N normal contact force for FeB-10Ni and WC–7.8Co discs versus Ti64 pin combinations were shown in

Fig. 4.8. The dynamic friction coefficients of the FeB-10Ni and WC-7.8Co tribo-pairs were measured to be in the range of 0.40–0.48. Generally, friction and wear behaviors could be divided into three stages[14]. The initial stage was the running in stage, in which the friction coefficient was abruptly increased. The second stage was steady stage, in which the friction coefficient was kept constant. The final stage was severe wear stage, in which the friction coefficient was increased rapidly. As shown in Fig. 4.8, it was found that the wear behavior of the FeB-10Ni and WC-7.8Co contained running in and steady stages. The abruptly increased friction coefficient of both compacts could be explained by schematic of the wear process as shown in Fig. 4.9. The initial friction should be mainly caused by strong asperity interaction such as fragmentation and deformation between the pin and disc[15]. Properties of contact surfaces were crucial to surface interaction because surface properties affect real area of contact, friction and wear. When the FeB-10Ni and Ti64 were placed in contact, surface roughness caused contact to occur at discrete contact spots (junctions). The total areas of all the contact spots constituted the real (true) contact area. This would be only a small fraction of the apparent (nominal) contact area, which resulted in high contact stress and friction[16]. The real contact area was a function of the surface texture, material properties and interfacial load conditions. The contact asperities results in adhesive contacts caused by interatomic interactions. When two surfaces moved relative to each other, the friction force was contributed by adhesion of these asperities and other sources of surface interactions. In addition, the Ti64 alloy was easy to adhesive, related to the mechanism of friction issued by Bowden and Tabor[17],

$$f=Ar\cdot \tau_s \tag{3}$$

where f, Ar and τ_s were friction force, actual contact area and shear strength (load/apparent contact area) of soft materials, respectively. As a result, the friction coefficient of the two compacts was increased with the increased of the friction force in the initial state.

After initial state, the friction coefficient of FeB-10Ni compacts showed similar evolution as function of the sliding distance, regardless of the sliding speed. While, the friction coefficient of WC-7.8Co was noticed to decrease and then increase at the sliding

speed of 0.05 and 0.17 m/s. It was thought to be caused by formation and periodic, localized fracture of a surface layer of the FeB-10Ni/Ti trio-pairs as shown in Fig.4.9. While for the WC-7.8Co/Ti trio-pairs, the surface asperities were first flattened before the localized fracture of the surface layer at the sliding speed of 0.05 and 0.17 m/s due to the higher hardness of WC-7.8Co. The actual contact area increased with the flattened asperities. Therefore, the contact stress was decreased as well as the friction coefficient. As the friction progressed, the surface layer was destroyed and the friction coefficient was increased until formed new friction film. No decrease of the friction coefficient of WC-7.8Co appeared at 0.03 m/s. It was considered that the new friction film was formed before flattening of the asperities due to the strong adhesion of the Ti alloys, especially at lower speed.

During sliding, variations in the conditions of mating surfaces occurred which affected friction and wear properties. As the sliding proceeded, the small oscillations in the steady state of the friction coefficient curves appeared. It was caused by the continuous fracture and regeneration of micro junctions as a consequently by the microscopic interaction. It should be related to the changing interlocking degree between the contact surfaces of the pin and disc. This was typical stick–slip behavior in the case of titanium and Ti alloys. The friction coefficient of FeB-10Ni and WC-7.8Co changed a few percent for a change in speed as shown in Fig.4.8. Generally, the friction coefficient decreased with the increase of the sliding speed[18]. The displacement per unit time increased with an increase in the sliding speed which lead to the formation of a lubricant film on the material surface, which, in turn, caused the decrease in the friction coefficient[19]. In addition, high sliding speeds could result in high interface (flash) temperatures which may form low shear strength surface films because of the low thermal conductivity of the Ti64 alloy[16].

As can be seen in Fig. 4.8, there were no significant difference in friction coefficient of FeB-10Ni and WC-7.8Co under different sliding speeds. According to the research of Boden et al[17] that the factors influenced the friction coefficient were mainly the chemical properties of the Ti64 alloys, surface roughness, load, temperature, sliding speed and the surface film. In this case, the effect of the hardness on the friction coefficient could be

negligible due to the same wear mechanism. In addition, the load, temperature, chemical properties of the Ti64 alloys and the sliding speed were in the same conditions. It was considered that the similar friction coefficient was related to the same experimental conditions.

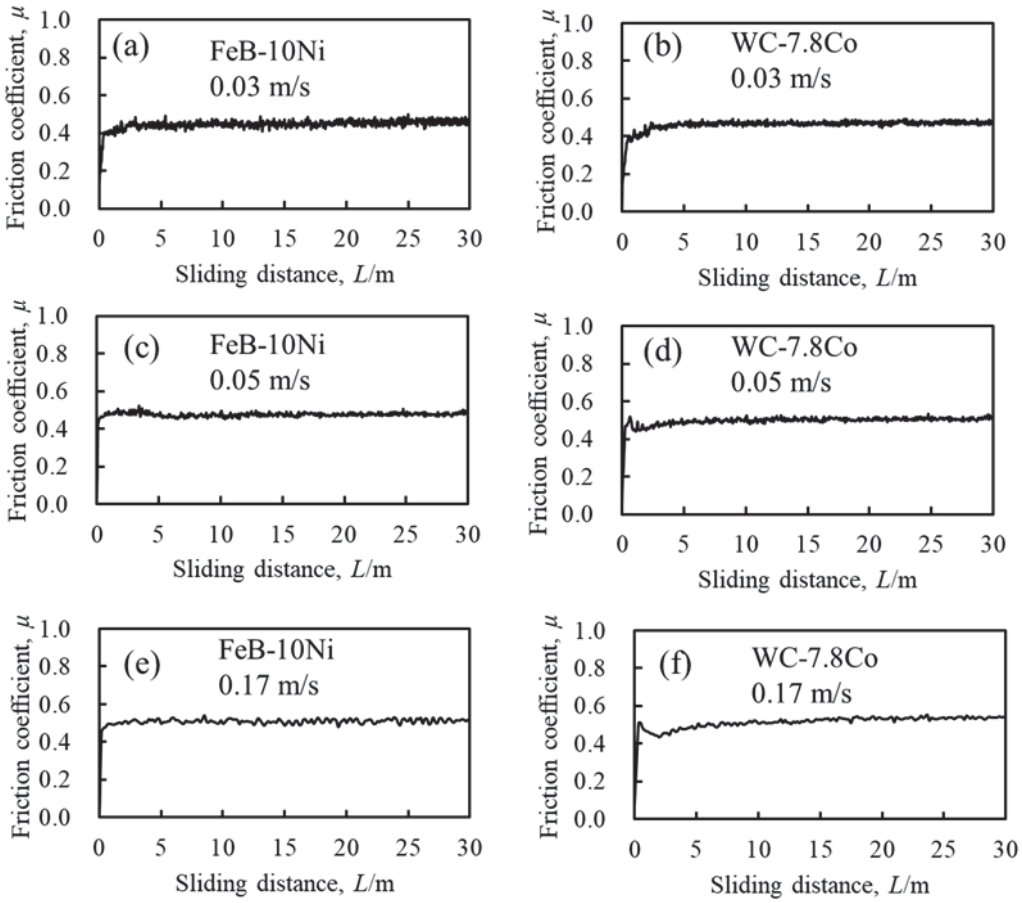

Figure 4.8 Dynamic friction coefficient of the FeB-10Ni and WC-7.8Co compacts under the sliding speed of (a), (b) 0.03 m/s, (c), (d) 0.05 m/s and (e) (f) 0.17 m/s.

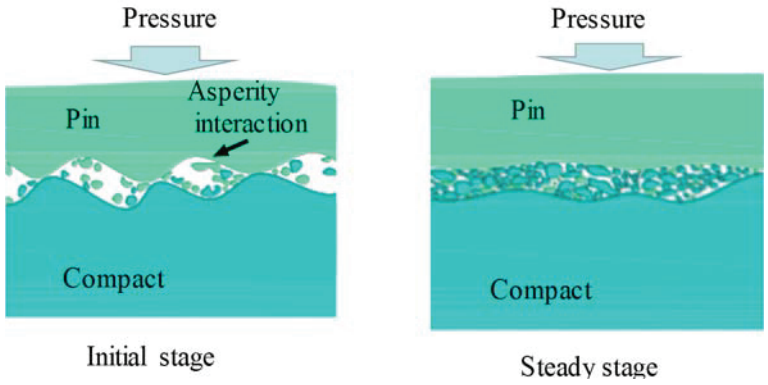

Figure 4.9 Schematic of the wear process.

4.3.1.2 Wear volume loss

The variation of weight loss of FeB-10Ni, WC-7.8Co and the corresponding Ti64 counter materials were shown in Fig. 4.10. It could be seen that the weight loss of FeB-10Ni compacts in all states gradually increased with the increasing speed as well as the WC-7.8Co. In the steady state of wear, the wear volume loss of the FeB-10Ni and the WC-7.8Co compacts increased slowly. However, the wear loss of counter materials coupled with FeB-10Ni was higher than that of WC-7.8Co. It was considered that the wear debris of FeB-10Ni or WC-7.8Co promoted the abrasion wear. Ti64 alloys possessed strong adhesion and spring back. The fracture of the adhesive Ti64 alloy peeled off the FeB-10Ni and WC-7.8Co particles during the wear process. The grain size of FeB-10Ni was higher than that of WC-7.8Co. FeB grains were easier to pull out by the adhesive Ti64 alloy. In the wear tests, more wear debris caused higher wear volume loss of the Ti64 alloys.

In order to further compare the wear properties of the FeB-10Ni and WC-7.8Co, wear ratio of the FeB-10Ni and WC-7.8Co corresponding to the counter materials Ti64 alloy was shown in Fig. 4.11. The wear ratio was obtained by the wear volume loss of the counter materials verse the compacts. Higher wear ratio means higher wear resistance. In this figure, the wear ratio of FeB-10Ni decreased with the increasing sliding speed as well as the WC-7.8Co. The wear ratio of the FeB-10Ni as a function of sliding speed generally had a negative slope. It was found that there was no considerable change in the wear ratio between the FeB-10Ni and WC-7.8Co compacts under different sliding speed, although the hardness of WC-7.8Co was higher than that of FeB-10Ni. As mentioned above, the wear volume loss of Ti64 counter material in FeB-10Ni tribo-pair was much larger than that of WC-7.8Co tribo-pair, while the wear volume of FeB-10Ni just slightly larger than that of WC-7.8Co. This result could be rationalized with the help of the wear mechanisms operating in the two compacts during dry sliding, such as adhesion, clearly seen on the worn surfaces.

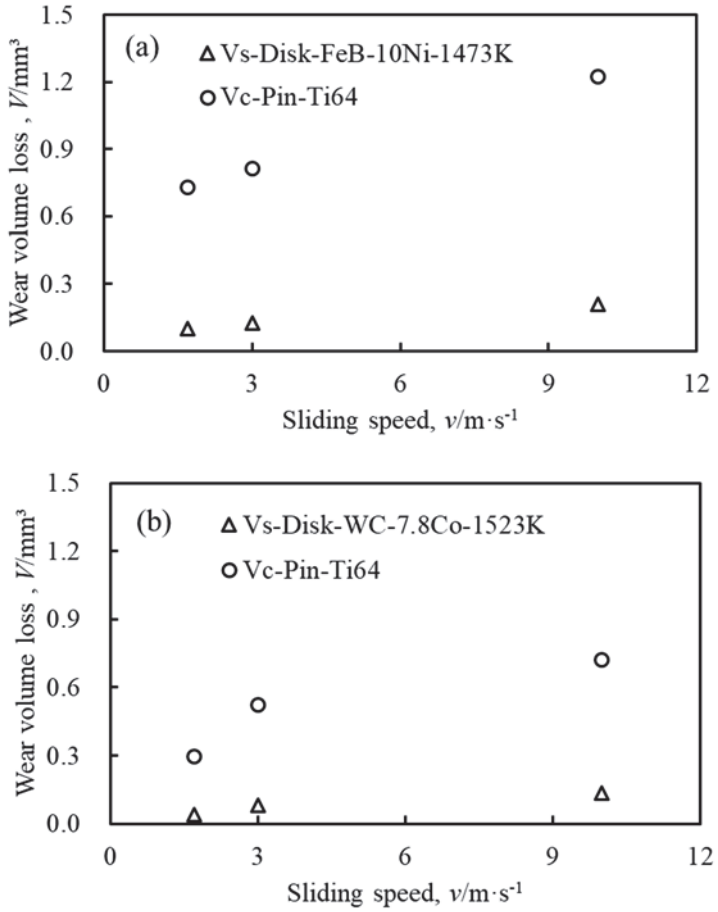

Figure 4.10 (a) Wear volume loss of the FeB-10Ni compacts and (b) WC-7.8Co compacts corresponding to the counter materials Ti64.

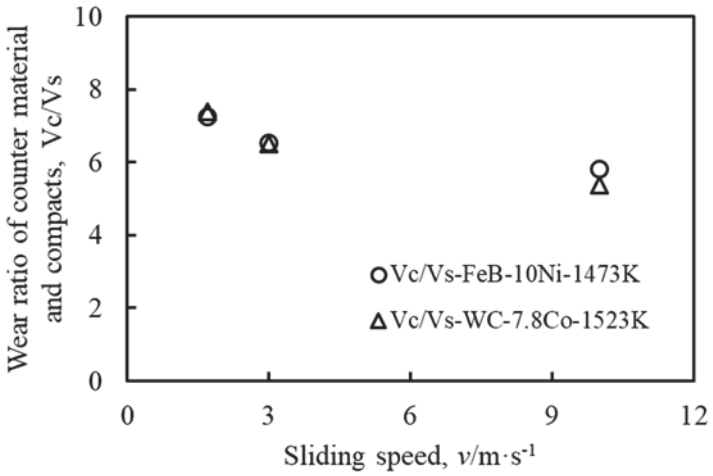

Figure 4.11 Wear ratio of Ti64 counter material and FeB-10Ni, WC-7.8Co compacts under different sliding speeds.

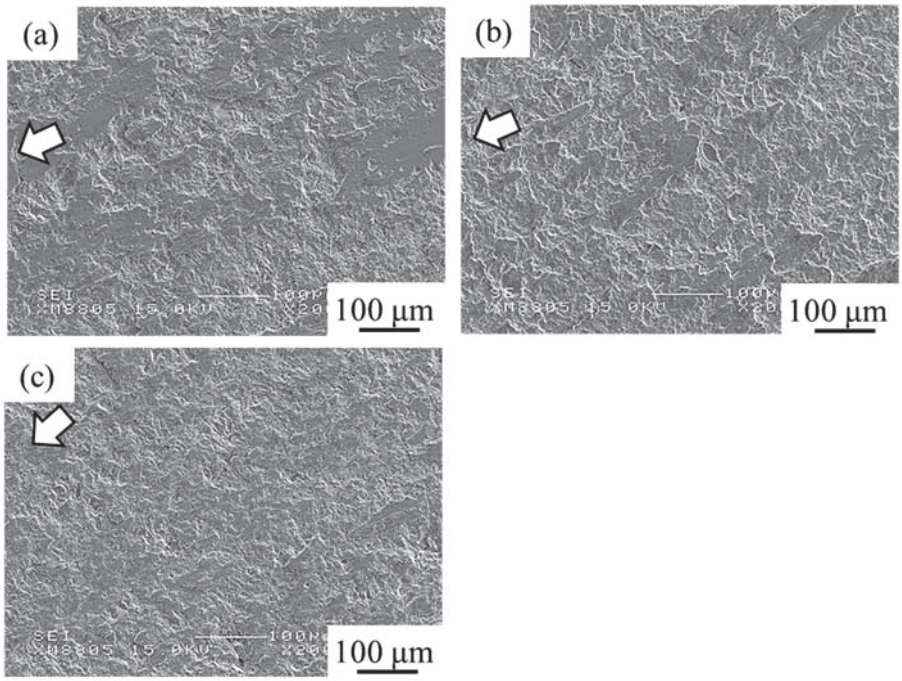

Figure 4.12 SEM images of FeB-10Ni compacts after wear tests under the sliding speed of (a) 0.03, (b) 0.05 and (c) 0.17 m/s. The direction of the wear tests was indicated by the arrows.

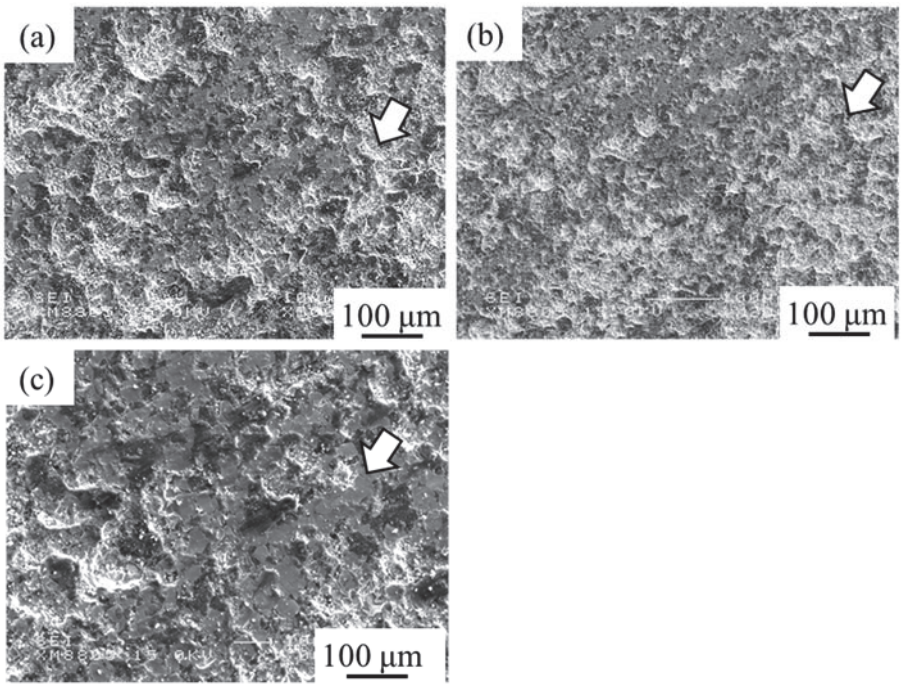

Figure 4.13 SEM images of WC-7.8Co compacts after wear tests under the sliding speed of (a) 0.03, (b) 0.05 and (c) 0.17 m/s. The direction of the wear tests was indicated by the arrows.

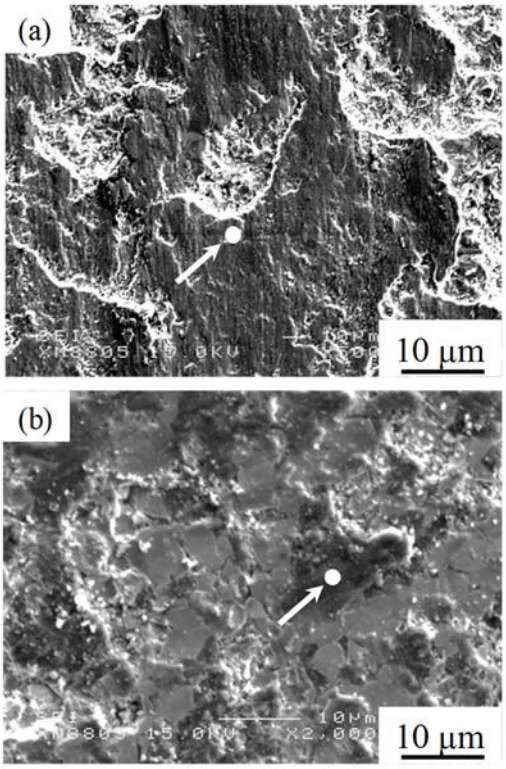

Elements	At.%
Fe	30.4
Ni	6.1
B	5.7
O	6.1
Ti	36.1
Al	4.4
V	1.2

Elements	At.%
W	13.4
C	1.1
Co	4.1
O	19.6
Ti	42.7
Al	16.6
V	2.5

Figure 4.14 SEM images of (a) FeB-10Ni and (b) WC-7.8Co and the corresponding point analysis indicated by the arrows at sliding speed of 0.03 m/s. Insert tables were the results of point analysis.

4.3.1.3 Worn surface morphology

Worn surfaces of the FeB-10Ni and WC-7.8Co compacts after wear tests under different sliding speed were shown in Fig. 4.12 and 4.13. The sliding directions were indicated by the arrows in the SEM images. The FeB-10Ni compacts exhibited similar surface appearance with grain fragmentation, smearing, pits and adhesion under different sliding speed as shown in Fig. 4.12 (a), (b) and (c). In the process of sliding speed increasing from 0.03 to 0.17 m/s, the amount of wear debris of FeB-10Ni compacts was significant growth and more pits appeared. No considerable plastic deformation, wear scars like scratches/grooves were seen on the worn surface, which indicated very low abrasion wear. More rugged worn surface was exhibited with the increasing sliding speed. In contrary, FeB-10Ni compacts showed distinctly adhesive wear as well as the WC-7.8Co. The adhesion marks were more prominent at relatively low sliding speed as shown

in Fig. 4.12(a) and 4.13(a), where the marks from the broken adhesion joints and smearing were evident. WC-7.8Co showed adhesive wear mechanism with FeB-10Ni as shown in Fig.4.13.

In Fig. 4.14, the point analysis of the two compacts showed adhesive wear on the worn surfaces. Among them, adhesion appeared to be the dominant mechanisms. In this figure, the fragmentation of the FeB and WC grains was observed. The broken grains were easily scraped off by the adhesion during the wear process. The exposed metal surface may then be spalling. The existence of oxygen may also deteriorate the mechanical properties of the compacts. This lead to a continuous removal and re-formation of the fragmentation layer and resulted in gradual consumption of the compacts during sliding[20,21].

The fragmentation of grains also brought about a secondary wear mechanism of abrasion for the FeB-10Ni and WC-7.8Co samples. The peeled of the grains during sliding created the potential for abrasive wear, where the wear debris may be swept aside or cause abrasion of the tribo-pairs, resulting in enhanced wear, especially for the relatively soft Ti64 alloy[20]. As shown in Fig. 4.15, the worn surfaces of the pins exhibited abrasion marks characterized by scratches and deep grooves. Moreover, the abrasion wear of the FeB-10Ni tribo-pairs was more serious than that of WC-7.8Co which was consistent with the results shown in Fig. 4.10. Together with the present results, this indicated that wear tests in Ti64 with strong affinity, the dry friction conditions and operative wear mechanisms outweighed the effect of hardness on the wear resistance.

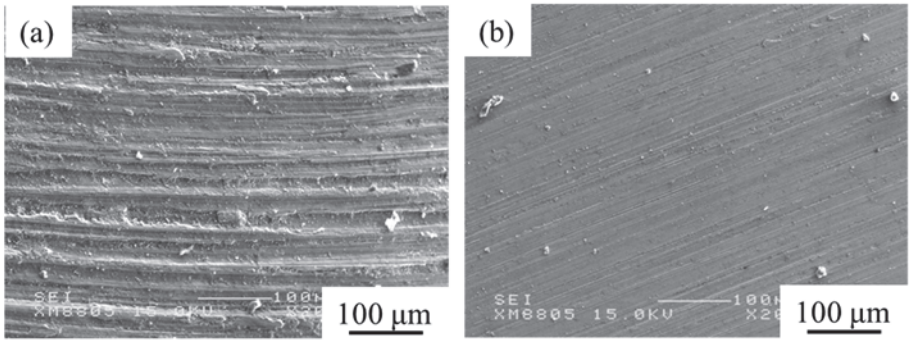

Figure 4.15 Worn surfaces of the pin corresponding to the (a) FeB-10Ni and (b) WC-7.8Co at the sliding speed of 0.03 m/s.

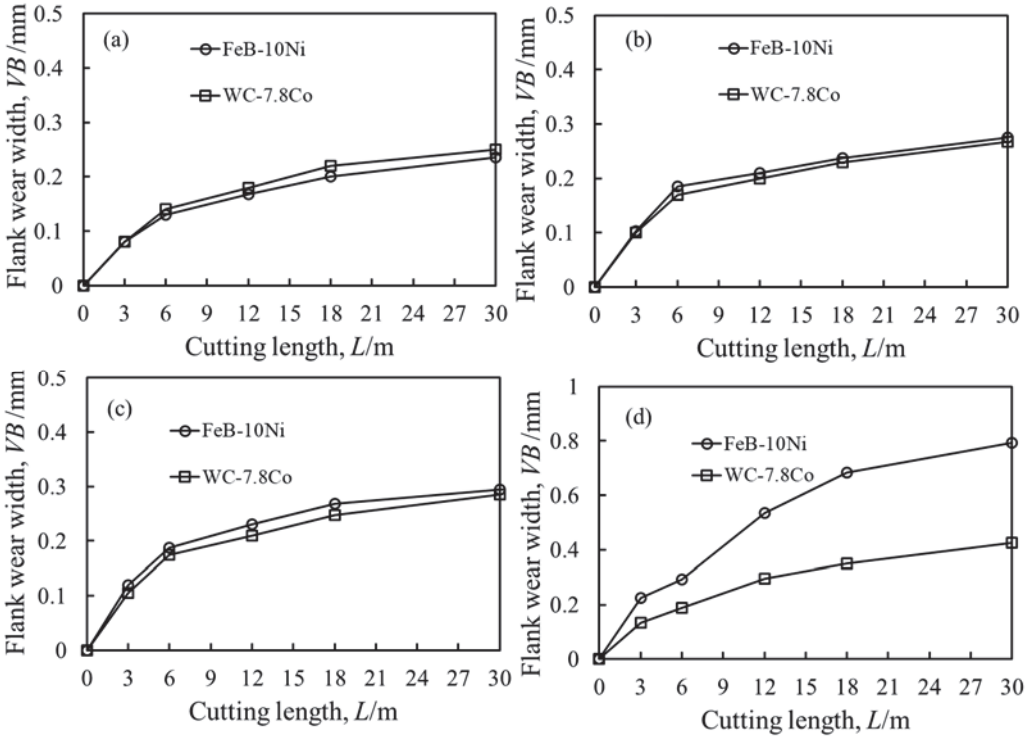

Figure 4.16 Relation between flake wear width VB and cutting length for FeB-10Ni and WC-7.8 Co at the sliding speed of (a) 0.03, (b) 0.05, (c) 0.17 and (d) 0.33 m/s.

4.3.2 Cutting performance of the FeB-10Ni compacts

4.3.2.1 Cutting behaviors of the FeB-10Ni compacts

During the machining process, the tool life could be defined by progressive wear on the rake face and/or clearance face of the tool, that was, crater wear and flank wear, instead of catastrophic tool failure. Flank wear had a major negative influence on the dimensional accuracy and surface finish of the counter materials as well as the stability of the machining process when the flank wear width VB reached a certain value. The flank wear width VB of both FeB-10Ni and WC-7.8Co was measured and plotted as a function of cutting length as shown in Fig. 4.16. It was noted that larger cutting speed means serious thermal and mechanical impact on the cutting tool. Therefore, it could be concluded that the flank wear width VB of both cutting tools increased with the cutting speed when cutting Ti64 alloys[22]. Classical tool wear process contained three stages including rapid initial wear followed by gradual or steady wear and finally rapid or catastrophic wear which same to the friction and wear process[23]. For the cutting speed

lower than 0.33 m/s, the tool wear was in the initial wear stage when the cutting length was less than 6m. After that the tool wear entered the steady wear stage. Although flank wear width VB of FeB-10Ni was higher than that of WC-7.8Co, the VB of FeB-10Ni was still within the criterion range. As the cutting speed reaching 0.33 m/s, tool wear process entered the sever tool wear stage for the VB beyond the criterion even at the cutting length of 6m.

In addition, the friction coefficient between cutting tools and workpiece would directly affect the tool wear behaviors and machined surface quality during the machining process. At the initial wear stage, the flank wear width varied rapidly. With the development of tool wear, the flank wear width increased at steady wear stage. The variation tendency of the flank wear width was consistent with that of friction coefficient. Associated with the adhesive Ti alloys under the tool wear condition, the effect of adhesion should be significant in the tool wear.

Figure 4.17 showed the wear rate of the FeB-10Ni and WC-7.8Co cutting tools under different cutting speeds. The wear rate could be calculated by the slop of the flank wear width and cutting speed under steady state shown in Fig. 4.16, according to the equation[3]:

$$\eta_f = \sin\theta \frac{dVB}{dL} \quad (4)$$

where θ was the relief angle. As can be seen in this figure, the wear rate of the two cutting tools gradually increased with the cutting speed. The wear rate of the FeB-10Ni cutting tools increased rapidly than that of WC-7.8Co when the cutting speed beyond 0.17 m/s. The large difference of the wear rate between FeB-10Ni and WC-7.8Co was probably due to the differences of microstructure, thermal conductivity or the interfacial strength.

FeB-10Ni compact showed lower fracture toughness than that of WC-7.8Co compact. During the cutting tests, the cutting tool suffered severe impact as the cutting speed reaching to 0.33 m/s when machining Ti64 alloys[5]. The tool edge of the FeB-10Ni was broken due to the low fracture toughness as could be seen from the flank wear images of the FeB-10Ni tools. Cutting tool material of FeB-10Ni was taken away during the high speed cutting tests due to the fracture of the tool. The catastrophic loss of the tool materials resulted in the tool failure and high wear rate due to the high impact force and low fracture toughness. While, there were no catastrophic loss of the tool materials

occurred in the WC-7.8Co tool. Therefore, the increase of the wear rate of WC-7.8Co tool was far less than that of FeB-10Ni tool.

In addition, the interfacial strength characterized by the compressive strength and hardness of WC-7.8Co tool were also higher than that of FeB-10Ni tool due to the fine grain size as shown in table 4.3. These were also the reasons caused the differences of wear rate. While, under the cutting speed less than 0.17 m/s, the wear rate of the FeB-10Ni cutting tool was the same level to that of WC-7.8Co due to the low thermal and mechanical impact. In addition, high temperature would deteriorate the mechanical properties of the cutting tool, which resulted in the rapid increase of the wear rate of the tool. The high temperature resistance of WC-7.8Co tool possessed high thermal conductivity was better than that of FeB-10Ni tool. In this case, FeB-10Ni tool was more suitable to use at the cutting speed less than 0.17 m/s.

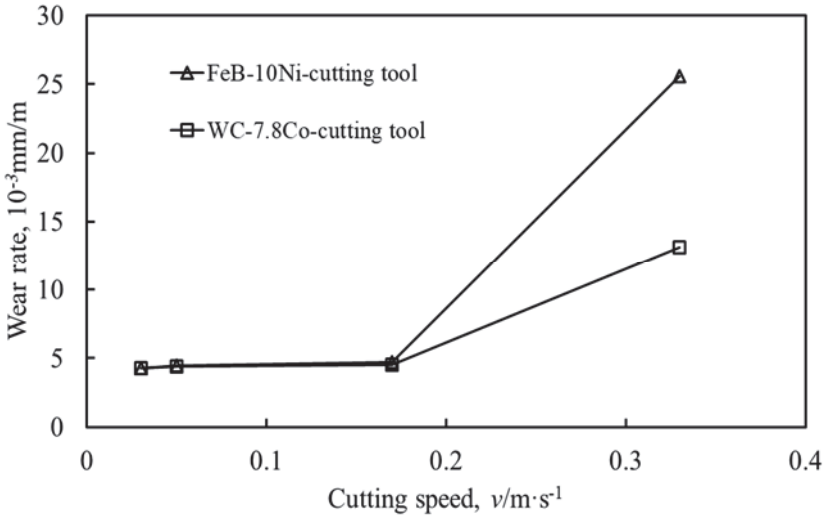

Figure 4.17 Relation between the wear rate and cutting speeds for FeB-10Ni and WC-7.8 Co cutting tools.

4.3.2.2 Tool wear of the FeB-10Ni cutting tool

A cutting tool was considered to have failed when it had worn sufficiently that dimensional tolerance or surface finish were impaired or when there was catastrophic tool failure or impending catastrophic tool failure. The principle types of tool wear, classified

according to the regions of the tool they affect, were shown in Fig. 4.18. Tool wear gradually occurred on the top rake face and the flank face due to the contact friction between the tool–workpiece and tool–chip. The morphologies of rake face of the FeB-10Ni and WC-7.8Co cutting tools tested under different cutting speeds were shown in Fig. 4.19-4.22, respectively. The state of cutting length at 6 m was the end stage of initial tool wear and started entering steady tool wear stage, while the state of cutting length at 30 m was the end stage of the steady tool wear and started entering the severe tool wear stage. The states were selected to investigate the steady tool wear stage and severe tool wear stage. The worn surface of the cutting tools tested at 0.33 m/s was the sever wear stage.

Figure 4.19 showed the SEM images of rake face of FeB-10Ni cutting tool tested for 6 m at the different cutting speeds. The edge chippings were observed in Fig.4.19 (a) and fracture were observed on the tool cutting edge of the FeB-10Ni cutting tools in Fig.4.19(b)-(d). Tool wear on the rake face was formed due to the sliding of the chips against the rake surface. According to the above-mentioned results of friction and wear tests, the dominant wear mechanism was adhesion. The adhesive Ti alloys were broken off and took away pieces of tool material, which resulted in the exacerbation of edge chipping to fracture as shown in Fig. 4.19. Tool materials spalling after the adhesive of titanium layers could be seen on the rake face. With the increased of the cutting speed to 0.33 m/s, the impact in the interrupted cutting test was increased. Moreover, increasing the cutting speed increased cutting temperatures. The hardness of the tool material typically dropped with the increase of the cutting temperature which also resulted in the increasing of the adhesive wear rate. Thus, a substantial loss of the portion of the FeB-10Ni tool appeared as shown in Fig. 4.18 (d).

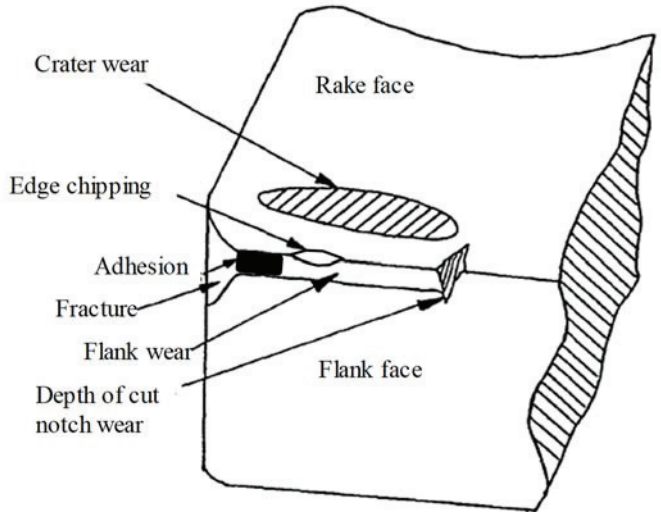

Figure 4.18 Schematic illustration of the tool wear.

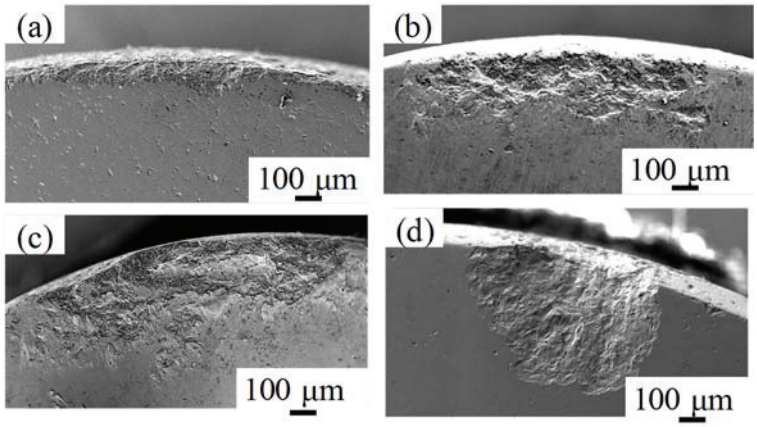

Figure 4.19 SEM images of rake face of FeB-10Ni cutting tool tested for 6 m at the cutting speeds of (a) 0.03, (b) 0.05, (c) 0.17 and (d) 0.33 m/s.

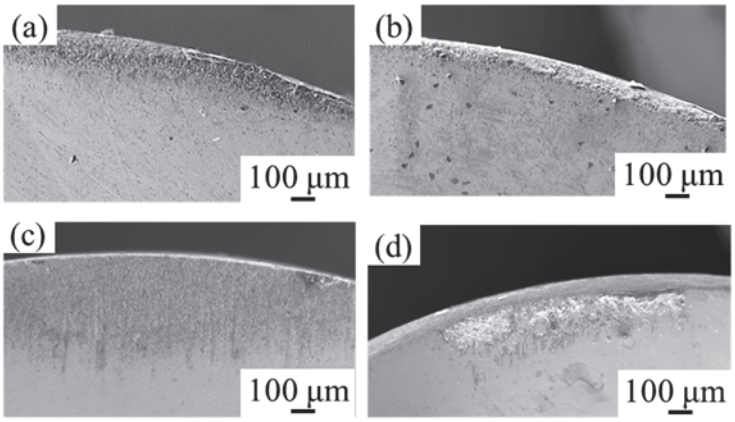

Figure 4.20 SEM images of rake face of WC-7.8Co cutting tool tested for 6 m at the cutting speeds of (a) 0.03, (b) 0.05, (c) 0.17 and (d) 0.33 m/s.

For comparison, the morphologies of rake face of WC-7.8Co cutting tool tested under different cutting speeds were shown in Fig. 4.20. The adhesive Ti layers and exposed tool substrate were clearly visible in rake face regions of the WC-7.8Co cutting tool. The various degrees of edge chippings were also observed in this figure. The softened Ti64 material was adhered to the rake face formed the thin deposited adhesive layers, regardless of the cutting speed. The cutting tool surfaces did not appear the phenomenon of catastrophic loss of the cutting edge of WC-7.8Co cutting tool. Only some peeling off of tool debris were observed on the rake face of the WC-7.8Co tool as shown in Fig.4.19 (d).

As the cutting length reached to 30 m, the catastrophic loss of the cutting edge of the FeB-10Ni cutting tool appeared regardless of the cutting speed as shown in Fig.4.21. The chips flow accumulated frictional heat and the mechanical impact at the tool-chip interface with the increase of the cutting length during the interrupted cutting. The increasing thermal mechanical loads associated with the adhesive titanium layers decreased the tool strength and then resulted in the catastrophic loss of the tool materials. In addition, fracture of the cutting edge also resulted in decrease of the contact area and deteriorated tool wear.

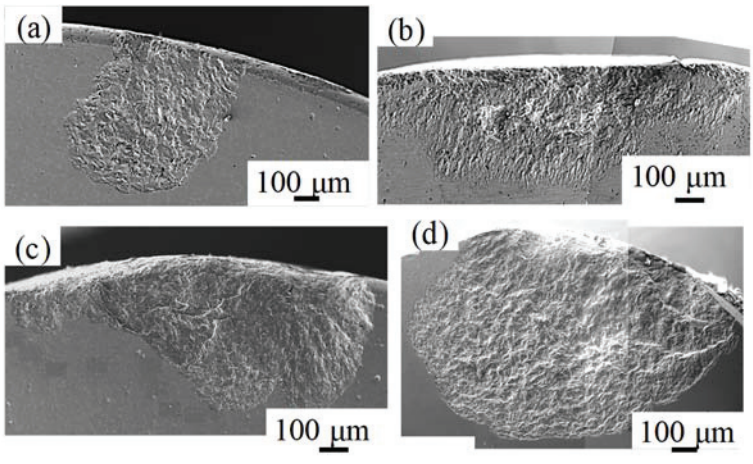

Figure 4.21 SEM images of rake face of FeB-10Ni cutting tool tested for 30 m at the cutting speeds of (a) 0.03, (b) 0.05, (c) 0.17 and (d) 0.33 m/s.

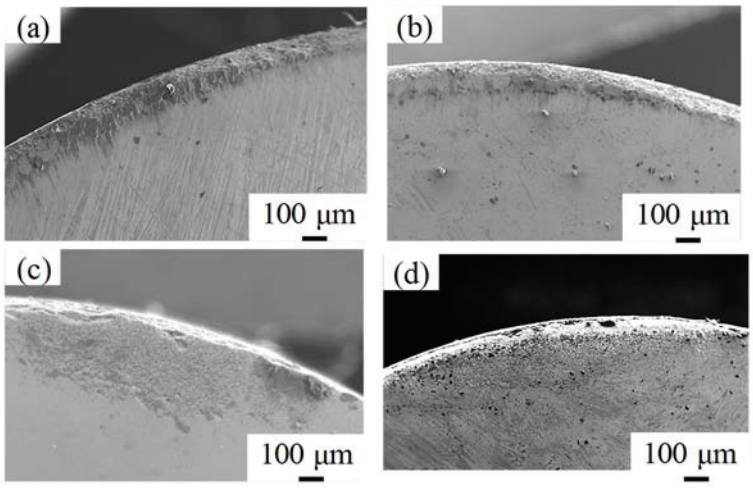

Figure 4.22 SEM images of rake face of WC-7.8Co cutting tool tested for 30 m at the cutting speeds of (a) 0.03, (b) 0.05, (c) 0.17 and (d) 0.33 m/s.

Figure 4.22 showed the SEM images of rake face of WC-7.8Co cutting tool tested for 30 m under different cutting speeds. As the cutting length increased, the edge chippings of the rake face presented more significant. The severe friction effect generated at the tool-workpiece interface deteriorated the rake face wear. But no catastrophic loss of the cutting edge of the WC-7.8Co cutting tool were observed even in high cutting speed as shown in Fig. 4.21 (d).

The different phenomenon of the tool wear occurred on the rake face of the two cutting tools was mainly caused by the different microstructure and mechanical properties. WC-7.8Co tool showed finer grain size than that of FeB-10Ni tool. According to the results of Venugopal et al.[24], the fine grain cutting tools did not appear the edge chipping or catastrophic loss at the tool cutting edge. As above-mentioned friction and wear results Cutting tool with fine grain size showed better resistance to the adhesive wear. Furthermore, WC-7.8Co cutting tool with fine grain size possessed higher strength and hardness than that FeB-10Ni tools with coarse grain. The low resistance to the adhesive wear and low strength resulted in the more sever wear of the FeB-10Ni cutting tool.

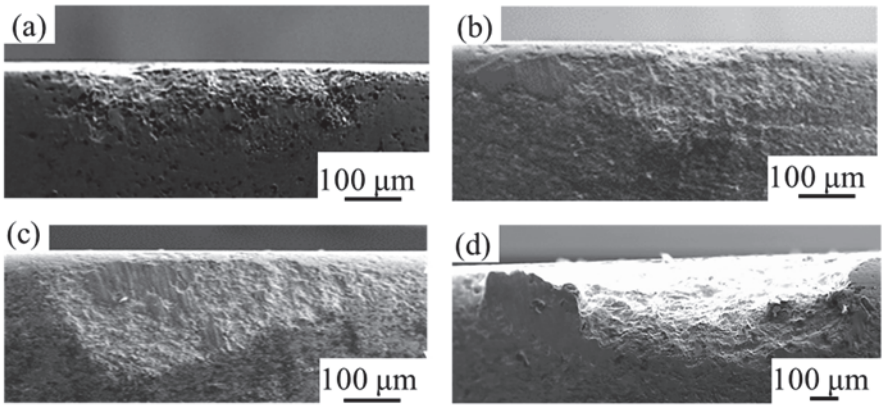

Figure 4.23 Flank wear images of FeB-10Ni cutting tool tested for 6 m at the cutting speeds of (a) 0.03, (b) 0.05, (c) 0.17 and (d) 0.33 m/s.

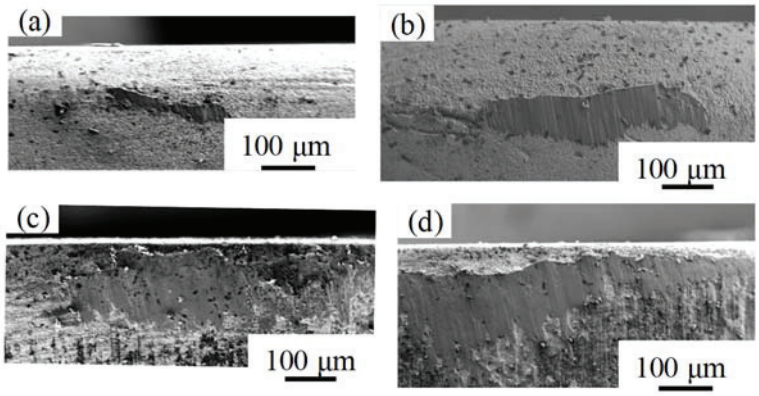

Figure 4.24 Flank wear images of WC-7.8Co cutting tool tested for 6 m at the cutting speeds of (a) 0.03, (b) 0.05, (c) 0.17 and (d) 0.33 m/s.

Because of the small Young's modulus and higher surface spring back of the Ti64 alloy, the flank face of the tool also suffered severely localized friction and extrusion effect during the interrupted cutting tests. As shown in Fig. 4.23, the non-uniform wear land occurred at flank face of the FeB-10Ni cutting tool. At the cutting speed less than 0.17 m/s, no obvious edge chippings were observed. As the cutting speed increased, the catastrophic loss of the cutting edge appeared. In addition, a series of Ti layers were observed in this figure. The adhesive Ti layers were easily peeled off, taken away the part of the tool material and ultimately deteriorated the flank wear, especially in high cutting speed.

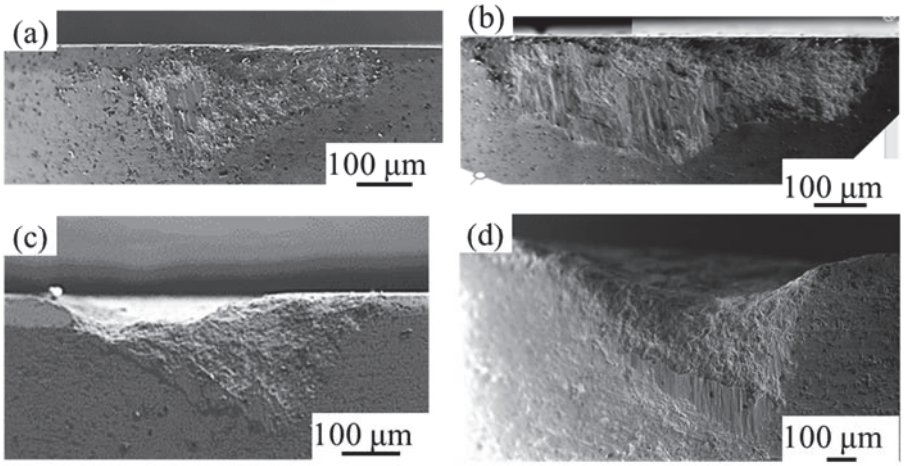

Figure 4.25 Flank wear images of FeB-10Ni cutting tool tested for 30 m at the cutting speeds of (a) 0.03, (b) 0.05, (c) 0.17 and (d) 0.33 m/s.

Figure 4.24 showed the flank wear images of WC-7.8Co cutting tool tested for 6 m under different speed. The wear land occurred at flank face of the WC-7.8Co cutting tool was more uniform than that of FeB-10Ni cutting tool. The phenomenon of adhesion was more obvious for the WC-7.8Co cutting tool. Edge chippings were also observed at the cutting speed of 0.33 m/s due to the peel off and take away the part of the tool material.

With the increasing of the cutting length, the flank wear became more serious as shown in Fig. 4.25. The adhesive titanium layers still existed in the cutting edge. At the cutting speed less than 0.05 m/s, no obvious edge chippings of the FeB-10Ni cutting tool were observed shown in Fig. 4.25 (a) and (b). As the cutting speed increased, a substantial loss of the portion of the FeB-10Ni cutting tool appeared in Fig. 4.25 (c) and (d). This adhesive titanium was broken off and took away of the tool material resulted in the decrease of the contact areas between the FeB-10Ni cutting tool and the work piece. The decreasing of the contact areas would increase the cutting force which accelerated the wear rate of the cutting tool. In addition, as the interrupted cutting proceeded, the accumulated frictional heat decreased the strength of the cutting edge which would resulted in the catastrophic loss of the tool material shown in Fig. 4.25 (d)[25].

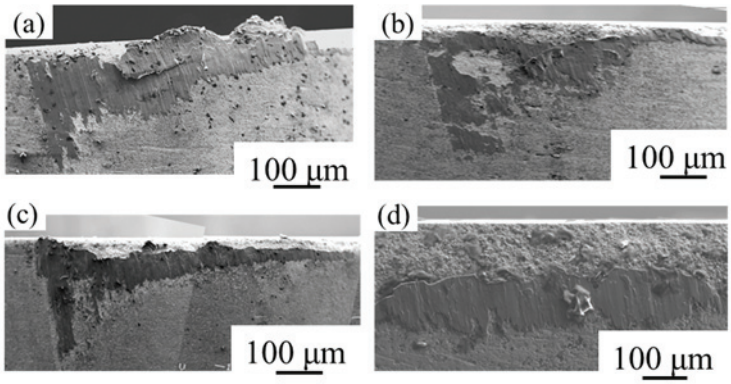

Figure 4.26 Flank wear images of WC-7.8Co cutting tool tested for 30 m at the cutting speeds of (a) 0.03, (b) 0.05, (c) 0.17 and (d) 0.33 m/s.

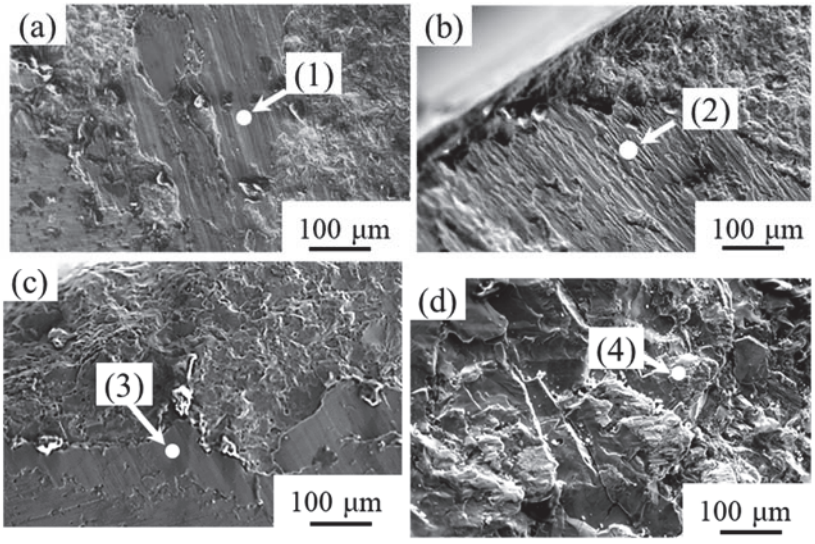

Analysis points	Element (At.%)						
	Fe	Ni	B	Ti	Al	V	O
(1)	0.3811	0.0249	0	73.595	13.2628	4.6783	8.0579
(2)	0.3928	0.0968	0	72.6255	14.4712	5.2884	8.9252
(3)	0.3934	0.0381	0.3226	71.7392	14.8541	5.8614	8.7912
(4)	0.1934	0.0751	0.0704	70.4204	13.2973	4.6459	11.2975

Figure 4.27 Point analysis of the flank wear of FeB-10Ni cutting tool tested for 30 m at the cutting speeds of (a) 0.03, (b) 0.05, (c) 0.17 and (d) 0.33 m/s. Insert tables were the results of point analysis.

Figure 4.26 showed the flank wear images of WC-7.8Co cutting tool tested for 30 m at different cutting speeds. Significant adhesive titanium layers were observed on the flank face of the WC-7.8Co tool in this figure. The softened Ti64 material adhered to the flank face formed the thin deposited the built-up layer (BUL) shown in Fig. 4.26 (a). With the increasing of the cutting speed, the peeling off of the adhesive titanium layers took away the tool materials resulted in the remove of the BUL and chippings of the cutting edge shown in Fig. 4.25 (b)-(d). In addition, the flank faces of the cutting tool did not appear the phenomenon of catastrophic loss of the cutting tool material due to the advantages of using fine grain cutting tools.

The chemical element compositions of the flank wear regions of FeB-10Ni cutting tool were measured by EPMA as shown in Fig. 4.27. The results of element analysis indicated that adhesive Ti existed at the flank wear regions. Little tool material element Fe and Ni diffused into the adhesive titanium layers at low cutting speed since higher cutting speed resulted in high cutting temperature. In addition, the traces of abrasion wear were presented at the adhesive titanium layers as shown in Fig. 4.27. Excessive abrasion effect existing between the tool and workpiece surfaces. These appearances were related to higher thermo-mechanical stresses and resulting from the severe friction between machined surface and flank face. It also means that wear debris promoted the abrasive wear. As shown in Fig. 4.27(a), the distribution of the adhesive Ti layer showed a lamellar state with uneven thickness. The adhesive titanium layers would play a certain protective role in reducing the further tool flank wear[26]. With the increasing of the cutting speed, the adhesive titanium layers were broken and tool away the tool materials. This was also a reason for the less flank wear width of FeB-10Ni cutting tool at low cutting speed.

Figure 4.28 showed the point analysis of the flank wear of WC-7.8Co cutting tool tested for 30 m at different cutting speeds. The results of element analysis also indicated the severe adhesive titanium existed at the flank wear regions. The traces of abrasion wear were also observed in this figure. The abrasion wear between the cutting tool and the work piece would appear. The adhesive layers existed regardless of the cutting speed which reduced the flank wear rate in high cutting speed.

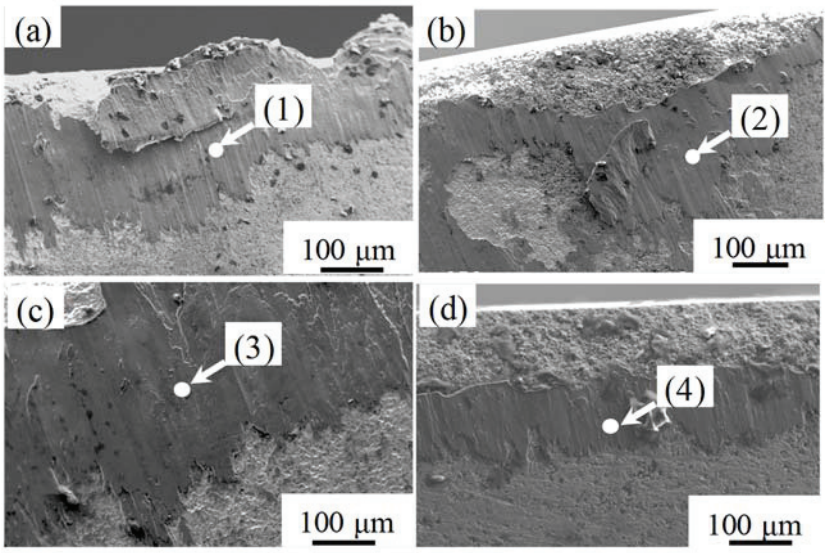

Analysis points	Element (At.%)						
	Fe	Ni	B	Ti	Al	V	O
(1)	0.3811	0.0249	0	73.595	13.2628	4.6783	8.0579
(2)	0.3928	0.0968	0	72.6255	14.4712	5.2884	8.9252
(3)	0.3934	0.0381	0.3226	71.7392	14.8541	5.8614	8.7912
(4)	0.1934	0.0751	0.0704	70.4204	13.2973	4.6459	11.2975

Figure 4.28 Point analysis of the flank wear of WC-7.8Co cutting tool tested for 30 m at the cutting speed of (a) 0.03, (b) 0.05, (c) 0.17 and (d) 0.33 m/s. Insert tables were the results of point analysis.

4.4 Summary

Wear and cutting performance of the FeB-10Ni cutting tool were investigated to compare the WC-7.8Co cutting tool. The main conclusions were summarized as follows.

(1) Pin-on-disc friction and wear tests on FeB-10Ni/Ti64 combinations revealed that the adhesion, abrasion, surface binder removal, grain polishing, grain cracking and grain pull out. The friction coefficient and worn surfaces of FeB-10Ni and WC-7.8Co alloys exhibited similar wear characteristics. This result was attributed to the complex operative wear mechanisms, such as adhesion and abrasion. Adhesive wear was found to be the dominant mechanisms controlling the wear rate of the FeB-10Ni and WC-7.8Co alloys.

Also, the breakdown of adhesive layer created hard debris, resulting in abrasive wear in subsequent sliding.

(2) Flank wear width was measured as a function of cutting length with different cutting speed. The flank wear width of all the tools increased with the increase of cutting speed. Flank wear width was within the criterion value of 0.3 mm in low cutting speed when machining Ti64 alloy for the FeB-10Ni cutting tool. The cutting performance of FeB-10Ni tool was comparable to that of WC-7.8Co tool at cutting speed less than 0.17 m/s.

(3) There was adhesive and abrasive wear on the rake and flank face of FeB-10Ni tool, and less serious combination of the above wear patterns as for WC-7.8Co tool. The With the increase of cutting speed, there existed amazing adhesive wear on the flank and edge breakage occurred at large cutting speed for the FeB-10Ni. The chippings of the FeB-10Ni cutting tool edge destroyed the structure and strength of the cutting tool, resulted in the decrease of the cutting performance of FeB-10Ni tool.

References

1) Z. L. W. Houping. Status of cemented carbide industry both at home and abroad. Cemented Carbide, 2009, 26(2), 122-127.
2) C. M. Fernandes, A. M. R. Senos. Cemented carbide phase diagrams: a review. International Journal of Refractory Metals and Hard Materials, 2011, 29(4), 405-418.
3) D. A. Stephenson and J. S. Agapiou. Metal cutting theory and practice. CRC press, 2016, 83.
4) V. P. Astakhov. The assessment of cutting tool wear. International Journal of Machine Tools and Manufacture, 2004, 44(6), 637-647.
5) E. O. Ezugwu and Z. M. Wang. Titanium alloys and their machinability—a review. Journal of materials processing technology, 1997, 68(3), 262-274.
6) N. Narutaki, A. Murakoshi, S. Motonishi, et al. Study on machining of titanium alloys. CIRP Annals-Manufacturing Technology, 1983, 32(1), 65-69.
7) P. A. Dearnley and A. N. Grearson. Evaluation of principal wear mechanisms of cemented carbides and ceramics used for machining titanium alloy IMI 318. Materials Science and Technology, 1986, 2(1), 47-58.
8) M. Nouari and H. Makich. Experimental investigation on the effect of the material microstructure on tool wear when machining hard titanium alloys: Ti–6Al–4V and Ti-555. International Journal of Refractory Metals and Hard Materials, 2013, 41,259-269.
9) T. B. Massalski, H. Okamoto, P. R. Subramanian, et al. Binary alloy phase diagrams. vol. 3. ASM International, 1990, 1485.
10) M. Buciumeanu, A. Bagheri, N. Shamsaei, et al. Tribocorrosion behavior of additive manufactured Ti-6Al-4V biomedical alloy. Tribology International, 2018, 119, 381-388.
11) S. I. Cha, S. H. Hong and B. K. Kim. Spark plasma sintering behavior of nanocrystalline WC–10Co cemented carbide powders. Materials Science and Engineering: A, 2003, 351(1-2), 31-38.

12) A.T. Santhanam, P. Tierney and J.L. Hunt. Cemented Carbides, in: ASM Handbook, vol. 7, Powder Metallurgy, ASM International,1990.

13) E.K. Storms, The Refractory Carbides, Academic Press, 1978.

14) W. Glaeser. Wear Failure Analysis. Wear of materials, 1979, 639-652.

15) K. Bonny, P. De Baets, W. Ost, et al. Influence of electrical discharge machining on the reciprocating sliding friction and wear response of WC–Co cemented carbides. Int. J. Refract. Met. Hard Mater., 2009, 27(2), 350-359.

16) B. Bhushan. Introduction to tribology. John Wiley & Sons, 2013, 110-111.

17) F. P. Bowden and D. Tabor. The friction and lubrication of solids. Oxford university press, 2001.

18) L. Meier, N. Schaal and K. Wegener. In-process measurement of the coefficient of friction on titanium. Procedia CIRP, 2017, 58, 163-168.

19) J. Wang, Y. Cheng, Y. Zhang, et al. Friction and wear behavior of microwave sintered Al_2O_3/TiC/GPLs ceramic sliding against bearing steel and their cutting performance in dry turning of hardened steel. Ceramics International, 2017, 43(17), 14827-14835.

20) G.Purcek, O.Saray, F. Rubitschek, et al. Effect of internal oxidation on wear behavior of ultrafine-grained Nb–Zr. Acta Materialia, 2011, 59(20), 7683-7694.

21) F. H. Stott. The role of oxidation in the wear of alloys. Tribology International, 1998, 31(1-3), 61-71.

22) J. Xiong, Z. Guo, M. Yang, et al. Tool life and wear of WC–TiC–Co ultrafine cemented carbide during dry cutting of AISI H13 steel. Ceramics International, 2013, 39(1), 337-346.

23) W. Bouzid. Cutting parameter optimization to minimize production time in high speed turning. Journal of materials processing technology, 2005, 161(3), 388-395.

24) K. A. Venugopal, S. Paul and A.B. Chattopadhyay. Growth of tool wear in turning of Ti-6Al-4V alloy under cryogenic cooling. Wear, 2007, 262(9), 1071–1078.

25) X. Liang and Z. Liu. Tool wear behaviors and corresponding machined surface topography during high-speed machining of Ti-6Al-4V with fine grain tools. Tribology International, 2018, 121, 321-332.

26) Z.G. Wang, M. Rahman and Y.S. Wong. Tool wear characteristics of binderless CBN tools used in high-speed milling of titanium alloys. Wear, 2005, 258(5), 752–758.

Chapter 5
Conclusions

The final purpose of the present research was to develop an environment-friendly and ubiquitous hard materials to substitute the WC-Co hard material. By comparison among some refractory carbides, nitrides and borides, the iron borides (FeB and Fe_2B) were expected to substitute the WC. Consideration for the low sinterability of iron borides, Ni or Fe belong to the same transition group of Co was added to prepare the fully dense compacts.

At first, Fe was selected as the binder phase. Fe and FeB powders were mixed by the elemental blending methods. The sintering behaviors and mechanical properties of FeB-Fe system alloys with 0, 10 and 50% Fe addition were investigated to determine the suitable amount of Fe added. After that, the sintering behaviors of the FeB with suitable amount of Fe added will be further investigated. Simultaneously, the microstructures and mechanical properties including Vickers hardness and bending strength of the FeB-Fe alloys were also investigated to evaluate whether Fe was suitable as a binder phase for FeB.

The results showed that the sinterability of FeB was significantly improved by the addition of Fe binder phase. The FeB with 10% Fe addition alloys showed high hardness and bending strength. In this case, the FeB alloys with 10 vol% was optimum. However, a large number of pores still existed in these compacts due to the heterogeneity distribution of the Fe binder phase.

Then, Ni as a suitable candidate binder phase was also chosen and investiaged. In view of the above mentioned problems, the Ni binder phase was introduced by the electroless plating method. Single factor experiments were carried out to optimize the electroless plating process including treating amount, bath temperature and plating time. After optimized the electroless plating process, the effect of the Ni content at the range

of 5-30% on the sintering behaviors and mechanical properties of FeB-Ni hard materials were investigated to determine the suitable Ni content. Then, the effect of the sintering parameters including the sintering temperature and the holding time on the microstructures and mechanical properties of the FeB-Ni alloys were further investigated to prepare the fully dense FeB with suitable Ni content.

The results showed that the increased treating amount of the FeB powders and bath temperature would accelerate the chemical reaction rate, increase the Ni content and affect the homogeneity of the Ni coating. Electroless plating time had a greater impact on the increase of the Ni content. But they had no effect on the composition and structure of the coating. FeB with 5, 10, 25 and 30% Ni alloys were successful prepared by spark sintering process. The relative density of FeB-Ni alloys increased with the increase of Ni content. FeB with 10% Ni alloys showed the maximum hardness, compressive strength and fracture toughness. The densification curves of FeB–Ni alloys showed that the plastic deformation and power-law creep deformation of the Ni binder phase in the FeB–Ni compacts occurred before and after reaching the maximum densification rate, respectively. The sintering temperature had a significant influence on the relative density and the homogeneous distribution of the Ni of the FeB-10Ni compacts. The holding time had a significant influence on the grain size, porosity and the mechanical properties of the FeB-10Ni compacts. The mechanical properties of FeB-10Ni compacts sintered at 1473 K without no holding time were comparable to that of WC-7.8Co compact.

Then, the friction and wear tests were conducted at the pin-on-disc wear tester to investigate the wear behaviors and wear mechanisms. The practical applications cutting tests were conducted on the milling machine at the feed rate of 0.05 mm/r and the depth of 0.2 mm. The cutting performance was evaluated by the flank wear width VB (0.3 mm). The effect of the cutting speed at the range of 0.03 to 0.33 m/s on the flank wear width of the FeB-Ni cutting tool were investigated as well as the WC-7.8Co tool. The investigation of the worn surface was used for characterization of the cutting mechanism. The results showed that the FeB-10Ni and WC-7.8Co alloys exhibited similar wear characteristics. This result was attributed to the complex operative wear mechanisms. Adhesive wear was found to be the dominant mechanisms controlling the wear volume loss of the two alloys.

The flank wear width of all the tool increased with the increase of the cutting speed. There was adhesive and abrasive wear on the rake and flank face of FeB-10Ni tool, and less serious combination of the above wear patterns as for WC-7.8Co tool. With the increase of cutting speed, there existed amazing adhesive wear on the flank and edge breakage occurred at large cutting speed for the FeB-10Ni tool. The chippings of the FeB-10Ni cutting tool destroyed the structure and strength of the cutting tool, resulted in the decrease of the tool life of FeB-10Ni tool. The FeB-10Ni cutting tool was suitable used at the cutting speed of less than 0.17 m/s for the flank wear width within the criterion value of 0.3 mm.

Acknowledgements

I would like to express my sincere gratitude to Professor Kazuhiro Matsugi for his guidance and insight throughout this study. Professor Matsugi gave me full support not only on my research, but also on my life and career, which has played an important role in both of my professional and personal development. He gave me a rigorous scientific research training, which enabled me to master scientific research methods. His careful guidance to me, tirelessly correcting my thesis, was an example for me to learn.

I am greatly indebted Assistant Professor Yongbum Choi. He gave me so much positive help on my research, and I have learnt so much from him. I am also greatly indebted Assistant Professor Zhefeng Xu. He painstakingly took me to do my experiments and every progress I made was the result of his hard work. He taught me a lot in doing better at getting along with others and the accumulation of the knowledge of my life. His meticulous attitude towards science was the goal I should strive for in my future life. I couldn't imagine that I could get a doctor's degree without him. I would like to express my heartfelt thanks to Professor Keiji Yamada for their technical advice and experimental assistance. I would like to thank Kenjiro Sugio. He gave me so much positive help on my thesis. I also would like to thank Suetsugu Kenichiro for the reviewing my thesis. I would like to thank professor Jinku Yu. Professor Yu gave me the chance to get a doctor degree at Hiroshima University.

Then, I would like to thank Mr. Youqiang Yao, Mr. Fuzhou Wang and Mrs. Meiqi Yu for considerable assistance and help in my experiments and my life during the difficult course of the thesis. Moreover, I would also like to thank all the past and present members of Property Control of Materials Laboratory, in Department of Mechanical Physical Engineering, Hiroshima University, for their enthusiastic help to both of my life and study.

Finally, my thanks would go to my parents and sisters for their loving considerations and great confidence in me all through these years. Thanks to my parents for their support and encouragement during my study. Thank them for their support over the years.

Published Papers Regarding to This Thesis

1. **S. Kang**, Z. F. Xu*, Y. B. Choi, K. Fujita, K. Matsugi, J. Yu. Spark sintering behavior of ubiquitously Fe-B and Fe powders and characterization of their hard composites. Materials Transactions, 2016, 57(5): 600-607. (Chapter 2)

2. **S. Kang**, Z. F. Xu*, Y. B. Choi, K. Matsugi, H. Kuramoto, J. Yu. Consolidation Behaviors of FeB–25Ni Powders in Spark Sintering and Mechanical Properties of Their Compacts. Materials Transactions, 2016, 57(12): 2139-2145. (Chapter 3)

3. **S. Kang**, Z. F. Xu*, Y. B. Choi, K. Fujita, K. Matsugi, J. Yu. Preparation of FeB-Ni hard materials by both electroless plating and spark sintering, and their Mechanical properties, J. Jpn. Soc. Powder Powder Metallurgy, 2016, 63(7): 484-490. (Chapter 3)

Presentations

1. **Shaoming Kang**, Zhefeng Xu, Yongbum Choi, Jinku Yu and Kazuhiro Matsugi. Preparation of Ni-W-P amorphous alloys by jet electrodeposition. 金属第 54 回・鉄鋼第 57 回中国四国支部講演大会, August 21, 2014, Tokushima, Japan, Tokushima University.

2. **Shaoming Kang**, Zhefeng Xu, Yongbum Choi, Jinku Yu and Kazuhiro Matsugi. The characterization in spark sintering for electroless Ni coated FeB powders. 粉体粉末冶金協会 平成27年度春季大会, May 26, 2015, Tokyo, Japan, Waseda University.

3. **Shaoming Kang**, Zhefeng Xu, Yongbum Choi, Jinku Yu, Kazuhiro Matsugi. Spark sintering of FeB-20vol%Ni powders and their mechanical properties. 金属第55回・鉄鋼第58回中国四国支部講演大会, August 19, 2015, Hiroshima, Japan, Hiroshima Institute of Technology.

4. **Shaoming Kang**, Zhefeng Xu, Yongbum Choi, Jinku Yu, Kazuhiro Matsugi. Spark sintering FeB-25Ni powders and their hardness properties. 日本金属学会 2015 年秋期大会, September 16, 2015, Tokyo, Japan, Kyushu University.

5. **Shaoming Kang**, Zhefeng Xu, Yongbum Choi, Jinku Yu and Kazuhiro Matsugi. Spark sintering of electroless Ni coated FeB powders and their mechanical properties. 3rd International Conference of Powder Metallurgy in Asia (APMA2015), November 8, 2015, Kyoto, Japan, Kyoto University.

6. **Shaoming Kang**, Zhefeng Xu, Yongbum Choi, Jinku Yu and Kazuhiro Matsugi. Spark sintering of FeB-Ni powders and their mechanical properties. 粉体粉末冶金協会　平成27 年度秋季大会, November 11, 2015, Kyoto, Japan, Kyoto University.

7. **Shaoming Kang**, Zhefeng Xu, Yongbum Choi, Jinku Yu and Kazuhiro Matsugi. Spark sintering behaviors of FeB-25Ni hard materials and mechanical　properties. 金属第56回 鉄鋼第59回 中国四国支部講演大会, August 22, 2016, Shimane, Japan, Shimane University.

8. Shaoming Kang, Kazuhiro Matsugi, Zhefeng Xu, Yongbum Choi, Keiji Yamada and Jinku Yu. Development of the ubiquitous FeB System Compacts for Cutting Tools.

日本金属学会 2017年春期大会, March 15, 2017, Tokyo, Japan, Tokyo Metropolitan University.